Prediction and Prolongation of the Service Life of Weathering Steel Highway Structures

by

Neal R. Damgaard

A thesis

presented to the University of Waterloo

in fulfillment of the

thesis requirement for the degree of

Master of Applied Science

in

Civil Engineering

Waterloo, Ontario, Canada, 2009

I hereby declare that I am the sole author of this thesis. This is a true copy of the thesis, including any required final revisions, as accepted by my examiners. I understand that my thesis may be made electronically available to the public.

Abstract

Weathering steel is a high-strength, low-alloy steel which has been proven to provide a significantly higher corrosion resistance than regular carbon steel. This corrosion resistance is a product of the small amounts of alloying elements added to the steel, which enable it to form a protective oxide layer when exposed to the environment. The main advantage of its use in bridges is that, under normal conditions, it may be left unpainted, leading to significantly reduced maintenance and environmental costs.

Weathering steel has been a material of choice for highway structures for almost half a century, and a very large number of structures have been constructed with it. Although its use has for the most part been successful, it has also become evident that, in circumstances where there is the presence of salt and sulphur oxides, its performance is deficient. In these situations the corrosion penetration rate is much higher than expected, and the oxide layer forms in thick layers. This presents an added risk, since these layers flake off and fall onto the roadway. The degree of corrosion on structures can be very different, even if the structural type, location, and climate are similar.

Therefore the focus of the thesis is on the lifespan of weathering steel highway structures. Primarily this research is concerned with the effect of corrosion on the integrity of these structures, as well as ways of quantifying corrosion loss and protecting the structure from further corrosion.

In order to determine the lifespan of weathering steel highway structures subject to different rates of corrosion, a probabilistic structural analysis program has been developed to assess the time-dependent reliability of the structure. This program used iterative Monte Carlo simulation and a series of statistical variables relating to the material, loading, and corrosion properties of the structure. A corrosion penetration equation is used to estimate thickness loss at a selected interval, and the structural properties of the bridge are modified accordingly. The ultimate limit states of shear, moment, and bearing, and the fatigue limit state of web breathing, are taken into account. Three types of structures are examined: simply-supported box and I-girder composite bridges, and a two-span box girder bridge.

Based on the structural analysis of the corroding bridge structures presented herein, it can be seen that corrosion to the weathering steel girders can cause reduced service lives of the structures. I-girder bridges are shown to be more susceptible to corrosion than box girder bridges, with continuous box girder bridges showing the best performance. The amount of truck traffic does not affect the reliability of the bridge. The short-span and high strength steel bridges are more susceptible to corrosion loss, primarily because their girders have thinner sections. A two-lane bridge also has better performance than the wider bridges because the weight of the barriers and sidewalks is carried by fewer girders, so these girders are stockier. The web breathing limit state is less significant than the combined ultimate limit states. Lastly, and most importantly, inspection data from a highway bridge is used to demonstrate the benefit that can be derived from using field data to update the time-dependent reliability.

The ultrasonic thickness gauge (UTG) is a common tool for thickness measurement of steel sections. When used to measure weathering steel, this instrument provides accurate data about the depth of corrosion pits, but not their lateral dimensions. The measurement does not include the corrosion layer on the opposite side of the plate from the one being measured; however, if the corrosion layer is on the measured face, a disproportionate increase in the measured thickness can be seen.

In order to prevent or minimize corrosion loss, the steel is currently painted, a process with several environmental and financial disadvantages. Therefore, three novel protection methods have been assessed in a cyclic corrosion test: a zinc metallizing, an aluminum-zinc-indium alloy metallizing, and a zinc tape with a PVC topcoat. All these coatings are designed to act not just as barriers, but also as sacrificial anodes. The test was run for 212 24-hr cycles, over the course of which the all the coatings were proven effective at protecting the steel substrate, regardless of steel type and surface roughness and pretreatment.

In conclusion, the threat to all types of weathering steel highway structures by contaminant-induced corrosion is significant, but inspection data permits a more accurate prediction of time-dependent reliability for a structure, and protective coatings are a promising method of slowing the advance of corrosion.

Acknowledgements

I would like to thank the following persons for their varied contributions to this work:

- God. Also my wife, Maria, and my son, Paul, and all of my family.
- Dr. Scott Walbridge and Dr. Carolyn Hansson, invaluable co-supervisors of this thesis, as well as Jamie Yeung, who did excellent work for this project, and of whom great things are expected.
- Frank Pianca of the Ministry of Transportation of Ontario, Dave Whitmore and the other excellent people of Vector Corrosion Technologies, and Florent Lefevre-Schlick and his helpful coworkers at Essar Steel Algoma.
- For their technical support: Graham Cranston, Jovan Vukotic, Richard Morrison, Mike Cocker, Randy Fagan, Dr. Shahzma Jaffer, Ken Su, Jim Merli, Dr. Giovanni Cascante, John Boldt, Dr. Enming Hu, Mark Sobon, Ken Bowman, and others too numerous to mention.
- For their friendship: Nathan, Allan, Carol, Matt and Deborah, Dave, Jon and Maureen, Jessica, Liam, Ivan, Simon, Pete, Paul, all the members of the Civilators FC, and everyone else who over the last couple of years has made doing a master's degree enjoyable, or at the very least memorable.

Dedicated to my father

TABLE OF CONTENTS

LIST OF FIGURES

LIST OF TABLES

CHAPTER 1: INTRODUCTION

1.1 Background

Weathering steel is a high-strength, low-alloy steel that has been proven to provide significantly more corrosion resistance than regular carbon steel. This corrosion resistance is achieved by adding small amounts of certain alloys to the steel that promote the formation of a protective oxide layer when the steel is exposed to the environment. The main advantage of using weathering steel in bridge applications is that under normal conditions it may be left unpainted, leading to significantly reduced maintenance costs. This means periodical blast-cleaning and repainting of highway bridges could be avoided, which also has significant environmental benefits.

Weathering steel has been a material of choice for highway structures for almost half a century in North America, Europe, and Japan, with a very large number of structures being constructed with it. Although its use in bridge applications has frequently been successful, a number of cases have been identified more recently where its corrosion performance has been worse than expected. In some cases, the reasons for this poor performance have been identified. In others, adjacent bridges constructed at the same time and subjected to similar environments have performed very differently, making the cause of the poor performance difficult to determine conclusively.

Recently, the Ministry of Transportation of Ontario (MTO) has found that a number of their weathering steel highway bridges are corroding at higher-than-expected rates. This has led to concerns regarding the safety of these structures. Firstly, this corrosion is causing a reduction in the thicknesses of the bridge girder plates. This has structural implications that have yet to be examined in depth. Secondly, the corrosion product, in addition to being unsightly, has also been seen to spall off of these structures in pieces that are sufficiently large to pose a threat to traffic passing underneath.

As a direct result of these concerns, this thesis project was initiated to examine the potential structural safety issues resulting from the corrosion problems observed in weathering steel highway bridges in Ontario and the possible mitigation of these problems through the application of specialized zinc-based coating systems.

In further discussions with MTO engineers at the time that this thesis project was initiated, the following additional information was conveyed:

- In many of the "problem structures", the regions of poor corrosion performance can be related to the "splash zones" caused by trucks passing underneath the weathering steel structures. Figure 1.1 shows an example of this. In this figure, the region where the corrosion is most severe is the underside of the box girder bottom flange, on the side of the girder that faces the oncoming traffic.

Figure 1.1: Underside of highway structure

- The current practice is to blast-clean the heavily corroded regions over roadways, in order to remove the spalled corrosion product in a controlled way, rather than having it fall on the roadway gradually over time. However, this procedure is costly, since the corrosion product must be collected and disposed of whenever it is removed intentionally in large quantities.

- With regards to the structural assessment of corroding highway structures, there is currently a lack of understanding of how to interpret the plate thickness data obtained using ultrasonic thickness gauges (UTGs). A number of possible sources of systematic error in ultrasonic thickness measurements need to be examined.

1.2 Objectives

Based on the background presented in the previous section, the main objectives of the work conducted for the current thesis project are as follows:

1. to determine the limitations (if any) of the UTGs commonly used to measure plate thicknesses for structural assessment purposes;
2. to determine the effectiveness of zinc-based protective coatings intended to slow or halt the corrosion penetration into the weathering steel element;
3. to develop analysis tools that are able to predict at what point the structural reliability of weathering steel bridges will deteriorate to an unacceptable level due to progressive corrosion; and
4. to use these tools to determine how serious a threat the corrosion problem is to weathering steel highway structures with different structural configurations and under different corrosive environments.

1.3 Scope

The UTG thickness measurement study is limited to the analysis of measurements obtained using a single proprietary device thought to be typical of the UTGs commonly used by the industry and fabricated by a well known maker of these devices.

Three different zinc-based coatings are examined: a pure zinc metallizing coating, an aluminum-zinc-indium alloy metallizing coating, and a pure zinc tape product with a polyvinyl chloride (PVC) top layer. The performances of these three coatings are compared with uncoated weathering steel. All steel specimens are exposed to a corrosive atmosphere with a high salt content according to [SAE J2334].

The focus of the reliability analysis is on short to medium span (30-40 m long) steel-concrete composite overpass structures. Both box and I-girder structures are considered, as is corrosion at typical urban, marine, and rural corrosion rates. The structural analysis verifies the ultimate limit states of shear, moment, and bearing. One fatigue limit state (web breathing) is also considered. All structural calculations are in accordance with the Canadian Highway Bridge Design Code [CAN/CSA-S6-06].

1.4 Thesis Organization

This thesis is organized as follows: first, a literature review is presented, in which the latest research is discussed on the nature of weathering steel corrosion, protective anodic coatings, and time-dependent reliability assessment of bridges (Chapter 2). Next is an explanation of the test procedures employed for the UTG studies and the corrosion testing studies of the uncoated and coated steel specimens (Chapter 3). The results of these tests are presented in Chapter 4. After this, the theoretical approach employed for analysing the time-dependent reliability of corroding highway structures is explained and the parameters of the reliability models are described (Chapter 5). The results from the analyses of a number of bridges and situations are then discussed in Chapter 6. Finally, conclusions and recommendations are presented in Chapter 7.

CHAPTER 2: LITERATURE REVIEW

In the following sections of this chapter, a review of the existing research on the corrosion process that attacks weathering steel is first presented. This is followed by a summary of the research that has been conducted to date on the effectiveness of metallizing and zinc tapes for corrosion protection. Lastly, a number of key structural reliability concepts are introduced and a summary is provided of the research done to date on predicting the structural reliability of steel-concrete composite bridges.

2.1 Corrosion of Weathering Steel

The corrosion reaction for low-alloy steel is identical to that of regular steel; the difference can be seen in the effect of the alloys on the formation of the protective layer.

2.1.1 Corrosion Products

Misawa et al. [1974] found that the primary products of atmospheric corrosion of regular and low-alloy steels are crystalline and amorphous rust (FeOOH) and magnetite (Fe_3O_4). The rust is usually in the form of crystalline α-FeOOH or γ-FeOOH and amorphous ferric oxyhydroxide $FeO_x(OH)_{3-2x}$. In a marine environment, β-FeOOH is likely to be present as well.

2.1.2 Corrosion Reaction for Steel

A good explanation of the mechanism of atmospheric corrosion of steel seems to be that of Misawa et al. [1974], where corrosion begins with the anodic dissolution of iron into ferrous ions (Fe^{2+}). These ferrous ions react with moisture (hydrolysis) on the surface of the steel to form $FeOH^+$. The $FeOH^+$ in turn reacts with the oxygen (oxidation) in the atmosphere to form γ-FeOOH, which crystallizes and precipitates out of the system (the rate of crystallization and precipitation is increased if a drying cycle occurs).

Moisture mixed with pollutants, such as sulphur dioxide SO_2, has a relatively low pH. In contact with this mixture, the crystalline γ-FeOOH dissolves to form the amorphous $FeO_x(OH)_{3-2x}$, which precipitates again. Finally, the $FeO_x(OH)_{3-2x}$ undergoes a solid state transformation (deprotonation with hydroxyl ions from rainwater) to become α-FeOOH. This process is shown in Figure 2.1.

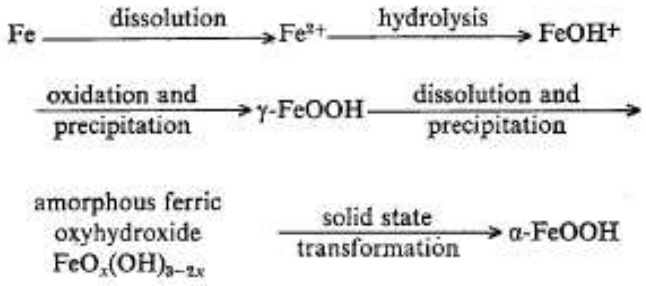

Figure 2.1: Reaction of overall rusting process [Misawa et al. 1974]

Kamimura et al. [2006] examined the ratio of α-FeOOH to γ-FeOOH in weathering steel exposed to industrial and rural environments, and the ratio of α-FeOOH to γ-FeOOH, β-FeOOH and Fe_2O_3 in weathering steel exposed to marine environments. They found that once these ratios achieved a certain value, the corrosion rate remains below 0.01 mm/year, which is considered a slow rate of corrosion. This finding essentially verified the research in [Misawa et al. 1974].

It should be noted that the corrosion process is fostered by accessible oxygen, the creation of an acidic solution layer by means of sulphur oxides (a product of vehicle exhaust, among other things), and a continuous wet-dry cycle.

2.1.3 Effect of Alloying Elements

According to Misawa et al. [1974], on a microscopic level, the corrosion layers of regular mild steel and weathering steel vary significantly. The layer on mild steel is uneven, with cracks and fissures that permit penetration of moisture, oxygen, and pollutants. The layer on weathering steel, however, is much more uniform and continuous; it is also found to contain relatively high amounts of the alloying elements particular to this type of steel, such as copper, chromium, and phosphorus. It appears, therefore, that these elements, which are evenly dispersed throughout the steel, enable the formation of a uniform layer of the corrosion product.

The main component of this layer on weathering steel is the amorphous ferric oxyhydroxide, $FeO_x(OH)_{3-2x}$; it is the formation of this product that is likely fostered by the alloying elements. These elements enable the formation of a uniform layer by first promoting uniform dissolution of the steel into γ-FeOOH; as this dissolves, the $FeO_x(OH)_{3-2x}$ forms a uniform layer. This layer is relatively dense and contains a high

amount of bound moisture, but is slow to absorb and release water from external sources. Furthermore, it is free of fissures or cracks, and so it prevents the penetration of oxygen and contaminants that foster corrosion.

The same wet-dry cycles that cause progressive corrosion to mild (regular) steel are required for the formation of this protective layer in weathering steel. Also, according to this theory, Fe_3O_4 is the product of an oxygen-deprived state that exists after a dense layer of rust has formed on the steel surface.

This is one theory; other systems of understanding rust layer formation also exist [Jones 1996, Albrecht and Naeemi 1984, Wang et al. 1997].

2.1.4 Effect of Road Salt on Weathering Steel

It has been noted that weathering steel does not appear to form a protective patina in the presence of chlorides, especially de-icing salt [Albrecht & Naeemi 1984, Albrecht & Hall 2003, Cook 2005]. This is due in part to the hydroscopic qualities of the salt; it attracts water, and so keeps the steel moist for longer periods of time and preventing the occurrence of dry conditions necessary for the patina formation.

The other factor is the presence of chloride ions, Cl^-. These negatively charged ions increase the negative potential of the steel, which accelerates the rate of corrosion of the metal (this is also an effect of the SO_4^{-2}, though to a lesser degree). Also, in the presence of chloride ions the corrosion reaction results in relatively large amounts of β-FeOOH. This oxide does not convert to form $FeO_x(OH)_{3-2x}$, which is the main component of the protective oxide layer of weathering steel [Misawa et al. 1974, Albrecht & Naeemi 1984, Cook 2005].

2.1.5 Corrosion Rate Equations

Albrecht et al. [1989] provide an envelope for the corrosion penetration of weathering steel. The upper bound is described by the equation:

$$C = 50 + 7.5 \cdot (t - 1) \tag{2.1}$$

while the lower bound is described by the equation:

$$C = 25 + 3 \cdot (t - 1) \tag{2.2}$$

where C is corrosion penetration in μm, and t is time of exposure in years. These numbers are based on the average steady-state corrosion rates for the ISO high and medium corrosivity categories. These equations provide an envelope for the ideal behaviour of weathering steel subject to environmental corrosion; weathering steels corroding at a rate faster than that of Equation 2.1 cannot be expected to develop a protective layer, according to Albrecht et al. [1989].

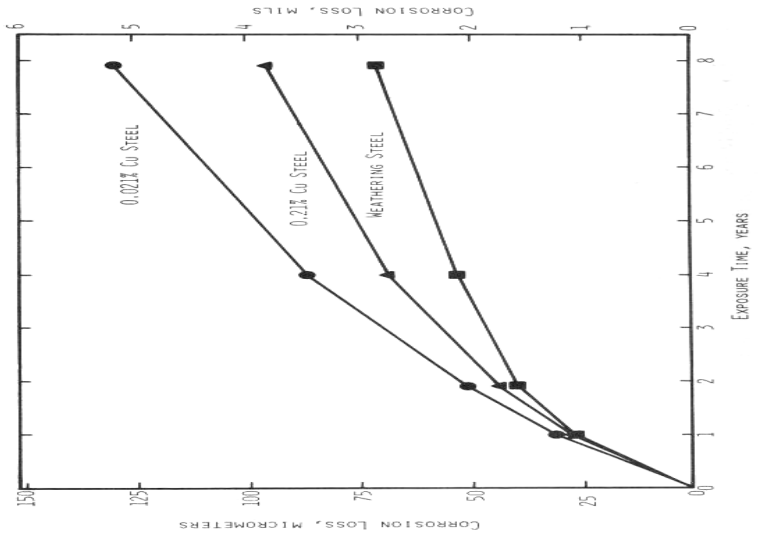

Figure 2.2: Corrosion penetration data plot [Townsend & Zoccola 1982]

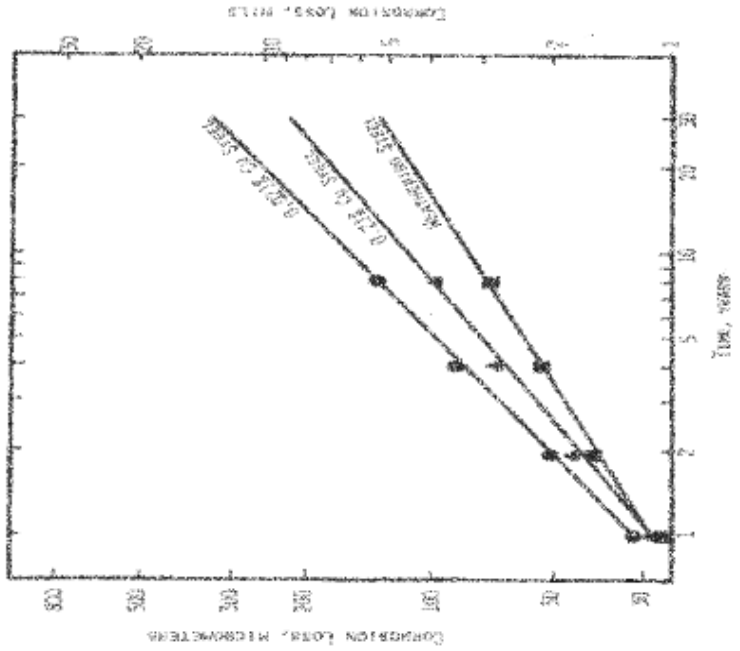

Figure 2.3: Corrosion penetration data plot, log-log scale [Townsend & Zoccola 1982]

Townsend and Zoccola [1982] tested specimens of weathering and copper steels in four different locations (matching marine, rural, industrial, and urban type environments). Figure 2.2 shows the output for the corrosion performance of two copper-steel specimens (circle and triangle markers) and a weathering steel specimen (square marker).

It was noted that the same data, plotted on a log-log graph, is linear (see Figure 2.3). On this basis, the standard equation (the logarithmic power model) for section loss due to corrosion of weathering steel [Townsend & Zoccola 1982, see also Albrecht & Naeemi 1984, G101-04] was deduced:

$$C = A \cdot t^{B} \tag{2.3}$$

In its logarithmic form, Equation 2.3 is a straight-line function:

$$\log C = \log A + B \log t \tag{2.4}$$

where C is the average corrosion penetration determined from weight loss, in units of length; t is the exposure time, in years; A is a regression coefficient numerically equal to the penetration after one year of exposure; and B is a regression coefficient equal to the slope of Equation 2.4 in a log-log graph. Effectively, A is related to the initial reactivity of the steel, while B accounts for the change in corrosivity of the steel over time.

Wang et al. [1997] found that an environment with a high concentration of SO_2 could cause serious deviation from the logarithmic power model. The two factors that were found to have a predominant effect on the performance of weathering steel are the corrosivity of the environment and the composition of the weathering steel.

Legault and Leckie [1974] created a set of equations for three levels of corrosive environment, i.e. semirural, marine, and urban; these equations were used to determine the corrosion rate of weathering steels based on percentages of their alloying elements. A modified form of one of their equations (modified to calculate corrosion resistance index rather than rate) is included in [ASTM G 101-04], despite the fact that their recommendations have been challenged by McCuen and Albrecht [2004].

In [McCuen & Albrecht 1994], another type of model is recommended and referred to as a composite model. One example of this is the power-linear model, which is composed of a pair of equations for calculating corrosion penetration, the first of which is identical to

Equation 2.3, and the second of which is linear. At a predetermined time, called an intersection time, the corrosion penetration switches from the first equation to the second, thus providing a constant rate of corrosion penetration after a certain point in time. Nevertheless, the model is less accurate for weathering steels than for other types of steel, and no guarantee of better results is made. In its defence, this model gives safer predictions (higher thickness loss estimates) over very long periods.

Another composite model recommended in [McCuen & Albrecht 1994] is the power-power model, similar to the power-linear model, but in this case both equations are power equations. In both of these cases, numeric fitting to data points is recommended, as opposed to the logarithmic approach of [Townsend & Zoccola 1982].

Finally, in [2005], McCuen and Albrecht modify their power-power model to account for the variable alloy content of weathering steel, specifically for the metals: copper, chromium, phosphorus, silicon, and nickel. This equation compares favourably with regards to the Legault and Leckie [1974] equations, but no comparison is made between this and the logarithmic power model.

Although the merits of each of the mentioned models can be argued, Equation 2.3, the logarithmic power model, is among the simplest of these and is commonly applied to structural problems resulting from corrosion attack. It should be noted that none of the models appear to have been experimentally verified for their validity over the long term.

2.2 Sacrificial Anode Protection of Weathering Steel

Two novel methods of providing corrosion protection for weathering steel are researched herein: metallizing and application of galvanic (zinc) tape to the steel surface.

2.2.1 Metallizing

Metallizing is a method of applying a layer of molten metal to a surface. The metal that is being sprayed is intended to act as a sacrificial anode. In the civil infrastructure, metallizing appears to be more commonly used on concrete for protecting the steel reinforcement than structural steel, perhaps because structural steel is more likely to be coated by painting to protect it from corrosion [see Sagüés & Powers 1995].

Matthes et al. [2003] tested three metallizing alloys – pure zinc, 85% zinc + 15% aluminum, and 12% zinc + 0.2% indium + balance aluminum. Zinc is a good cathodic protector of the substrate, while aluminum is more passive and functions primarily as a mechanical barrier. Small amounts of indium are introduced to improve galvanic efficiencies. Specimens of these alloys (flame-sprayed onto lexan panels) were boldly exposed in a rural and a marine environment and their runoff was measured for approximately 2.5 years. It was found that the zinc runoff was directly proportional to precipitation rate, but also to the amount of zinc in the alloy; interestingly, the higher chloride levels of the marine site did not have an effect.

Another test was reported by Kuroda et al. [2005]. In this case, twelve steel pipes were coated with zinc, aluminum, and an 87% zinc + 13% aluminum alloy, and were set vertically into seawater at a port in Japan. This test lasted for 18 years; corrosion was estimated by measuring the change of thickness of the metallizing. Over the duration of the test, most of the metallized specimens performed very well. The amount the coatings increased in thickness due to corrosion depended on their location vis-à-vis the water. One noted problem was that where the aluminum coating was damaged, red rust appeared, which is likely a result of the fact that aluminum has little anodic capacity. On the other hand, the zinc-aluminum alloy appeared to corrode at a much slower rate than the pure zinc. Kuroda et al. compared their results with those of similar tests, and found that they are about as expected.

2.2.2 Galvanic (Zinc) Tape

Galvanic (zinc) tape functions by the same fundamental mechanism as metallizing, insofar as it provides a sacrificial anode to protect the steel substrate. It is essentially a layer of sacrificial material with an adhesive backing; however, this adhesive must provide a mechanical and electrical connection to the substrate for the tape to be effective. Nevertheless, galvanic tape is a new material for this application, and no published research is available quantifying its performance.

2.3 Evaluating Corrosion Penetration

2.3.1 Visual Assessment of Corrosion Damage

At least one study has been made into the possibility of predicting the amount of section loss that has occurred by a visual inspection of the corroded surface [Hara et al. 2006]. It appears to be possible to correlate the condition of the attacked surface with the amount of section loss that has occurred. The first step is the taxonomy of the corrosion, i.e. the classification of the degrees of corrosion. Figure 2.4 shows how this classification was done in [Hara et al. 2006]; five stages of corrosion severity have been identified.

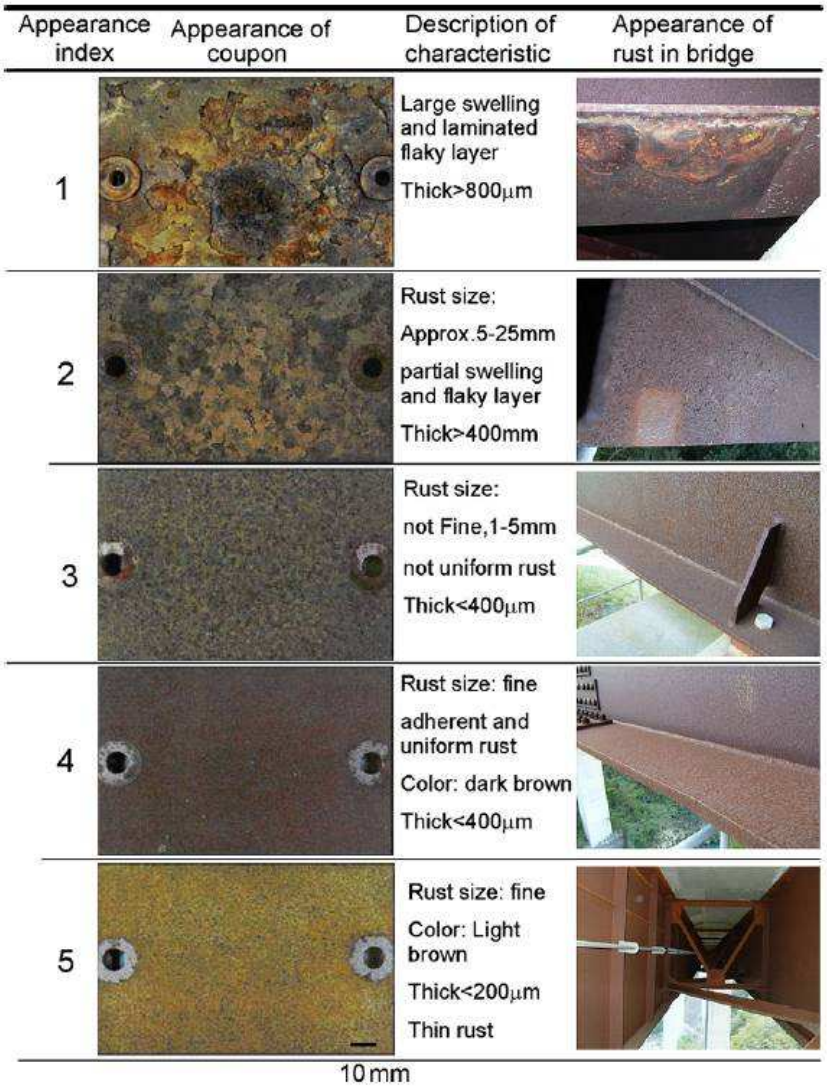

Figure 2.4: Taxonomy of rust types [Hara et al. 2006]

The specimens in this case were weathering steel test coupons exposed for between 1 and 18 years under eleven bridges in Japan. All of the specimens were exposed to varying degrees of humidity and airborne salt.The thickness loss of these test coupons was measured and correlated to the corrosion class. The results of this are shown in Figure 2.5.

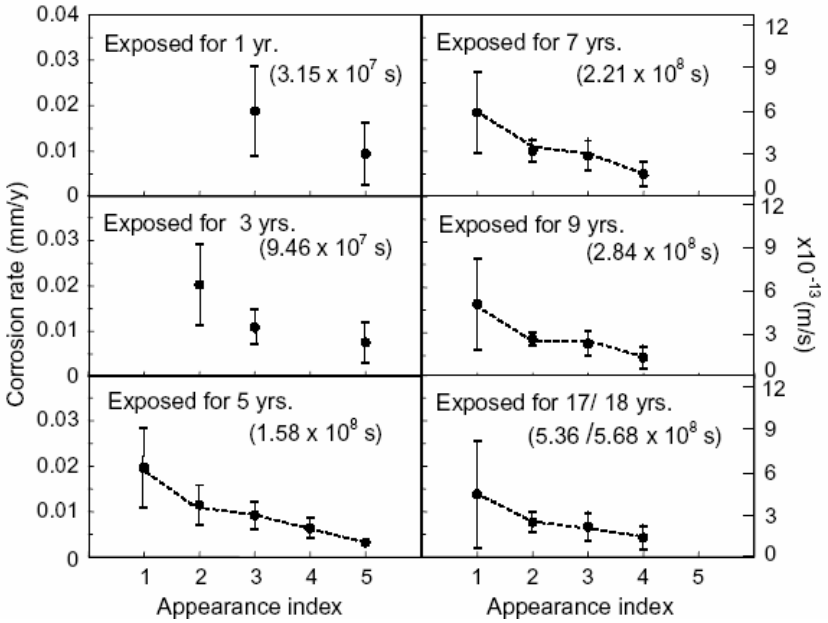

Figure 2.5: Correlation of corrosion stage and section loss over time [Hara et al. 2006]

The error bars in Figure 2.5 indicate $\pm 2 \cdot \sigma$ (two standard deviations) relating to the variability of the section loss data. Note that indices 1 and 4 did not appear in the short term tests, while index 5 did not appear in the longer term tests.

The appearance of index 1 corrosion indicates the possibility of rapid and progressive corrosion. The test results also show the high degree of variation that can be found in corrosion rates for a given type of corrosion. Also, the high corrosion rate of index 1 is consistent, regardless of the test period.

2.3.2 Ultrasonic Thickness Testing

Little research is available on the accuracy of ultrasonic thickness gauges (UTGs) in measuring the remaining section of a corroded weathering steel plate. Hara et al. [2007] note that corrosion thickness measurements are inaccurate and thus require extended periods of data collection (i.e. a minimum of six years) to determine the corrosion rate.

The sources of inaccuracy include the instrument itself, as well as the surface of the measured plate, which is usually somewhat rough and corroded. For this reason, the standard procedure used in industry involves grinding smooth a small area of the steel plate [J. Vukotic, personal communication, September 25, 2008]. Nevertheless, ultrasonic thickness measurement is recommended for inspection and assessment of corrosion degradation in steel bridges [Kulicki et al. 1990].

2.4 Structural Reliability Evaluation

In most modern structural design codes, the safety of a structure is measured (either directly or indirectly) in terms of its reliability index.

2.4.1 Probability of Failure and Reliability

The concept of structural reliability is bound to that of the limit states design process [Walbridge 2005]. Limit states are defined as the conditions of a structure or component beyond which it ceases to fulfill the function for which it was designed. Three types of limit state are identified in [Commentary on CAN/CSA-S6-00], namely fatigue, serviceability, and ultimate limit states. Fatigue cracking of a structure occurs at the fatigue limit state, while the serviceability limit state coincides with the occurrence of excessive vibrations or static deformations, sufficient to affect the usability or durability of the structure. Total failure of the structure by any suitable mechanism (i.e. fracture, buckling, overturning) is considered to be an ultimate limit state. Limit states may be described by limit state functions, $G\left(\bar{z}\right)$, which take the following form:

$G\left(\bar{z}\right) > 0$ means that the limit state is satisfied, so failure does not occur, (2.5)

$G\left(\bar{z}\right) < 0$ means that the limit state is surpassed and failure occurs, and (2.6)

$G\left(\bar{z}\right) = 0$ is the so-called “failure surface”. (2.7)

Where $\bar{z}$ is the vector of statistical variables, z_i, which take into account the various sources of uncertainty associated with the limit state function.

In [Melchers 2002] the basic reliability problem is described as having two competing statistical variables: the resistance, *R*, and the applied load, *S*. The corresponding limit state function and expression for the probability of failure, p_f, is as follows:

$$p_f = P\left(G\left(\bar{z}\right) < 0\right) = P\left(R - S < 0\right) \tag{2.8}$$

The probability density functions (PDF) for *S*, *R*, and $G\left(\bar{z}\right)$ are plotted in Figure 2.6. In this figure, the bold symbols are vectors, and therefore: $G(z) = G\left(\bar{z}\right)$.

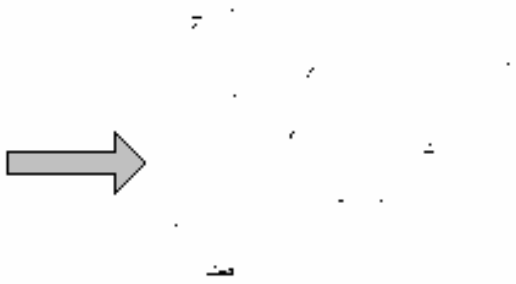

Figure 2.6: Probability curves [Walbridge 2005]

The p_f is the area under the PDF of $G\left(\bar{z}\right)$ for which $G\left(\bar{z}\right) < 0$. If the distributions for *S* and *R* are both normal, then the p_f can be calculated as follows:

$$p_f = \Phi\left(\frac{-\left(\mu_R - \mu_S\right)}{\sqrt{{\sigma_R}^2 + {\sigma_S}^2}}\right) = \Phi\left(-\beta\right) \tag{2.9}$$

where μ_S and μ_R are the means, and σ_S and σ_R are the standard deviations of the load and resistance variables, and $\Phi()$ is the cumulative density function for the standard normal distribution. Often, reliability is expressed by structural engineers in terms of the reliability index, β. As follows from Equation 2.9,

$$\beta = -\Phi^{-1}\left(p_f\right) \tag{2.10}$$

As can be seen in Figure 2.6, this index can be understood as the distance between the mean of the $G\left(\bar{z}\right)$ distribution and the origin, divided by the standard deviation, $\sigma\left(G\left(\bar{z}\right)\right)$. The p_f for a more general case can be expressed as follows:

$$p_f = P\left(G\left(\bar{z}\right) < 0\right) = \int \ldots \int_{G(\bar{z})<0} f\left(\bar{z}\right) dz \tag{2.11}$$

In other words, given a limit state function, $G\left(\bar{z}\right)$, containing n statistical variables, z_i, the p_f is equal to the volume in n-dimensional space under the portion of the joint PDF, $f\left(\bar{z}\right)$, for which $G\left(\bar{z}\right) < 0$. In order to solve the integral in Equation 2.11, one of two approaches is usually applied: numerical methods such as Monte Carlo simulation (MCS) or analytical methods such as the First Order Reliability Method (FORM) [Walbridge 2005].

2.4.2 Reliability in the Bridge Code

The safety philosophy of the [CAN/CSA S6-06] is to have a consistent level of risk to life for each bridge element. The level of risk is equal, by definition, to the probability of failure multiplied by the cost of failure. In [CAN/CSA S6.1-00] (see also Figure 2.7), the cost of failure of a bridge element is related to the likelihood of the element failure leading to loss of life. A consistent level of risk is maintained if a higher probability of failure is accepted in the elements whose failure will not result in a loss of life, or a lower probability of failure is accepted in the elements whose failure might result in a loss of life. Likewise, a structural element that receives frequent inspections, shows warning signs if approaching failure, or is capable of redistributing its load to other elements will be less likely to cause loss of life.

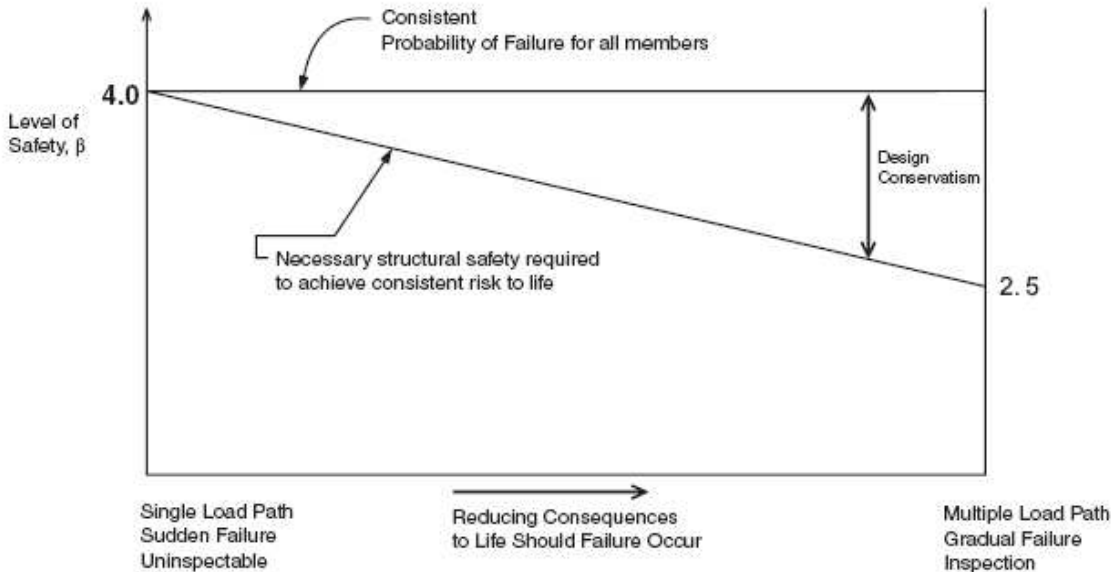

Figure 2.7: Relationship between risk and probability of failure [CAN/CSA S6.1-00]

In the [CAN/CSA S6-06]-recommended procedure for bridge evaluation, the level of safety is measured using the reliability index, β, which is inversely related to the notional probability of failure. The notional probability of failure is calculated using the life safety criterion of CSA S408-1981:

$$P_f = \frac{AK}{W\sqrt{n}} \tag{2.12}$$

Where P_f is the probability of failure, A is an activity factor taking into account the risk involved in activities associated with the structure, K is a calibration factor, W is a warning factor, and n is an importance factor. For determining a structure's capacity to carry vehicle trains, two-unit vehicles, and single-unit vehicles, in normal traffic, A is 3.0, K is 10^{-4}, W is 1.0, and n is 10. Together, these give a P_f of 9.5 x 10^{-5}; this is the target P_f for a structure. Table 2.1 relates the values of the reliability index to the notional probability of failure values, based on a probability distribution where the probability of failure is normally distributed [CAN/CSA-S6.1-00]. Using Table 2.1 or Equation 2.10, a probability of failure, P_f of 9.5 x 10^{-5} corresponds with a reliability index of 3.73.

Table 2.1: Notional probability of failure for various reliability indices, based on the normal probability curve [CAN/CSA-S6.1-00]

Reliability Index, β	Notional Probability of Failure, P_f
2.00	2.3×10^{-2} or 1:44
2.25	1.2×10^{-2} or 1:81
2.50	6.2×10^{-3} or 1:160
2.75	2.8×10^{-3} or 1:360
3.00	1.4×10^{-3} or 1:740
3.25	5.6×10^{-4} or 1:1800
3.50	2.3×10^{-4} or 1:4300
3.75	8.8×10^{-5} or 1:11,000
4.00	3.2×10^{-5} or 1:31,500
4.25	1.1×10^{-5} or 1:93,500
4.50	3.4×10^{-6} or 1:294,000

2.5 Structural Analysis Models of Corroding Steel Bridges

Several studies have been performed over the last two decades that examined the effects of progressive corrosion on bridge reliability. All of the studies mentioned here focus on the time-variant reliability of simply-supported composite I-girder bridges, but they look at different aspects of the structures and how progressive corrosion affects their reliability. They also consider different girder regions that can be affected by corrosion.

2.5.1 Research of J.R. Kayser

In [Kayser 1988, Kayser & Nowak 1989], the examined structures are two-lane bridges with five I-girders, ranging from 12.2 m to 30.5 m in length. A cross section of the examined bridge type is shown in Figure 2.8.

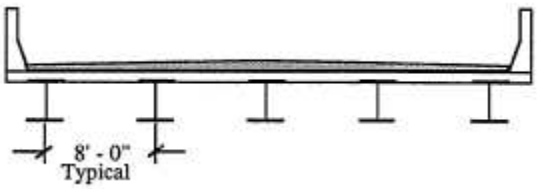

Figure 2.8: Steel I-girder bridge cross section [Kayser 1988]

The bridge has a composite section, with a 190 mm thick, 27.6 MPa concrete slab. Since the number of girders is constant, the girder size is varied with the bridge length, from W610x113 for the 12.2 m bridge to W920x345 for the 30.5 m bridge. The girders are hot-rolled and composed of 250 MPa steel. Kayser apply the standard equation (see Equation 2.3) in his corrosion penetration models. Regarding the assumed corrosion location, for the majority of the span, general thickness loss is assumed to occur to the top of the bottom flange and the bottom quarter of the web (Figure 2.9). However, at the supports, the web is assumed to corrode over its entire depth.

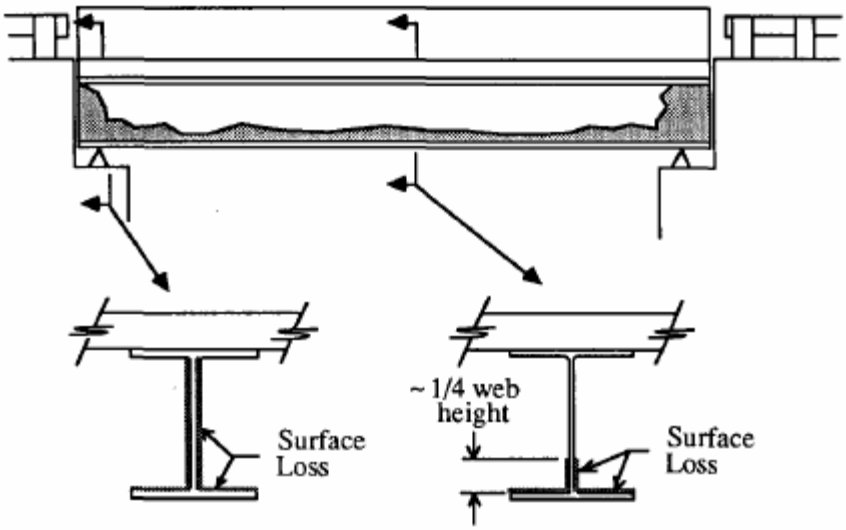

Figure 2.9: Typical corrosion locations assumed by [Kayser 1988]

Kayser [1988] consider the effect of corrosion on the flanges and webs of the girders, but not on the connections or secondary members such as cross-bracing. They also ignore the problem of corrosion fatigue. The failure modes considered include shear, moment, and bearing, since they have the greatest effect for single-span I-girders.

In Kayser [1988], it is found that bearing and shear usually govern at high levels of corrosion since the resistances are dependent upon the web, which is thinner and more sensitive to thickness loss due to corrosion. Also, elements in compression are more sensitive since they become more susceptible to buckling.

Figure 2.10 shows the reliability predictions for a 12.2 m long bridge.

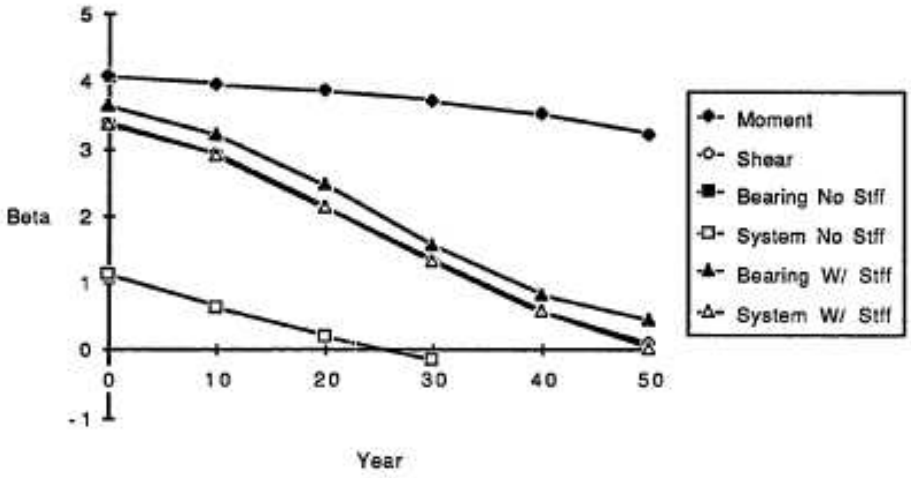

Figure 2.10: Reliability of a 12.2 m long bridge [Kayser 1988]

Figure 2.11 shows the reliability predictions for a 30.5 m long bridge.

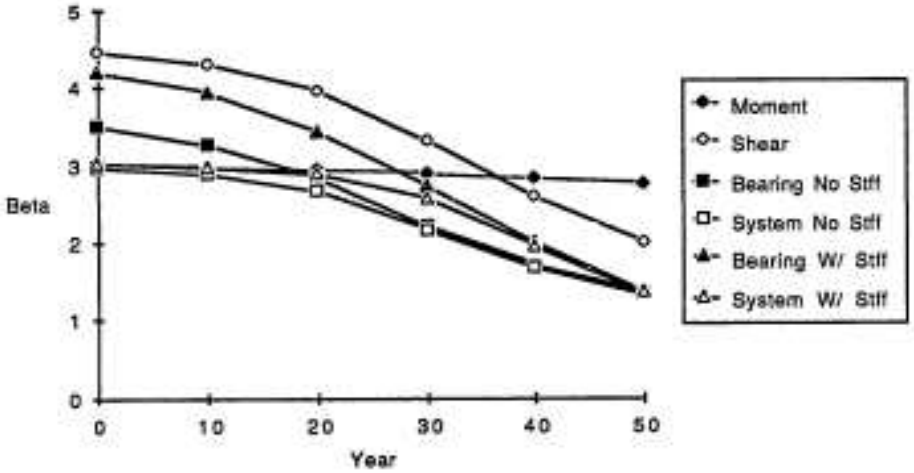

Figure 2.11: Reliability of a 30.5 m long bridge [Kayser 1988]

As can be seen from these figures, the shorter span bridge is more susceptible to capacity loss over time; this is a direct result of the fact that bearing stiffeners are not required for the shorter bridge, but if the bridge is thus unfitted, it becomes susceptible to failure in the bearing mode in a relatively short amount of time.

It was also found that the thickness loss exponent B is the most influential parameter in the corrosion rate model. The variation of B had a significant effect on the reliability fraction, β/β_0, of a bridge, far more so than A, as is shown in Figure 2.12.

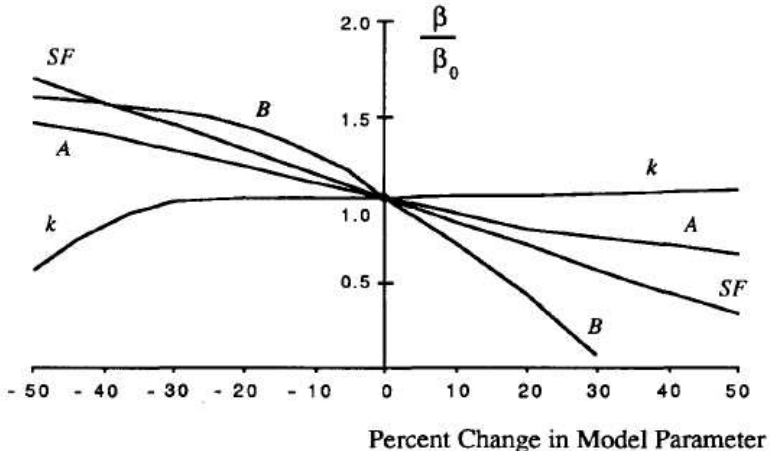

Figure 2.12: Sensitivity study of model parameters [Kayser & Nowak 1989]

Also presented in this figure are the effects of varying the shear distribution parameter (SF) and the bearing plate coefficient (k). Figure 2.13 shows the reliability performance of an 18 m long span in different corrosion environments.

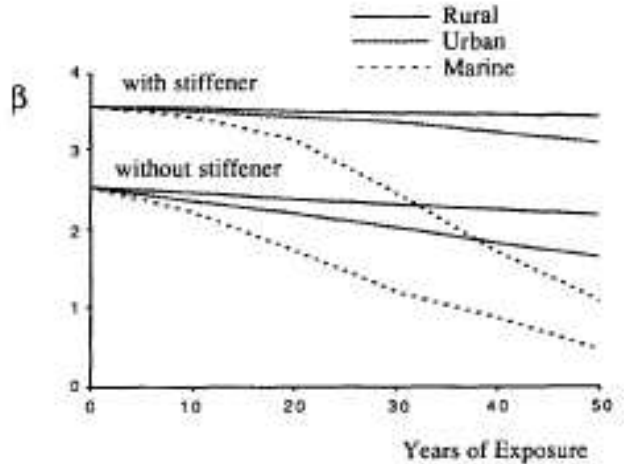

Figure 2.13: 18 m long span in different environments [Kayser & Nowak 1989]

The bridge reliability is not significantly affected by the rural corrosion rate, but the effects of the urban and marine corrosion rates are significant. Note that the reliability analyses in this study were performed for regular carbon steel girders.

2.5.2 Research of A.A. Czarnecki

[Czarnecki 2006, Czarnecki & Nowak 2006] looked at bridges from 12.2 m to 42.7 m in length, supported by four to six steel I-girders. Cross-sections are shown in Figure 2.14.

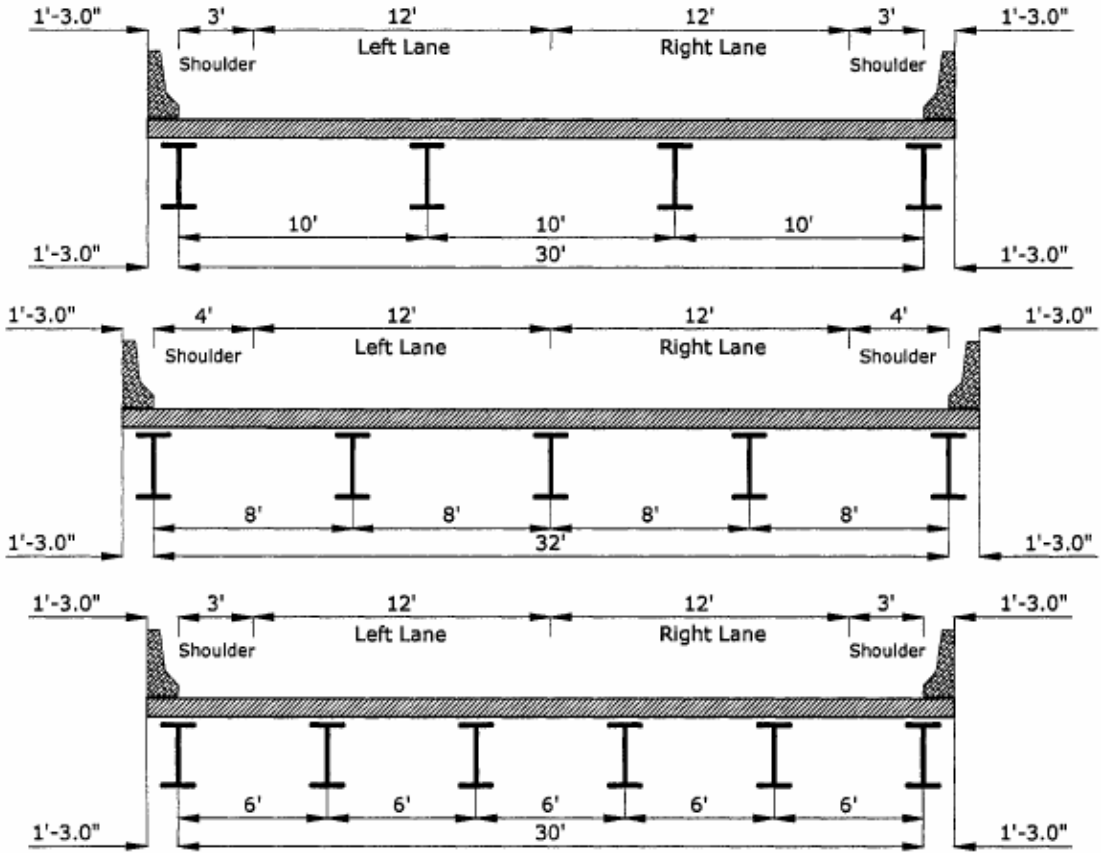

Figure 2.14: Steel I-girder bridge cross sections [Czarnecki & Nowak 2006]

Czarnecki examined bridges of the three cross sections shown for six different lengths ranging between 12.2 m to 42.7 m. For each section type and span, he also used different girder sizes to create structures with reliability indices under, over, and equal to the target reliability index (β_T).

Regarding the corrosion penetration rate equation, in [Czarnecki & Nowak 2006] the modelling is done assuming painted carbon steel, and so the corrosion penetration line is essentially divided into concave and convex parts to take into account, first, the degradation of the coating, and after this, the progression of corrosion penetration. This is shown in Figure 2.15.

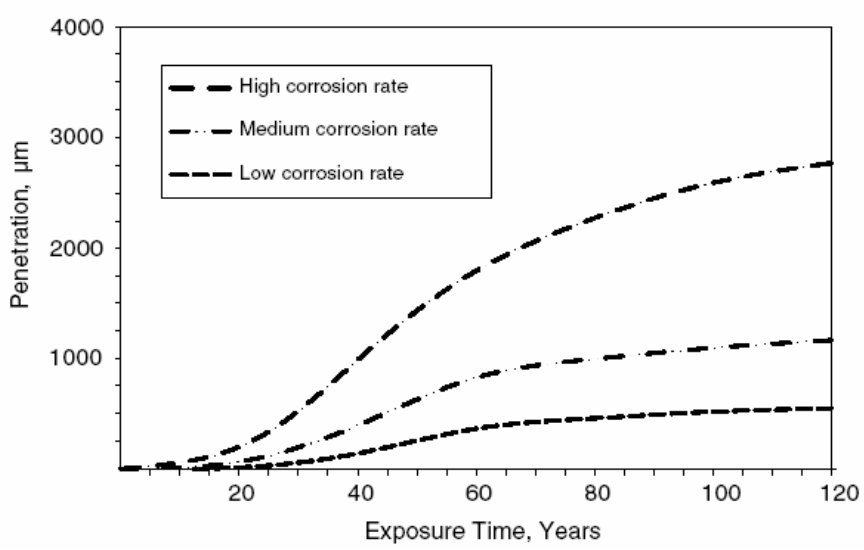

Figure 2.15: Corrosion rates for research of [Czarnecki & Nowak 2006]

The corrosion penetration curves in Figure 2.15 were selected based on both field observations and the data in [Albrecht & Naeemi 1984]. The high corrosion rate represents an industrial or marine environment or one where de-icing salts are used, while the low corrosion rate is for dry areas with little chemical contamination.

Regarding the locations on the bridge subject to corrosion, Czarnecki thought the approach used in [Kayser 1988, Kayser & Nowak 1989] was too refined; basically, there are too many variables that determine corrosion spread and penetration, and so the prediction is not realistic, he argues. Preferring a more general approach, [Czarnecki 2006] supposes surface loss due to corrosion over the entire web and top of the bottom flange for the whole bridge span, as shown in Figure 2.16.

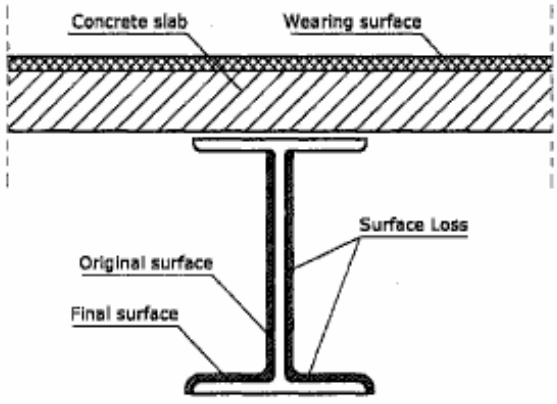

Figure 2.16: Corrosion location [Czarnecki 2006]

Czarnecki's work examined the effects of corrosion on the reliability of the system as a whole rather than any part of it. Depending on the configuration of the structure, considering system behaviour can result in a more reliable structure due to the fact that when a member is stressed beyond its capacity it is not removed from the structure; rather, the excess loads are distributed elsewhere. The type of computation required for this analysis is considerably complex; in this case, bridge models were built using a dedicated structural engineering program. A nonlinear model was applied to account for stress and load redistribution that occurs when a member progresses from the state of local yielding to ultimate, and from there to where the bridge fails.

Three limit states were checked: member failure, total bridge collapse, and a serviceability limit state (i.e. excessive deflection equal to 0.0075 of the span length). Analyses were performed for ultimate limit states (moment and shear) and serviceability (deflection), and structural performance was measured in terms of the reliability index.

It was found that reliability models provide a real benefit by facilitating estimations of the time-dependent bridge deterioration. While the low corrosion rate had a negligible effect on the bridge performance, a high corrosion rate significantly reduced the bridge capacity over time. It was further found that bridge reliability decreases much more rapidly for shorter spans compared to longer ones. Figure 2.17, Figure 2.18, and Figure 2.19 show the decreasing system reliability of bridges as their spans become shorter.

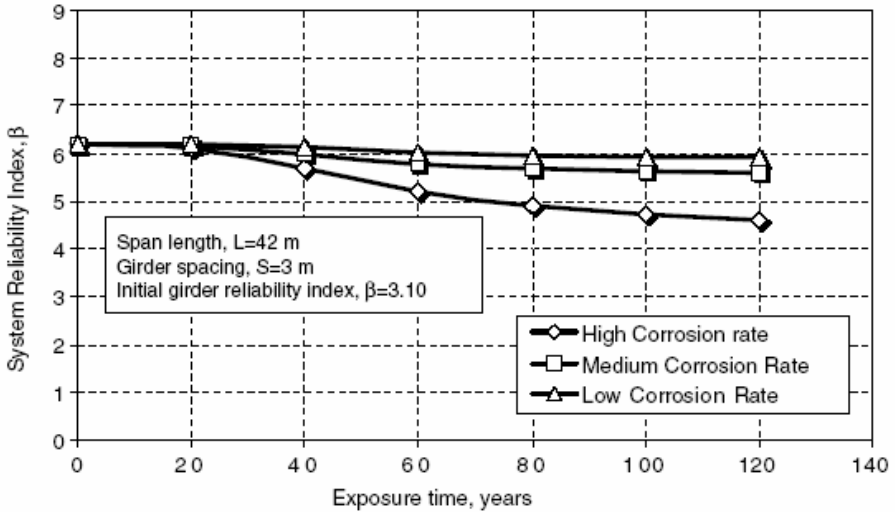

Figure 2.17: System reliability for long span bridge [Czarnecki & Nowak 2006]

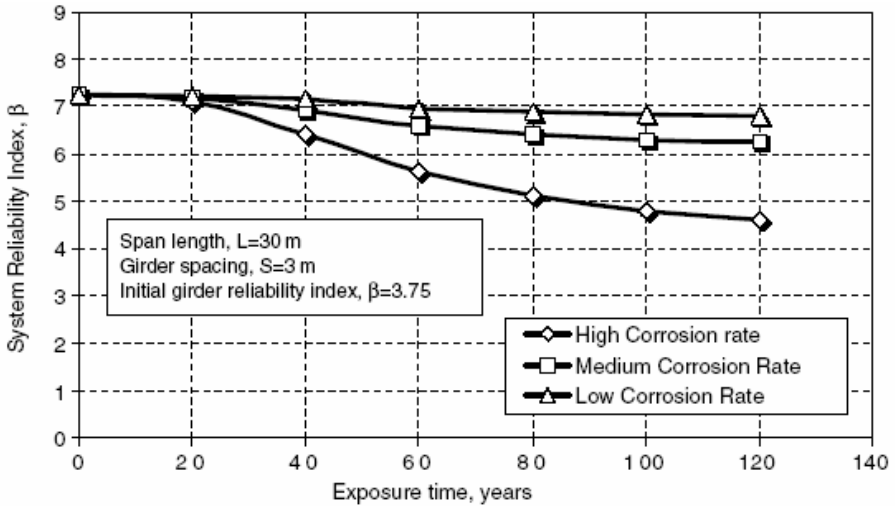

Figure 2.18: System reliability for medium span bridge [Czarnecki & Nowak 2006]

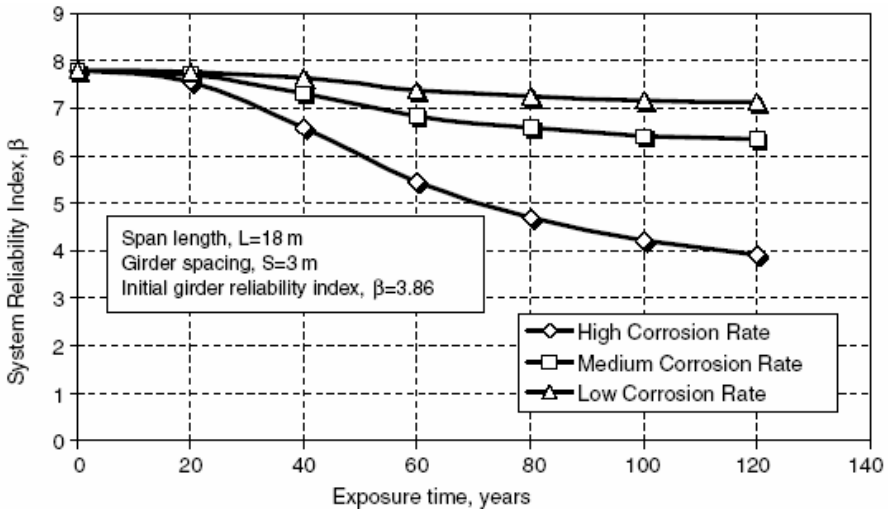

Figure 2.19: System reliability for short span bridge [Czarnecki & Nowak 2006]

A sensitivity analysis was also performed by Czarnecki, which showed that the statistical parameters related to the structural steel had a more noticeable effect on the structural behaviour than those parameters related to the concrete slab.

2.5.3 Research of M.S Cheung and W.C. Li

Cheung and Li [2001] looked at bridges of varying lengths with five rolled steel or built-up I-girders. Figure 2.20 below shows the arrangement of the girders and concrete slab.

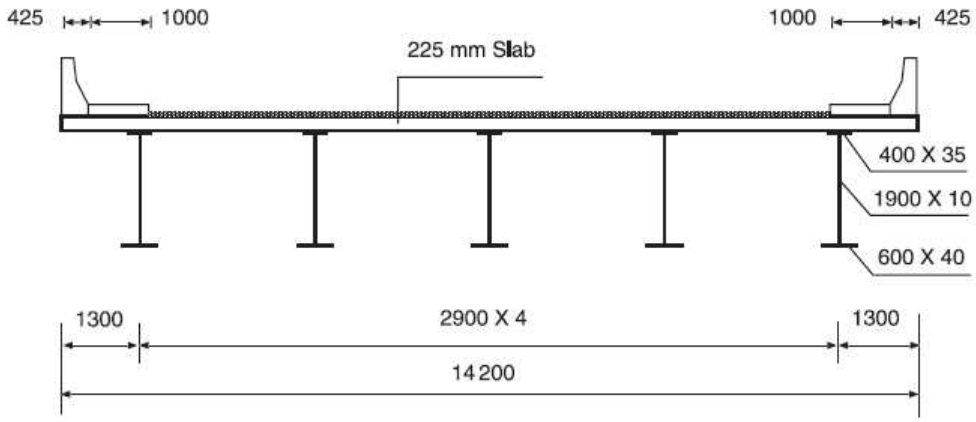

Figure 2.20: Structural arrangement [Cheung & Li 2001]

The same corrosion model (i.e. corrosion rate and location) as the one used by Kayser was applied here. The finite strip method was used in [Cheung & Li 2001] to determine the effect of corrosion on the serviceability of the structure, i.e. based on its deflection. The finite strip method uses beam eigenfunctions to express the longitudinal variation of displacements. This method requires the creation of a finite element model of the bridge cross-section in order to develop a stiffness matrix for the section as a whole. Figure 2.21 shows a typical finite strip model of the bridge section. As an analysis method, the finite strip method is more universal and more accurate than beam theory, and requires much fewer calculations than a full finite element model.

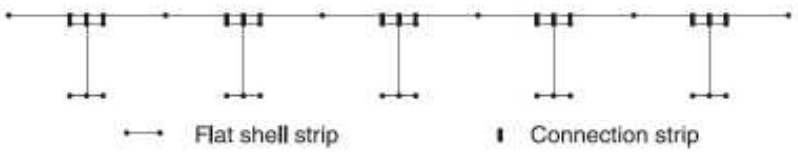

Figure 2.21: Finite strip model [Cheung & Li 2001]

In [Cheung & Li 2001], the *A* and *B* corrosion parameters, the thickness of the slab, and the moduli of elasticity of steel and concrete were varied in order to determine their effect on the time-dependent bridge reliability. Based on this work, it was found that, even if the nominal corrosion rate was low, corrosion still had a profound effect on the bridge serviceability, due to the fact that some corrosion rates had a large variance, so it was still possible to have high rates of corrosion penetration on occasion.

2.5.4 Research of P. Laumet

Laumet [2006] focussed on the deflection limit state of composite girder bridges. As with the above studies, the structures were single-span, I-girder bridges. Bridges with span lengths between 15.3 and 39.7 m, and girder spacing between 1.83 and 3.66 m, were considered. His models take into account nonlinear behaviour of the structural materials, i.e., the creep and shrinkage of the concrete slab and plastification of the steel girders. In [Laumet 2006] the logarithmic power model (see Equation 2.3) is used to predict the corrosion penetration. Only general corrosion is considered.

It is found that corrosion has a significant effect on the reliability of the bridge. Interestingly, it is also suggested that the deflection limit state should not be considered as a reliability limit state; on the other hand, steel yield is a valid reliability limit state, according to this reference. The reason for this is that the deflection limit state (*L*/800 is used here) does not correspond to any actual structural state, and since the bridge will frequently experience traffic loads that are larger than those predicted by the design codes, the structure's reliability index will show negative values.

2.5.5 Research of C.H. Park

The purpose of the research done by Park [1999] was to determine the effects of time dependent loads and corrosion on bridge reliability. The structures examined in this reference were composite I-girder bridges, between 10 and 30 m long, 12 m wide, and supported by a varying number of girders. The bridge structures were also examined as systems to determine their safety reserves as such. The model used in [Park 1999] is shown in Figure 2.22.

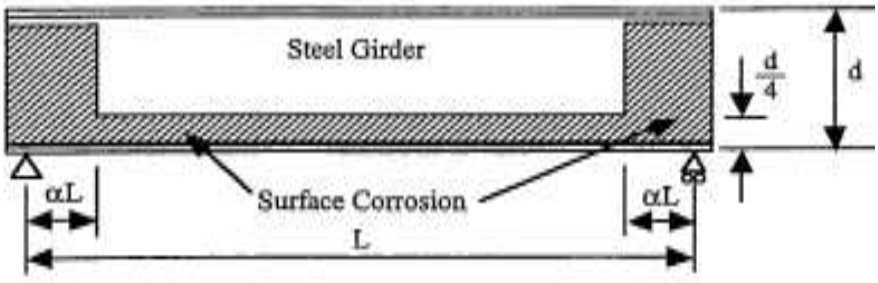

Figure 2.22: Corrosion locations [Park 1999]

As a preliminary part of his research, Park varied the $\alpha \cdot L$ value (shown in Figure 2.22) between 1.0 and 3.0 m, and found that doing so did not affect the reliability of his bridge model. The same corrosion model is used here as in [Czarnecki & Nowak 2006] (see Figure 2.15). Failure due to shear was found to be a more immediate threat to the structure than that due to moment. In fact, for short-span bridges, shear buckling is the governing failure mode at the maximum lifetime of the bridge. Sections with thinner webs are obviously more susceptible to web failure, and so it is recommended that web stiffeners be used. Importantly, it was found that the reliability of the bridge as a system was significantly higher than that of the individual components.

2.5.6 Other Research

Included in this section are structural reliability studies that either did not consider the effects of corrosion or did not examine the bridge structure as a whole.

Research of Sarveswaran et al.

Sarveswaran et al. [1998] also looked at the effect of corrosion penetration on component reliability: rather than considering composite I-girder structures, the research examined steel members alone. However, interval probability theory was used to determine the system reliability. In [Sarveswaran et al. 1998] only structures with known amounts of section loss due to corrosion are considered, due to the difficulty and uncertainty of predicting future corrosion penetration. For the general model, section loss occurs to the entire steel section, but at an advanced rate for the bottom ¼ of the web and the flange. Corrosion was also expected to attack both the top and bottom surfaces of the flanges. A diagram of the resulting beam section is shown in Figure 2.23.

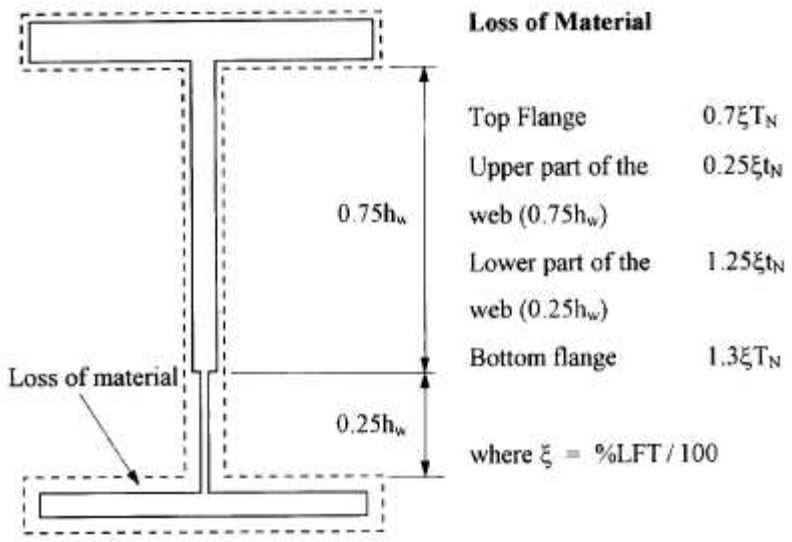

Figure 2.23: Beam section [Sarveswaran et al. 1998]

The findings of [Sarveswaran et al. 1998] are that the most critical failure mode affecting the beam is lateral-torsional buckling, due in part to beam coping. This is followed by shear, since the loss of material affects the bottom quarter of the web most directly, and then by moment, since section loss to the compression flange is less significant.

Research of Eamon and Nowak

Eamon and Nowak [2004] attempted to evaluate the effect of secondary elements, such as sidewalks and barriers, on the system reliability of girder bridges, assuming these elements participate in resisting live loads due to truck traffic, but also contribute to the dead load on the span. The effect of corrosion penetration over time was not considered. The study considered two-lane structures with varying numbers of I-girders and varying in length from 10 to 50 m. The results of [Eamon & Nowak 2004] show that the secondary elements did affect the reliability of the bridge structural systems. The effects varied with bridge span and girder spacing. Short-span structures showed the largest increases in reliability index, due to the additional capacity provided by the edge-stiffening elements. Figure 2.24 shows the effect of span length on reliability.

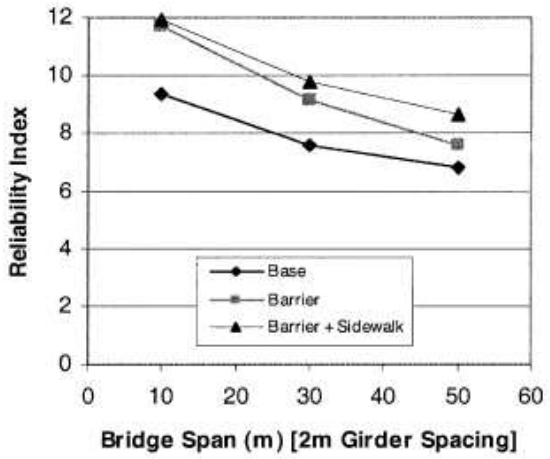

Figure 2.24: Reliability data for varying spans with 2 m girder spacing [Eamon & Nowak 2004]

Girder spacing was also found to influence reliability, but to a lesser degree. Since the number of girders affects system redundancy, structures with more, or more closely-spaced, girders had the highest reliability indices. Figure 2.25 shows these results.

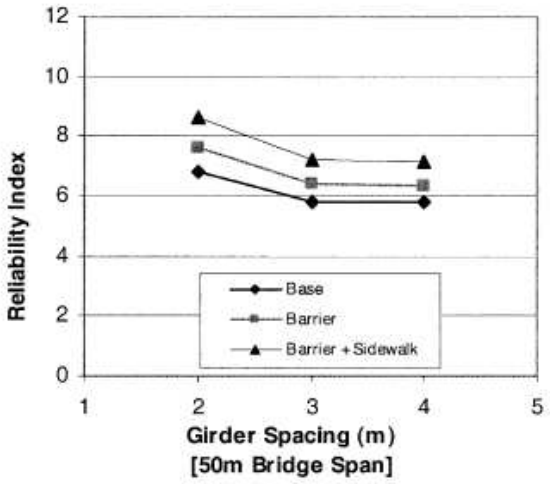

Figure 2.25: Reliability data for 50 m span [Eamon & Nowak 2004]

2.6 Summary

2.6.1 Corrosion of Weathering Steel

As mentioned earlier, there are some differing views on the exact nature and mechanism of corrosion penetration in weathering steel. Nevertheless, there is a consensus that its alloy content enables weathering steel to form a dense, uniform layer, which protects it from ingress of air, moisture, and pollutants that cause corrosion and lead to section loss.

2.6.2 Sacrificial Anode Protection of Weathering Steel

There has been research performed on the effectiveness of zinc and zinc-aluminum alloy metallizing as protective coatings for steel and concrete. These studies find that both are successful at protecting the substrate, even though they work in different ways. The zinc metallizing apparently wears down faster than the alloy alternative. However, no studies have been conducted that compare the effectiveness of these coatings on corroded, pitted weathering steel with the precision allowed by laboratory conditions. Also, no research on the effectiveness of zinc tape on a steel substrate was found.

2.6.3 Structural Reliability Evaluation

A significant amount of research has been carried out on the effects of corrosion on the time-dependent structural reliability of single-span I-girder bridges, including the consideration of system effects. However, no research has been done comparing I-girder bridges to box-girder bridges, or single-span bridges to two-span bridges. And, while the effects of span length and the number of girders have been researched with sensitivity studies, other factors, such as girder yield strength, the number of lanes, and the amount of traffic the bridge carries have yet to be considered.

CHAPTER 3: TESTS AND PROCEDURES

This chapter describes the laboratory tests conducted to assess and evaluate the accuracy of UTG measurements of corroded bridge plates and the benefit of metallizing and zinc tape as a means of reducing the rate of corrosion.

3.1 Ultrasonic Thickness Measurements

3.1.1 Background

Ultrasonic thickness (UT) measurement is the most common method of measuring the thickness of steel plate on a structure. The technique is as follows: a transducer is put in contact with the surface of the material being measured. The quality of the contact can be increased by the use of a couplant, usually a gel. The transducer emits ultrasonic waves that pass from a transmitter (T) through the material and reflect off the opposite wall and back to a receiver (R), providing there are no discontinuities or cracks that might first intercept the waves [Antaki 2005]. Figure 3.1 shows a diagram of this.

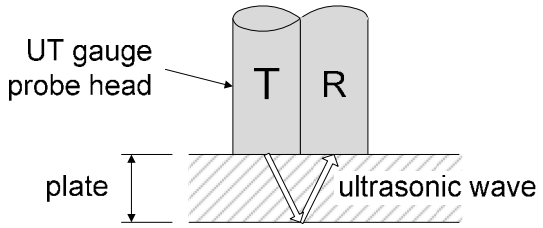

Figure 3.1: Explanation of ultrasonic thickness measurement

The main advantage of this system (versus the use of callipers, for example) is that it needs access to only one side of the plate being measured. However, there is significant uncertainty about what is actually being measured when the probe is placed on a heavily pitted surface or if there is a corrosion layer between the probe and the steel.

The goal of the research into ultrasonic thickness measurements performed for the current study was to determine the effectiveness and accuracy of UTGs when being applied to corroded steel plate. The effect of corrosion products (on either side of the plate) on the thickness measurement was studied, specifically whether the corrosion product was included in the thickness measurement of the steel. Also, the effect of pitting on the measurements was examined. As shown in Figure 3.2, it was necessary to design a test to

examine the effect of pitting, not only on the face being measured (thereby denying the UTG a smooth working surface), but also on the opposite face, in order to determine whether the distance to the pit or to the opposite face is what is being measured. Likewise, clear information could not be found in the existing literature on the effect of corrosion product (rust) on the reported thickness measurement.

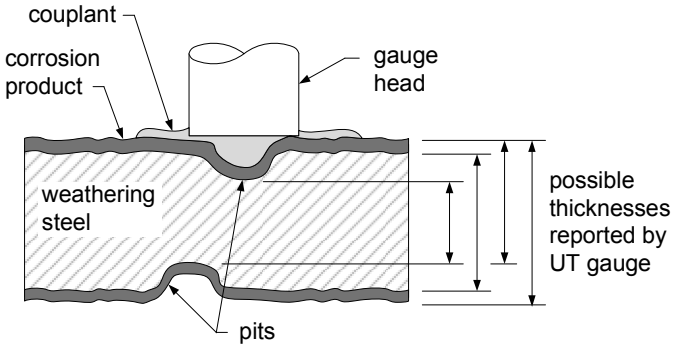

Figure 3.2: Explanation of uncertainty in ultrasonic thickness measurement.

3.1.2 Equipment

The Nova Eclipse TG110DL was the UTG used for this study; Figure 3.4 is a photograph of this instrument. The TG110DL has a built-in microprocessor for calculating the thickness of the material and a liquid crystal display for the visual interface. It is a handheld unit with the transmitter and receiver contained together in the probe that is applied to the material being tested (Figure 3.3).

Figure 3.3: UTG probe head

Figure 3.4: UTG and couplant

A variety of probes are available for use with this gauge, but for this project the Standard Probe (TG506) was the only one used. The gauge functions by sending a short ultrasonic pulse into the material and measuring the amount of time it takes for the signal to return after echoing off the back surface of the material. In calculating the material thickness, the gauge takes into account the characteristic ultrasonic velocity of the material. The gauge user's manual recommends a longitudinal ultrasonic velocity of 5.9 mm/μs for mild steel, and this is the value that is used for all measurements. The UTG results compared well with those provided by digital callipers and the Coordinate Measuring Machine described below. The couplant used was Sonotech Ultragel II, an ultrasonic couplant with a temperature range of -20° to 150° C.

A Mitutoyo BHN305 Coordinate Measuring Machine (CMM) was used to obtain measurements of the plate thickness with which the ultrasonic thickness measurements could be compared. The CMM (Figure 3.5) is a computer controlled measurement device used to measure the dimensions of three dimensional objects.

Figure 3.5: Coordinate Measuring Machine

It uses a needle-like probe to mechanically determine the x-, y- and z-coordinates of a point on the surface of the specimen. The probe can be manipulated directly by the user, or it can be directed to measure the object at a series of set locations or in a preset grid. It is programmable, so the user can enter a grid and let it run automatically.

The CMM does point measurements only, and not a continuous scan along a line. It is calibrated by measuring specimens of known dimensions. The surface profile measurements obtained with the CMM can be directly translated into thickness measurements if one side of the specimen is polished flat.

By comparing the UTG measurements with the physical measurements made using the CMM, it is possible to determine the level of accuracy provided by the UTG and, in particular, to determine the effects of pitting and corrosion product (on the front or back surfaces of the plate) on the measurements recorded by the UTG probe.

3.1.3 Tests

Machined Groove Thickness Measurement Test

Prior to measuring the thicknesses of corroded plate specimens, it was decided to test the ultrasonic gauge on a machined groove of known geometry. The steel used in this test was the taken from the "new weathering steel" sample provided by Algoma, as discussed in Section 3.3, with the corrosion product removed and all of the surfaces of the specimen machined smooth. For this test, the weathering steel specimen was first machined to a constant thickness. A groove (depth = 1.854 mm, radius = 3.175 mm) was then cut across the specimen to simulate a deep pit in the steel (Figure 3.6).

Figure 3.6: Steel specimen with groove

The specimen was then mounted onto an electronic height gauge that permitted vertical translation while measuring the change in vertical position to the hundredth of a millimetre. The UTG probe head was mounted on a three-prong swivel clamp and a magnetic clamp stand, allowing the sensor to be in contact with the specimen at all times. The full test setup can be seen in Figure 3.7.

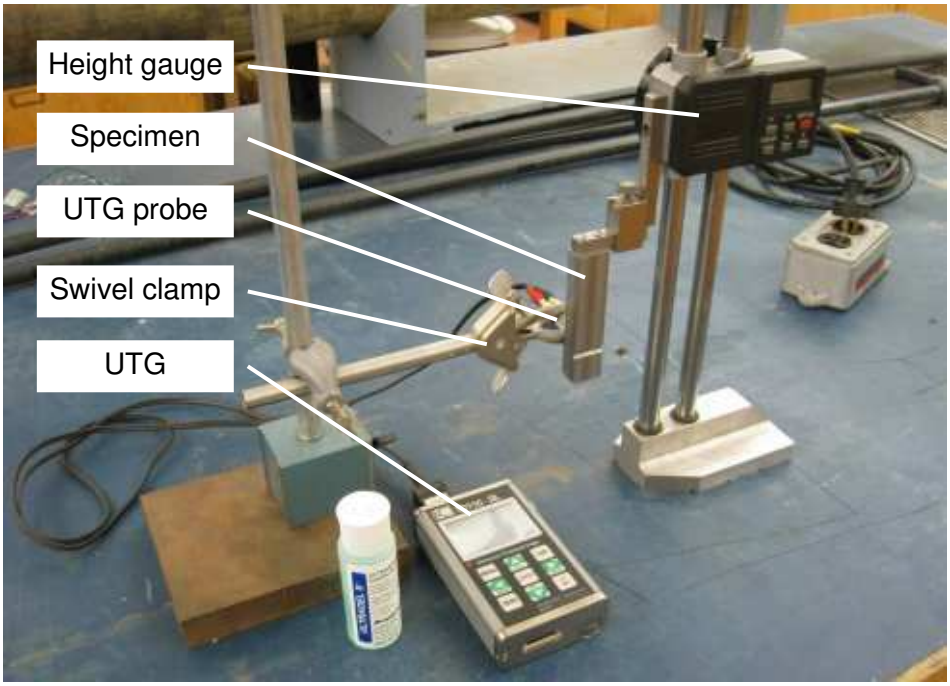

Figure 3.7: Machined groove thickness measurement test setup

To record the data, an arbitrary initial point above the groove was chosen and the thickness was recorded. The specimen was then moved across the UTG probe head and the position and the thickness value recorded at each location. This process was repeated until a complete line including the machined groove was measured. This test was run with the UTG probe head mounted in two orientations, termed "parallel" and "perpendicular" (see Figure 3.8). The results of this test are presented in Chapter 4.

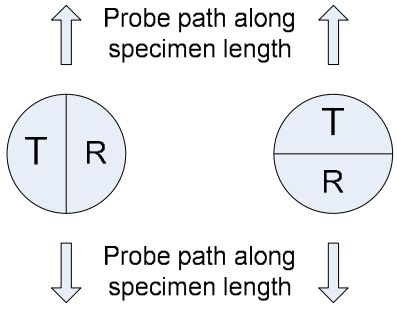

Figure 3.8: Parallel (left) and perpendicular (right) orientations of probe head

For this test, a circular irregularity was measured because it approximates the expected shape of a corrosion pit; however, for the purposes of the structural research, the shape of the pit is not as important as its depth.

Corroded Specimen Thickness Measurement Tests

The objective of the next series of tests was to determine the accuracy and limitations of the UTG when used to measure heavily corroded piece of weathering steel, specifically in view of the concerns discussed in Section 3.2.1.

For these tests, two types of specimens were considered, those with heavy corrosion and those with light corrosion. Figure 3.9 and Figure 3.10 are photos of typical specimens. Note that the heavily corroded specimens were "old steel" coupons cut from a larger sample taken from the Big Otter Creek Bridge; the lightly corroded specimens were "new steel" coupons cut from a sample provided by Algoma. The specimens were machined to a length of 90 mm and a width of 45 mm. The top, more heavily corroded, surface was initially left untouched, while the bottom surface was milled smooth.

Figure 3.9: "Old steel" specimen with heavy corrosion (old steel)

Figure 3.10: "New steel" specimen with light corrosion (new steel)

The UTG was used to perform a 5 x 7 grid of thickness measurements from both sides of the specimen. Special templates, shown in Figure 3.11, were used to control the location of each of the measurements to ensure repeatability. These plastic templates contained holes slightly larger than the probe head and a lip so that they would fit snugly over the 90 x 45 mm specimens, as is shown in Figure 3.12.

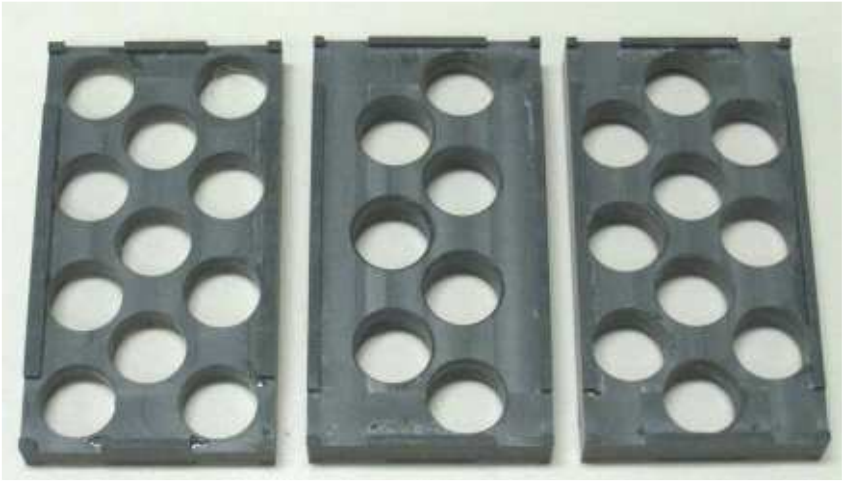

Figure 3.11: Templates

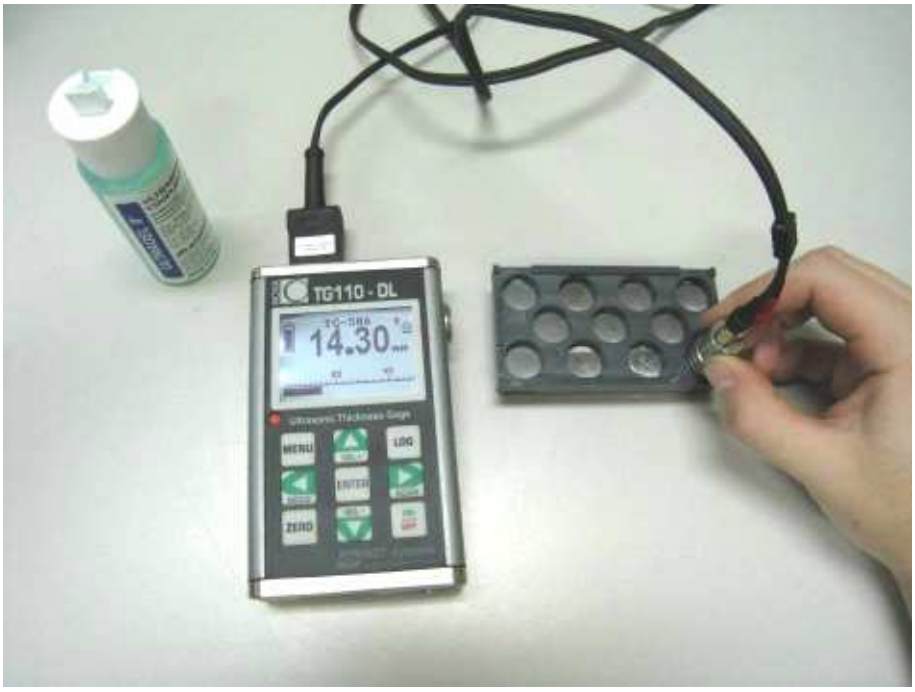

Figure 3.12: UT measurements with templates

Once the UT measurements were complete, the CMM was used to collect a 5 x 7 grid of thickness measurements at the center of each UTG measurement point. After these measurements were taken, the corrosion product was removed from each specimen by "pickling" as per [ASTM G1-03]. The clean specimens (Figure 3.13 and Figure 3.14) were examined under a microscope to ensure that the corrosion product was fully removed. Once cleaned, the UTG and CMM measurements were repeated.

Figure 3.13: Pickled specimen with heavy corrosion (old steel)

Figure 3.14: Pickled specimen with light corrosion (new steel)

In addition, the CMM was used to collect a data set in a 13 x 13 grid with a spacing of 1.5 mm between each measurement; the centre of this grid was located at the centre of the specimen. The results of this series of tests are also summarized in Chapter 4.

3.2 Corrosion Testing

3.2.1 Background

The objective of the corrosion testing performed for the current study was to examine the corrosion resistance of three different coating products. The test program was also designed to examine the effect of varying the level of sandblasting, the steel type, and the degree of corrosion damage to the surface prior to the coating.

3.2.2 Test Program

The test matrix for the corrosion testing is shown in Table 3.1. Five specimens of each type were used to ensure statistical viability.

Table 3.1: Corrosion test matrix

Group	Material	Corrosion	Treatment	Coating	Count
1	Old steel	Heavy	Full sandblast	None	5
2	New steel	Light	Full sandblast	None	5
3	New steel	Light	Full sandblast	Aluminum alloy metallizing	5
4	Old steel	Heavy	Full sandblast	Zinc metallizing	5
5	New steel	Light	Full sandblast	Zinc metallizing	5
6	Old steel	Heavy	Half sandblast	Zinc metallizing	5
7	New steel	Light	Half sandblast	Zinc metallizing	5
8	Old steel	Heavy	Full sandblast	Zinc tape	5
9	New steel	Light	Full sandblast	Zinc tape	5
10	Old steel	Heavy	Half sandblast	Zinc tape	5
11	New steel	Light	Half sandblast	Zinc tape	5

The test regimen chosen for the corrosion test was [SAE J2334]. This test regimen was originally designed for testing the corrosion resistance of automobile parts; however, it was used in the current study because of its known ability to induce significant corrosion thickness loss over a relatively short test duration, and due to the smaller area of steel required for the specimens. According to this regimen, this test follows a 24-hour cycle, as shown in Figure 3.15.

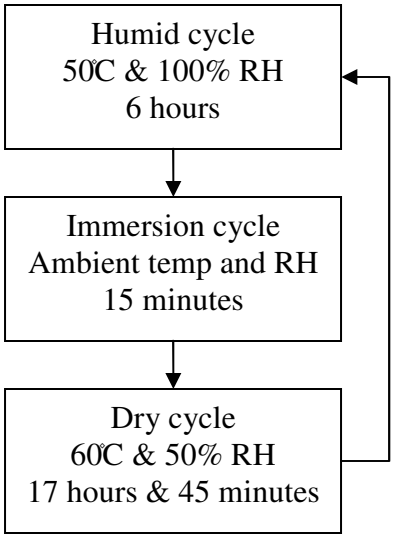

Figure 3.15: Test cycle [SAE J2334]

The composition of the [SAE J2334] immersion solution is as follows:

- 0.5 wt% NaCl
- 0.1 wt% $CaCl_2$
- 0.075 wt% $NaHCO_3$

Each of these constituents was obtained in solid (powder) form and dissolved in the distilled water that comprised the remainder of the solution.

Conductivity and pH were tested on a weekly basis to ensure the quality of the solution. An Orion Model 710A pH/ISE meter was used to test the pH of the solution; a Hach conductivity/TDS meter was used to monitor its conductivity.

3.2.3 Test Equipment

The test regimen was imposed by placing the specimens in an Ascott Cyclic Corrosion Test Chamber (model CC450). The system, which has a 450 L capacity, has two components: a corrosion chamber and a solution reservoir (Figure 3.16 and Figure 3.17).

Figure 3.16: Corrosion chamber

Figure 3.17: Solution reservoir

The Ascott system is programmable through a touch screen, and automatically adjusts the temperature, humidity, and immersion of the specimens. Its capacity for automatic operation means that it could operate continuously.

Test racks for the specimens were cut from black ABS plastic tubing. Figure 3.18 shows a diagram of the test rack (dimensions are in mm). The specimens were placed in a random order on the racks inside the corrosion tester. Once per week they were removed to be weighed and photographed (this was reduced to once per two weeks at the 120-cycle mark); they were then returned to the machine in a different order to ensure that their location inside the tester would not be a factor in their corrosion rate.

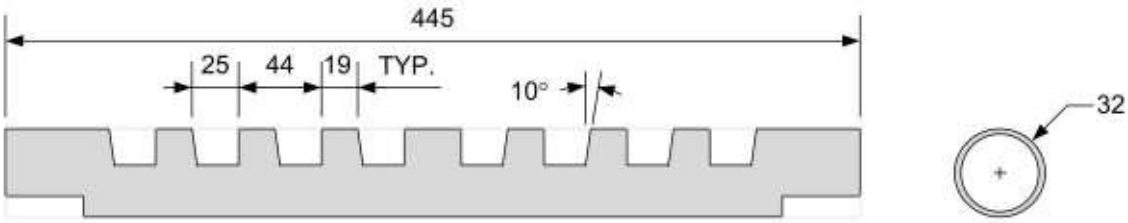

Figure 3.18: Test rack diagram

3.2.4 Specimens

Steel for the corrosion specimens came from two sources. The "old steel", provided by the MTO, came from a splice plate from the Big Otter Creek Bridge on King's Highway No. 3 near Tillsonburg, Ontario. Figure 3.19 shows a photo of the old steel in its "as received" state.

Figure 3.19: Old steel sample provided by MTO

The bridge drawings specify CSA G40.11 Grade 50A (yield strength, F_y = 345 MPa) atmospheric corrosion resisting steel. Inspections indicated this I-girder bridge, which is near Tillsonburg, Ontario, was experiencing very high corrosion rates and, as part of the repair procedure, some of the splice plates, as well as parts of the I-girder, were removed and replaced. This steel was observed to be heavily pitted and had lost some of its section. The section loss could be deduced because the steel under the bolt holes was not corroded, and the steel around them was much less thick. Figure 3.20 shows a photo of the profile of a pickled specimen cut from the old steel splice plate.

Figure 3.20: Bolt hole specimen (old steel)

Figure 3.21 shows an old steel (50 x 50 mm) specimen after sandblasting. As can be seen in this figure, the steel was heavily pitted as a result of its exposure and use.

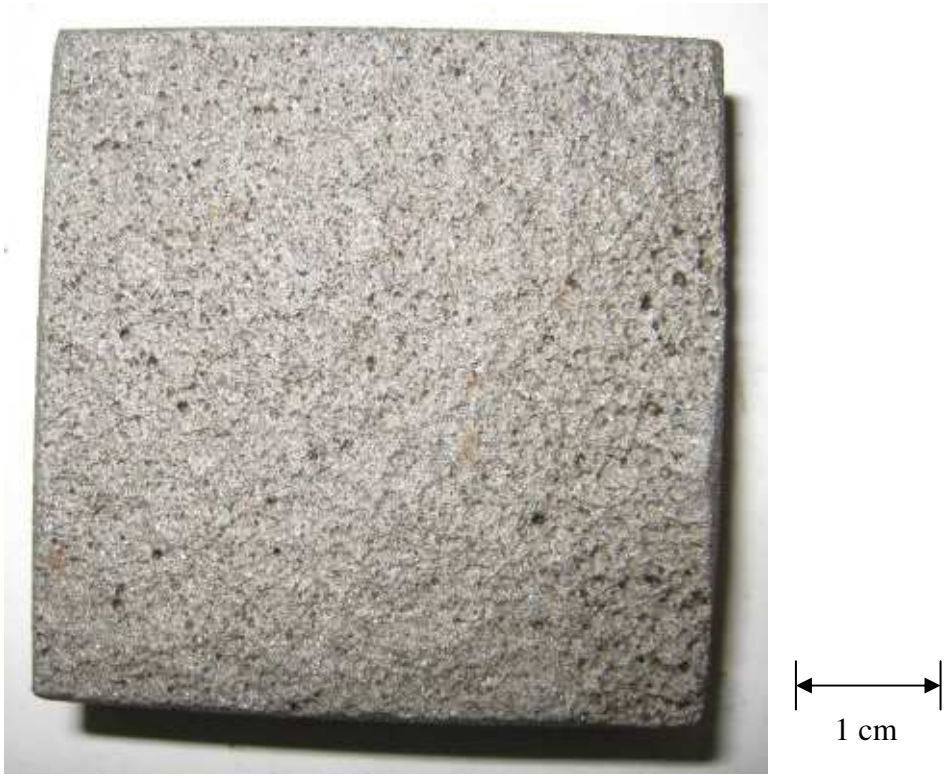

Figure 3.21: Old steel specimen

The "new steel" used in this study was provided by Algoma Steel. It is a weathering steel grade that is used in modern bridge construction, grade CSA 350 AT. Figure 3.22 shows

a photograph of the steel sample. The new steel was exposed outdoors to approximately six months of cold and wet environment with road salt and snow prior to testing. The effect of this exposure was a small amount of corrosion of the steel surface.

Figure 3.22: New steel sample provided by Algoma

Figure 3.23 is a close-up of a new steel specimen after sandblasting. The surface of the new steel specimen shows some texture, but is not pitted like the old steel specimen.

The chemical composition of each steel type was ascertained by testing in accordance with [ASTM D-1976 M] and [ASTM E-1019]. Testing was performed by Bodycote Testing Group of Burlington, Ontario. The results are summarized in Table 3.2, and the data are presented in a graphical manner in Figure 3.24. The current specifications for weathering steel according to [CAN/CSA G40.21] are summarized in Appendix A.

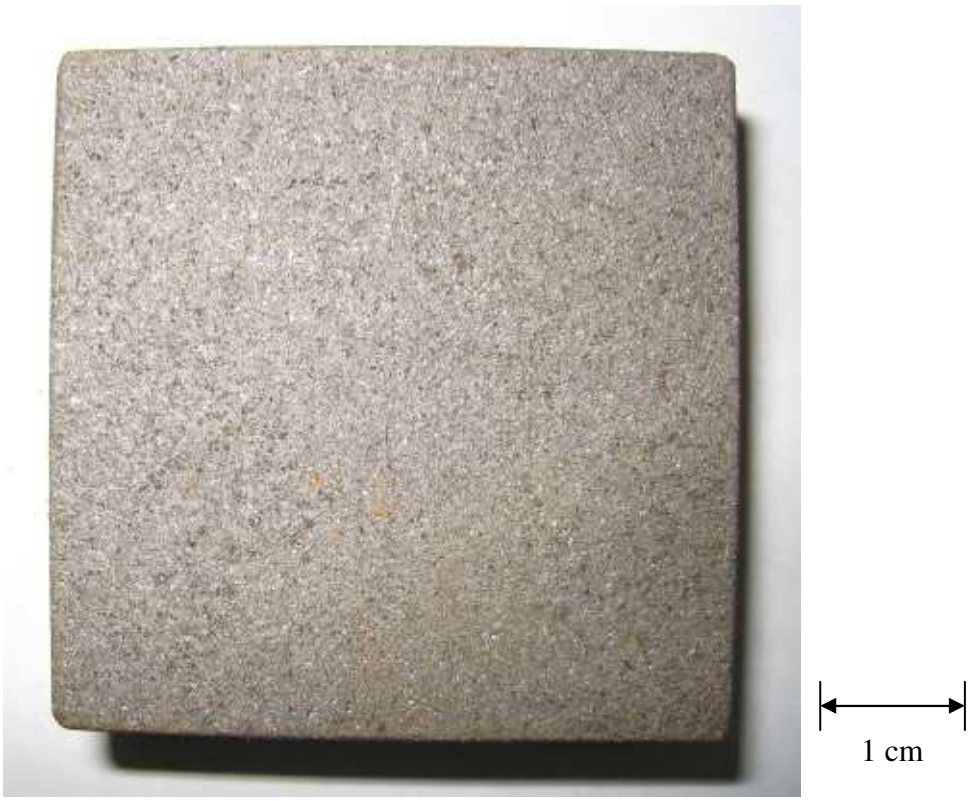

Figure 3.23: New steel specimen

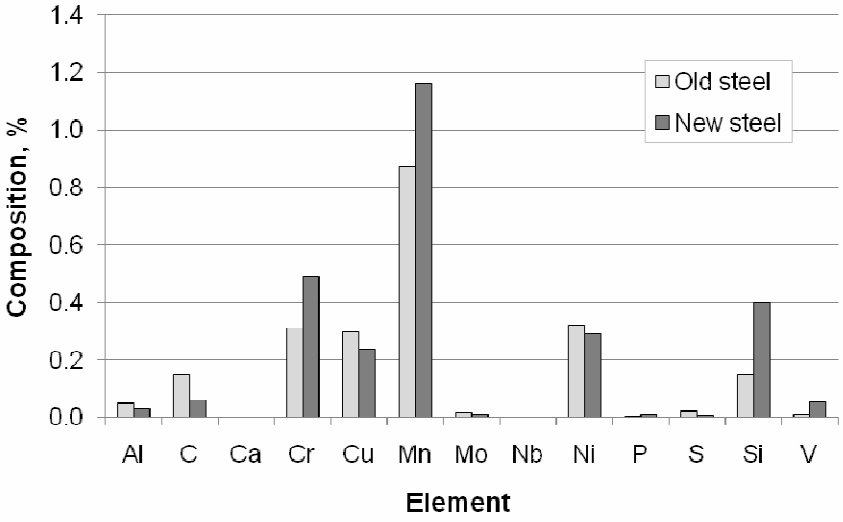

Figure 3.24: Percent composition of alloying elements

Table 3.2: Steel compositions, wt%

Element	Old Steel, %	New Steel, %
Al	0.05	0.03
C	0.15	0.06
Ca	< 0.005	< 0.005
Cr	0.31	0.49
Cu	0.30	0.24
Mn	0.87	1.16
Mo	0.02	0.01
Nb	< 0.005	< 0.005
Ni	0.32	0.29
P	0.005	0.011
S	0.024	0.006
Si	0.15	0.40
V	0.012	0.053

The old and new steels have a chemical composition that would qualify them as 350A or 350 AT steels (see Appendix A, Table A.1). The new steel contains significantly larger amounts of chromium, manganese, silicon and vanadium, but smaller amounts of carbon, aluminum, copper, and sulphur. The effects of these alloying elements are summarized as follows [Kulak & Grondin 2006, Albrecht & Naeemi 1984]: carbon increases the steel's strength and hardness, but tends to decrease its ductility and toughness. Manganese increases strength and hardness in a similar manner, except that it also increases the toughness. Chromium, copper, nickel, and silicon all serve to increase the corrosion resistance of the steel; manganese likewise has a beneficial effect on the corrosion resistance. Silicon and aluminum may also be present as deoxidizers, while vanadium is an effective precipitation strengthener. Phosphorus and sulphur are considered to be impurities and should be minimized if possible.

3.2.5 Pre-treatment

The old and new steel specimens were pretreated by sandblasting performed by a licensed contractor: Reitzel Brothers Sandblasting of Ontario. Thirty-five of the 55 total samples were sandblasted to a level compliant with [SSPC-SP 5/NACE No. 1]. The remainder of the samples were sandblasted to approximately half this level. The intent of this was to simulate an improperly sandblasted piece of steel in order to test the effect of sandblasting on coating effectiveness. In addition, it was thought that, if both specimen types performed equally well, then perhaps a lower cleaning criterion could be permitted, thereby reducing the preparation cost for the coating procedure.

3.2.6 Coatings/Treatment

As indicated in Table 3.1, three different coating products were applied to the weathering steel specimens. Each of these products operates as a sacrificial anode. All of the tape and metallizing products and procedures used for the current study were supplied and applied by Vector Corrosion Technologies.

Galvanic (Zinc) Tape

The tape product tested was Galvanode® ZincTape, and is comprised of three layers: the first (outer) layer is a topcoat of PVC, followed by a layer of high purity zinc (min. 99.99% zinc). The third is a layer of electro-conductive, pressure sensitive adhesive (the electrical conductivity is required to produce an electrical contact between the surface of the steel and the zinc tape). The adhesive is advertised to be capable of resisting a continuous temperature of 120°C, so there was no reason to expect a thermal breakdown of the adhesive to have an effect on the tape's performance.

The application of the tape is a straightforward process. Care has to be taken to prepare the surface correctly, either by scrubbing with a steel brush or sandblasting. Thin strips of tape have to be applied at the edges of the steel first, before the wider strips of tape can be used to cover up large, flat spaces between the edge strips.

Metallizing

Two metallizing products were examined in this study: zinc and aluminum alloy (see Table 3.1). The zinc metallizing product, like the zinc tape, is composed of high purity

zinc (min. 99.99 wt%). The aluminum alloy metallizing product is aluminum, 5.0 wt% zinc, 0.05 wt% indium, with additional small amounts of iron, silicon, copper, and manganese [D. Whitmore, personal communication, April 14, 2009].

3.2.7 Specimen Casing

Once the specimens were coated by Vector, they were subsequently encased on all but their top surfaces with epoxy to confine the exposure to the face of the specimen only. The epoxy used was the flowable two-stage SikaFloor® 261 system.

3.2.8 Control Tests

A control test was run in addition to the coated and uncoated steel specimens. This other test also took place under the [SAE J2334] test regimen. Four epoxy blanks of varying masses were tested in order to ascertain the effect (if any) of weight change associated with the casing material.

CHAPTER 4: TEST RESULTS AND INTERPRETATION

In this chapter the results of the tests made with the ultrasonic thickness gauge (UTG) are presented and analysed. Also presented are the results of the corrosion test which was performed with uncoated, metallized, and taped steel specimens.

4.1 Ultrasonic Thickness Measurement Tests

4.1.1 Machined Groove Test

In the machined groove test, the UTG was tested on a steel specimen with a machined semicircular groove. The test was run with the probe head in two different orientations, with the transmitter and receiver aligned parallel and perpendicular with respect to the gauge travel direction (see Figure 3.8).

Results

Figure 4.1 shows the thickness measurements made by the UTG with the probe in the parallel and perpendicular orientations, in comparison with the physically measured dimensions of the groove.

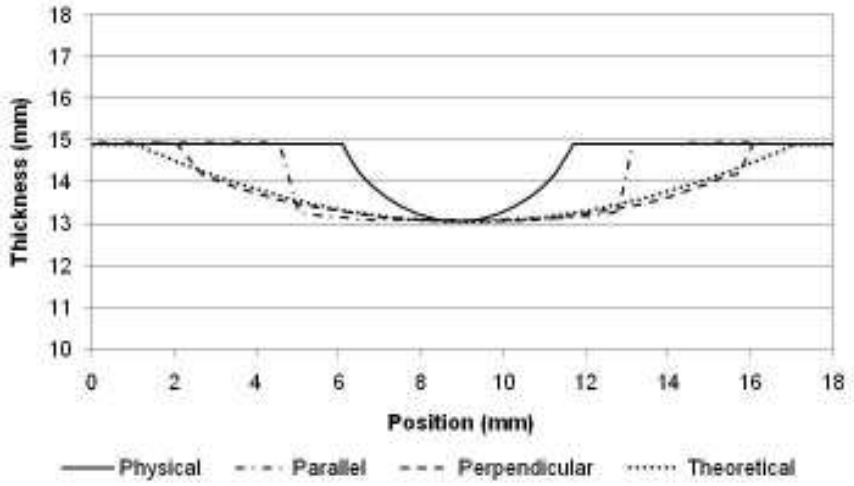

Figure 4.1: Machined groove test results compared with theoretical groove data.

The curve representing the physical measurements is based on thickness measurements of the specimen, measurements of width and depth of the groove, and an assumed circular cross section of the groove (the groove was drilled, so this assumption is expected to be realistic). The maximum depth and width measurements are presented in Table 4.1.

Table 4.1: Groove test measurements.

Measurement device	Depth (mm)	Top width (mm)
Physical	1.85	5.61
Parallel	1.85	8.22
Perpendicular	1.87	13.70

The UTG accurately measures the depth of the groove, regardless of the orientation of the probe; however, the measured width of the groove varies substantially and is not accurate.

Interpretation

The UTG works by transmitting and receiving ultrasonic pulses (see Section 3.2.1). These pulses, in the form of waves, return to the probe after reflecting from a discontinuity in the transmitting medium. They return at different intervals, depending on the distance travelled (assuming the transmitting medium is continuous); the UTG displays the calculated thickness based on the first wave to return. Once the distance to the edge of the groove is shorter than the distance to the opposite side of the specimen, this is the distance that is reported as the specimen thickness. Based on this assumption, a theoretical probe reading can be calculated for a given probe position. However, only surfaces perpendicular to the direction of the wave are able to reflect it back to the UTG receiver. Figure 4.2 shows the direct (A) and angular (B) paths.

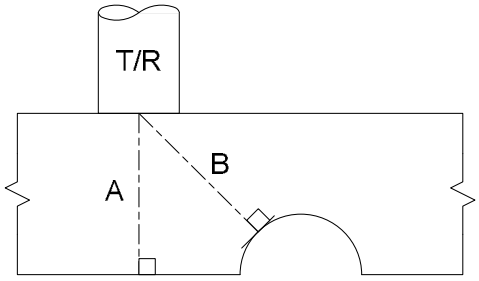

Figure 4.2: Ultrasonic wave paths

The shortest distance between the UTG and the opposing surface is the one used for the shortest distance assumption. Two lines based on the calculated or theoretical probe reading, based on the shortest distance assumption, are presented in Figure 4.2.

The theoretical UT values that were calculated were based on this "shortest distance" assumption. As can be seen from Figure 4.1, there is a noticeable similarity between the measurement made with the probe head in the perpendicular orientation and the theoretically shortest distance. The difference between the parallel and perpendicular orientation output is probably due to the fact that the instrument cannot register a weak return signal in the parallel orientation. Other factors that may have had an influence on both the parallel and perpendicular data are (1) the distance between the transducer and receiver and (2) the shape of the ultrasonic beam produced by the transducer, which, due to the shape of the transducer, is probably somewhat irregular.

Based on this study, it can be concluded that, the UTG output is reliable if it is being used to measure the thickness of a metal plate that is subject to general corrosion; however, the UTG is not well-suited for locating and measuring individual pits.

4.1.2 General Corrosion Measurement Test

In the general corrosion measurement test, the UTG was tested on steel specimens with varying degrees of corrosion. The specimens were first measured with the corrosion product present, and then again with the corrosion product removed by pickling. Each specimen was measured at 35 locations, and measurements were made three times to confirm their accuracy.

Old Steel Results

For the old steel, it proved impossible to measure the thickness from the corroded face of the specimen due to the heavy pitting; a relatively smooth surface is required for the UTG to take a reading. Thus, UTG readings were taken only from the back of the specimen only, which had been milled flat. CMM measurements were taken on the corroded face, which only measures the surface profile. However, if the side of the specimen sitting on the CMM table is perfectly flat, then the profile measurements can be equated to measurements of thickness. A summary of the statistical data for each of the readings is provided in Table 4.2.

Table 4.2: Old steel specimen thickness measurement data

Condition	Tool	Value	Spec. 3 (mm)	Spec. 4 (mm)	Spec. 5 (mm)
As received	UTG	Average	14.12	14.21	14.35
		Std. dev.	0.22	0.11	0.18
Pickled	UTG	Average	14.10	14.26	14.38
		Std. dev.	0.22	0.11	0.18
As received	CMM	Average	14.33	14.54	14.73
		Std. dev.	0.26	0.29	0.31
Pickled	CMM	Average	14.14	14.34	14.45
		Std. dev.	0.22	0.20	0.23

Figure 4.3 is a histogram showing the statistical distributions of the readings made with the UTG, taken before the corrosion product had been removed by pickling.

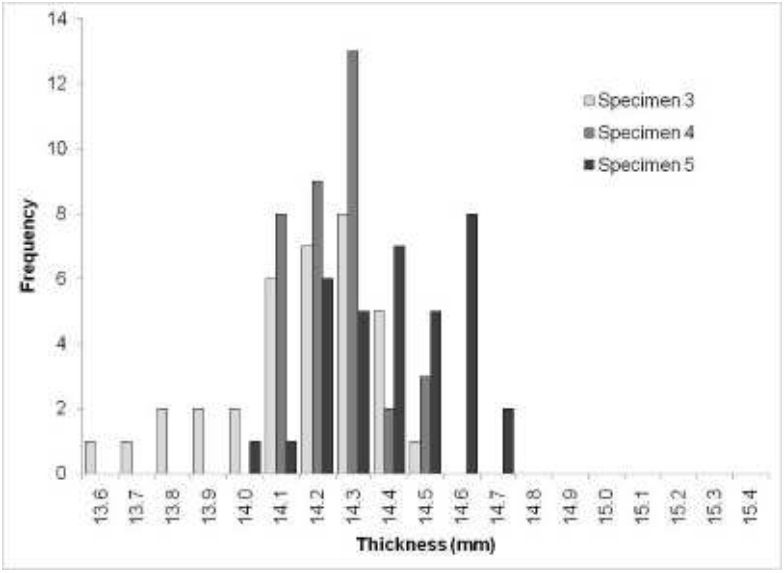

Figure 4.3: Histogram of as received old steel specimen thicknesses, by UTG

There is some variation in the data, which is probably due to the fact that the different specimens had experienced varying degrees of corrosion. Figure 4.4 is a histogram of the data collected with the UTG applied to the same three specimens after pickling.

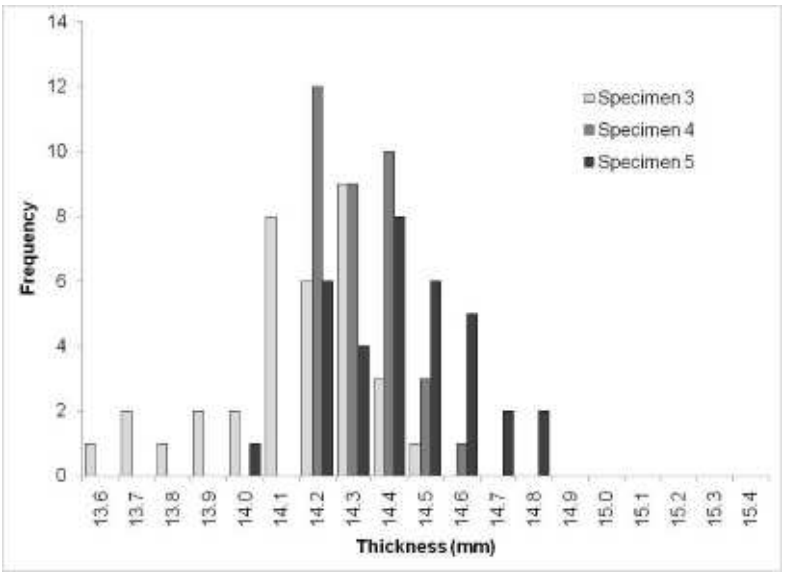

Figure 4.4: Histogram of pickled old steel specimen thicknesses, by UTG

Once again, there is a significant amount of variability between the individual specimens, but there is also a clear similarity between Figure 4.3 and Figure 4.4. The CMM was used to measure the same old steel specimens before and after pickling. Figure 4.5 shows a histogram of the plate thicknesses measured with the CMM from the corroded face of the old steel specimen before pickling. The data in Figure 4.5 collected with the CMM are more scattered than the UTG data.

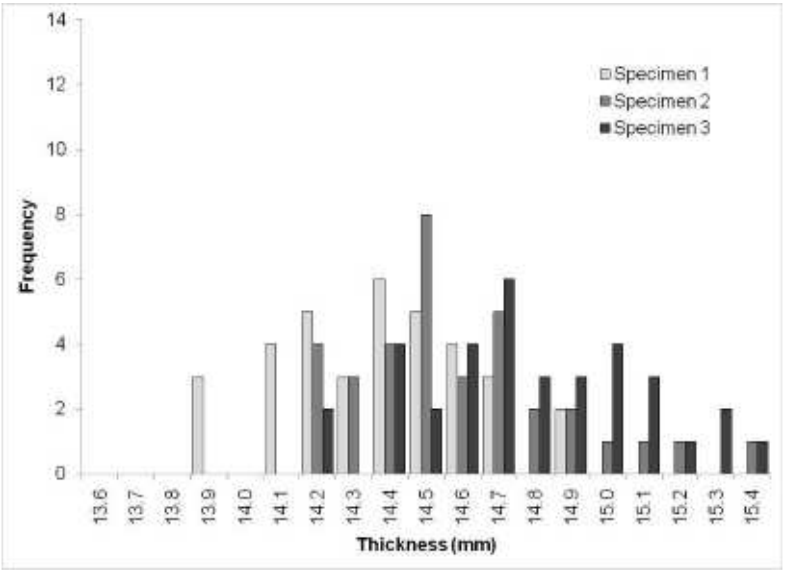

Figure 4.5: Histogram of as received old steel specimen thicknesses, by CMM

Figure 4.6 is a histogram of the data collected with the CMM from the corroded face of the old steel specimen after pickling.

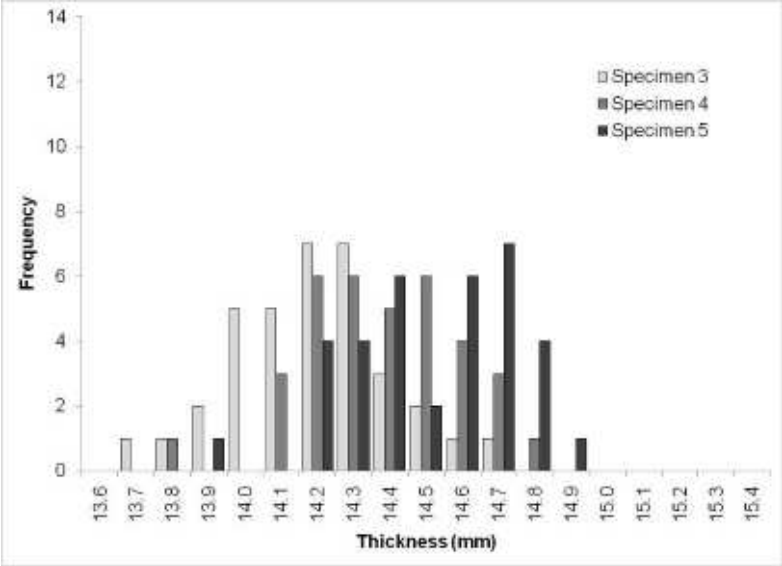

Figure 4.6: Histogram of pickled old steel specimen thicknesses, by CMM

Old Steel Data Interpretation

Table 4.3 contains the results of the average thickness before pickling ($t_{\text{as received}}$) minus the average thickness after pickling (t_{pickled}), as measured with the UTG and CMM.

Table 4.3: Comparison of old steel specimen thickness measurements

Δt	Spec. 3 (mm)	Spec. 4 (mm)	Spec. 5 (mm)
$t_{\text{as received, UTG}} - t_{\text{pickled, UTG}}$, mm	0.01	-0.05	-0.01
$t_{\text{as received, CMM}} - t_{\text{pickled, CMM}}$, mm	0.19	0.20	0.28

The CMM found 0.2 to 0.3 mm of corrosion product on the face of the corroded steel specimens on average. With the UTG, however, thickness measurements made from the uncorroded face before and after pickling are precise to within 0.02 mm on average, which is an acceptable error for this application. From this, it can be concluded that the UTG does not include the corrosion product in its measurements.

New Steel Results

The new steel, lightly corroded specimens were also measured with the UTG and CMM, both before and after pickling; however, in this case, the UTG probe was applied to the corroded face of the steel. Due to the relatively small amount of rust present, the UTG

was still able to measure the specimen thickness from the corroded side. A summary of the measurement data for the new steel specimens is available in Table 4.4.

Table 4.4: New steel specimen thickness measurement data

Condition	Tool	Value	Specimen 3	Specimen 4	Specimen 5
As received	UTG	Average Std. dev.	15.47 0.02	15.55 0.05	15.51 0.05
Pickled	UTG	Average Std. dev.	15.35 0.02	15.29 0.02	15.28 0.03
As received	CMM	Average Std. dev.	15.30 0.03	15.29 0.03	15.26 0.04
Pickled	CMM	Average Std. dev.	15.24 0.02	15.22 0.02	15.21 0.03

Figure 4.7 is a histogram of the data collected with the UTG on the three new steel specimens prior to pickling. The data in Figure 4.7 are quite closely grouped.

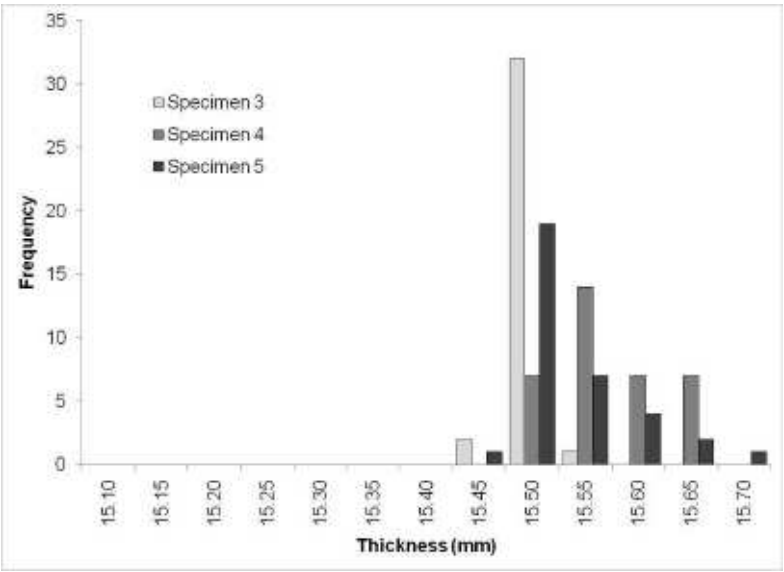

Figure 4.7: Histogram of as received new steel thicknesses, by UTG

Figure 4.8 is a histogram of the data collected with the UTG on the new steel specimens after they have been pickled.

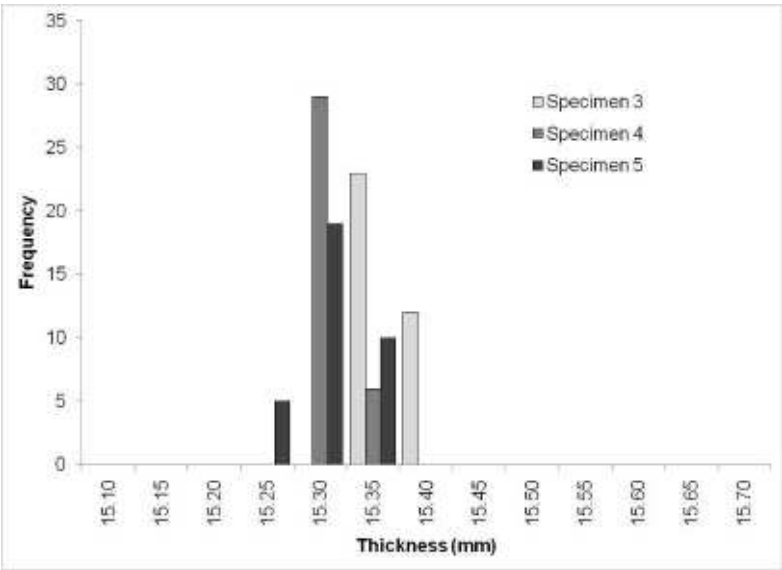

Figure 4.8: Histogram of pickled new steel thicknesses, by UTG

Once again, it is a tight group of data; however, the data are now significantly lower than what was collected with the rust still attached to the specimens. Figure 4.9 is a histogram of the data collected by CMM on the new steel specimen with the corrosion product still attached.

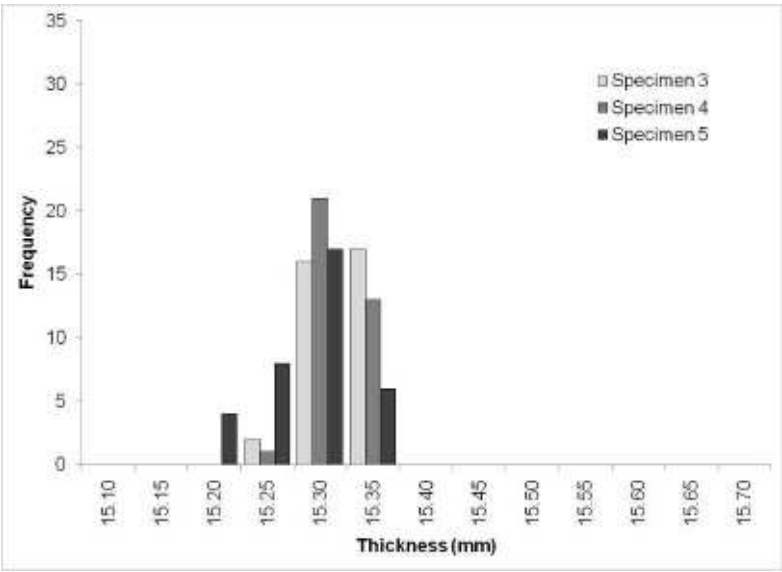

Figure 4.9: Histogram of as received new steel thicknesses, by CMM

Once again the data are quite tightly grouped, and the values are generally lower than those presented in Figure 4.7. Figure 4.10 is a histogram of the data collected with the CMM on the pickled new steel specimens.

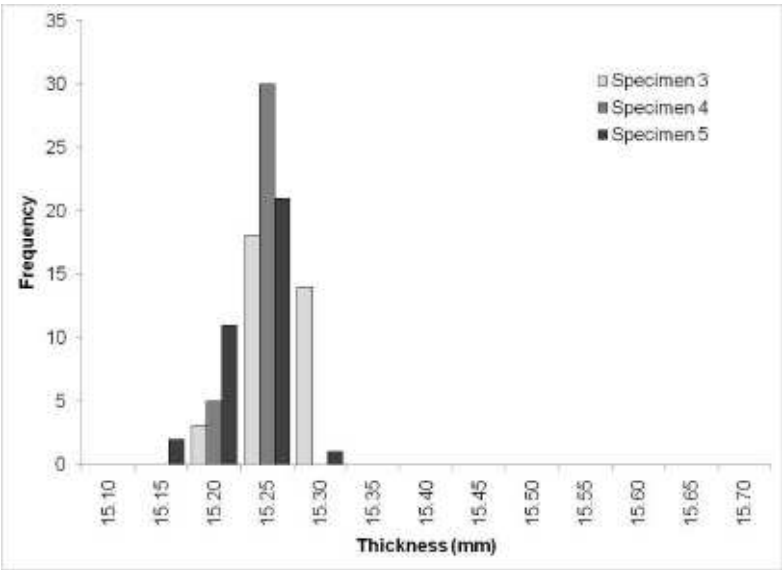

Figure 4.10: Histogram of pickled new steel thicknesses, by CMM

Again the data are quite tightly grouped, and in the lower range of values for these specimens. Comparing Figures 4.9 and 4.10, it can be seen that the average thickness, measured by the CMM, is slightly lower after the specimens are pickled.

New Steel Data Interpretation

Table 4.5 contains the average thickness before pickling minus the average thickness after pickling, as measured with the UTG and CMM, for specimens 3, 4, and 5. Note that in this case, all of the measurements have been made from the corroded side.

Table 4.5: Comparison of new steel specimen thickness measurements

Δt	Spec. 3 (mm)	Spec. 4 (mm)	Spec. 5 (mm)
$T_{\text{as received, UTG}} - t_{\text{pickled, UTG}}$, mm	0.13	0.26	0.23
$T_{\text{as received, CMM}} - t_{\text{pickled, CMM}}$, mm	0.06	0.07	0.05

It would appear from the data in Table 4.5 that the UTG overestimates the thickness of the steel by as much as 0.2 mm, approximately four times the thickness of the corrosion layer. This inaccuracy is caused by the rust coating on the specimen, through which the ultrasonic waves must pass twice in order for the plate to be measured. The rust layer is thin enough that the UTG still registers the returning energy, but is significantly less dense than the steel and, therefore, transmits the energy at a slower rate. Table 4.6 shows

the differences between the measurements made with the UTG and CMM on the pickled old steel and new steel specimens.

Table 4.6: Comparison of measurements taken with UTG and CMM on pickled specimens

$t_{\text{pickled, UTG}} - t_{\text{pickled, CMM}}$, mm	Specimen 3	Specimen 4	Specimen 5
Old steel	-0.04	-0.08	-0.08
New steel	0.11	0.07	0.07

In the measurements made on the old steel specimen, the UTG returned data that are on average 0.07 mm smaller than the CMM. However, in measurements made on the new steel specimen, the UTG data are on average 0.08 mm larger than the CMM data. There are two possible sources of error, which are given below.

With the old steel specimen, the CMM would have had to both find the pits and then have its needle fit into them; since the UTG was measuring from the smooth back of the specimen and uses a dispersive method of locating the shortest distance, the UTG measurements are smaller than those of the CMM. Using a microscope, numerous pit depths in excess of 1 mm were located on old steel specimens; pit measurement was accomplished by focussing on the rim and bottom of the pit and recording the difference between them. This is a probable source of difference for the old steel measurements.

Another possible source of error is with the UTG measurements of the new steel specimens. Since these measurements were being made from the corroded face, it is possible that the surface texture made it necessary for the ultrasonic waves to pass through a thicker layer of the gel couplant, which would increase the return time for the waves and result in an overestimation of the plate thickness.

4.2 Corrosion Tests

In this section the results of the corrosion test are presented. First a summary is made of any anomalies that were observed during the preparation and execution of the tests. The test results are then presented, and interpretations and conclusions are drawn from the data.

In order to distinguish the specimens, a shorthand system of nomenclature was developed, which is used throughout this section. Each specimen is labeled by three letters, followed by a number. The first letter denotes the type of steel (N or O, for new and old, respectively). The second letter is for the type of coating (Z, T, I, and 0, for zinc metallizing, zinc tape, aluminum alloy metallizing, and uncoated, respectively). The third letter is for the type of pre-treatment (W or R, for specimens sandblasted to a white or red condition, respectively). The number is for the individual specimen, ranging from 1 to 5. This code is used to identify the results on all the graphs in this section.

4.2.1 Test Preparation

The sandblasted samples were left exposed to ambient (laboratory) conditions after sandblasting and prior to coating. Within 24 – 48 hours, the steel samples sandblasted to white metal condition had lost their shine and began to show an orange tinge. The samples sandblasted to half-white condition also showed a low level of atmospheric corrosion. No attempt was made to re-clean the specimens.

Metallizing of specimens took place within a week of their being sandblasted. The zinc tape samples were taped approximately one month after the sandblasting was performed, while there were approximately six weeks between the sandblasting of the uncoated samples and the beginning of the corrosion test. During this time the uncoated samples developed a thin, dark orange layer due to atmospheric corrosion.

4.2.2 Test Execution

The full duration of the main corrosion testing program was 212 cycles.

Some unplanned events occurred during the corrosion test. First, at the 26 cycle mark, the corrosion tester partially shut down due to an equipment error, leaving the specimens in the tester for approximately four days with the atmosphere being adjusted normally (between 50°C/100% RH and 60°C/50% RH), but without being submerged.

Second, after some time, corrosion product was observed to have developed between the uncoated specimens and their epoxy casings, cracking the epoxy. This occurred on the sides and back of the specimens, and required removal of the epoxy and re-encasing of the specimens. This was performed after 47 cycles in the corrosion tester. After 82

cycles, the uncoated specimens were removed from the test. This was done because there was no reason to continue testing them; instead, the corrosion products were removed from four specimens (two new and two old) to measure the progress of the corrosion.

At regular intervals the corrosion tester had to be paused so that maintenance could be performed and specimens could be measured and examined. On these occasions, the chamber was opened and the specimens were exposed to ambient temperature and humidity for a short period of time.

4.2.3 Test Results

Figure 4.11 shows the mass gain/loss data collected through the full duration of the test. Each curve in this figure represents an average of the five specimens of each type. Graphs with the data for individual specimens are presented in Appendix B.

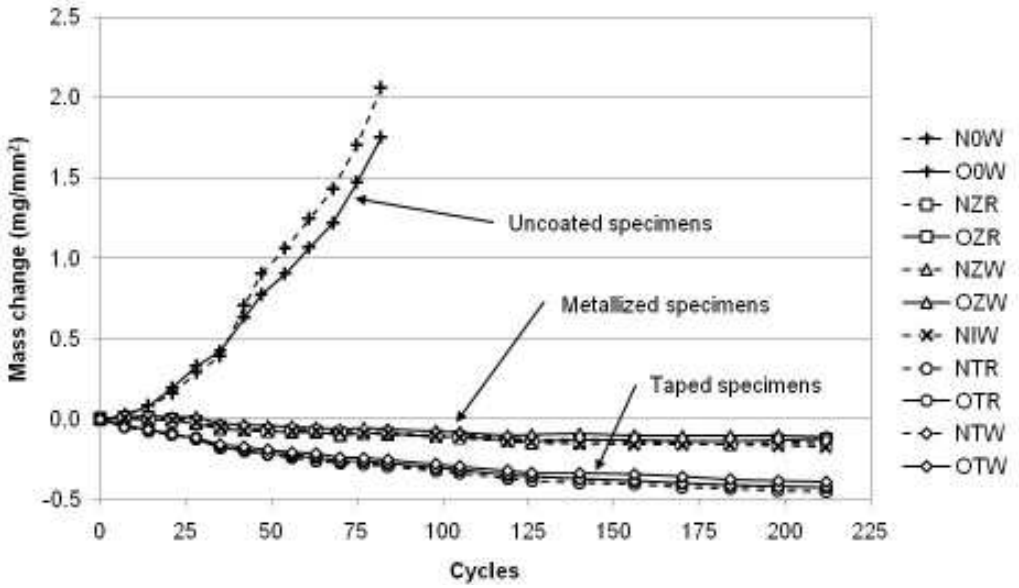

Figure 4.11: Corrosion test mass change results – general

The specimens immediately separated into three groups according to their coating type. The first group, the uncoated specimens, showed a dramatic increase in mass over the duration of the test. The second group, the metallized specimens, at first showed a slight increase in mass, but this was followed by a downward trend, which lasted to the end of the test. The third group is the taped specimens; these showed an immediate downward trend, which continued until the end of the test. The test results for each of these groups are discussed in detail below.

Uncoated Specimens

Figure 4.12 shows the weight gain of the uncoated specimens during the corrosion test. The uncoated specimens began corroding immediately. After 82 cycles they were removed from the corrosion chamber, due to the deterioration of the epoxy casings.

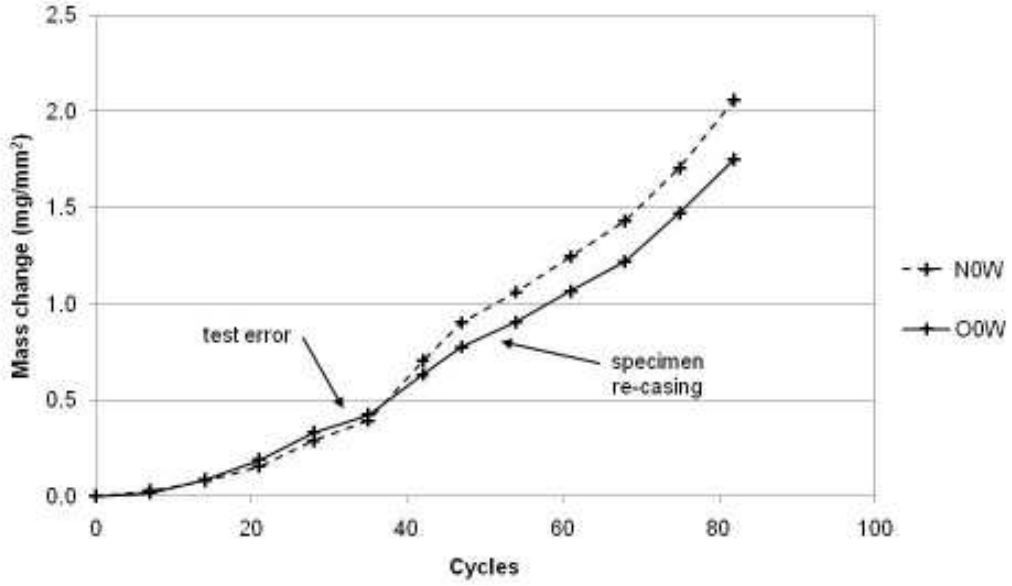

Figure 4.12: Corrosion test mass change results - uncoated specimens

In Figure 4.12, the mass change slope becomes steeper for both samples at the 35 cycle mark, and again at the 70 cycle mark. This may be due to the progression of corrosion through the sides and back of the uncoated specimens. Nevertheless, there is no indication from the data gathered that the corrosion would level off at some point in the future. Also, when the specimens were autopsied, it was discovered that most of the corrosion occurred on the exposed face rather than on the sides and back of the specimen.

Figure 4.13 shows two examples of the uncoated specimens prior to the start of the test.

Figure 4.13: Specimens N0W3 (left) and O0W1 (right), prior to test start

As can be seen from these figures, already at the start of the test (after blast cleaning) a small amount of atmospheric corrosion had occurred.

Figure 4.14 is a photo of the specimens after their removal from the corrosion chamber.

Figure 4.14: Specimens N0W3 (left) and O0W1 (right), after test conclusion

In Figure 4.14, the surfaces of the specimens are heavily corroded. The epoxy casings were removed from four of the uncoated specimens, which were then pickled in order to remove the corrosion products. However, it was discovered that once an uncoated specimen had been removed from the tester and left aside for a few days, the corrosion layer would come off as a single piece. Interestingly, this corrosion piece was very similar in appearance to the large flakes of corrosion product that can be found on and under a heavily corroded weathering steel structure. Figure 4.15 shows a specimen with a detached corrosion layer.

Figure 4.15: Specimen O0W1, after removal from tester, with rust layer detached

Raman and x-ray diffraction (XRD) tests were performed on corrosion samples from the old and new steel specimens in order to identify the components of the corrosion. Figure 4.16 shows the results from the Raman test performed on the rust layer of an old steel specimen.

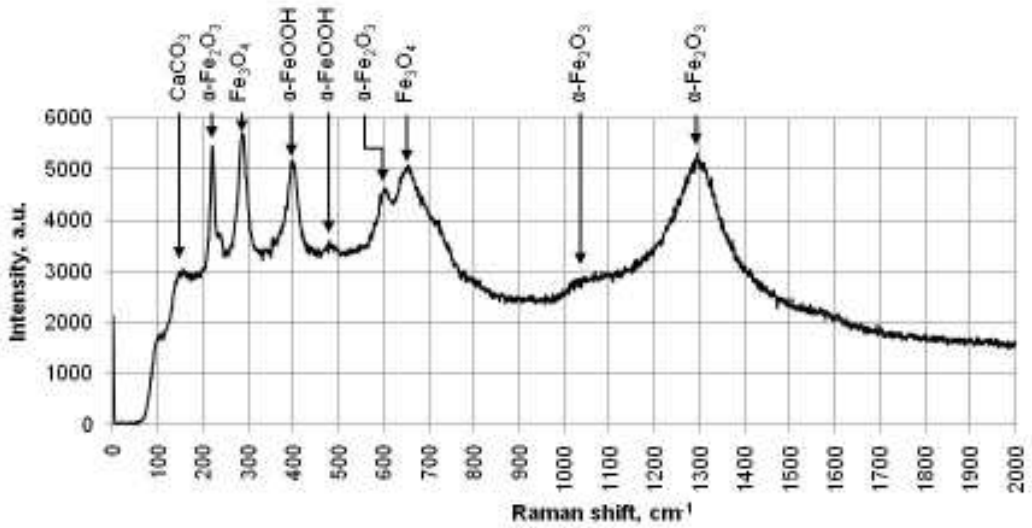

Figure 4.16: Raman test results for old steel rust

The main products are iron oxides and iron oxide-hydroxides. Calcium carbonate ($CaCO_3$) also appears as a deposit from the test solution. Figure 4.17 shows the Raman test results for the corrosion product of the new steel specimen.

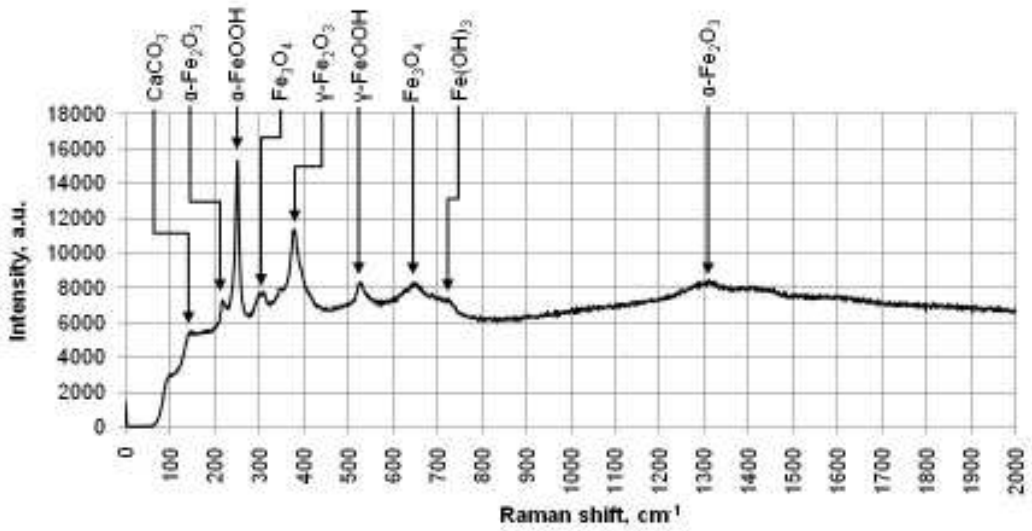

Figure 4.17: Raman test results of new steel rust

The results of the Raman test of the new steel rust are very similar to those of the old steel rust. Interestingly, β-FeOOH is not found among the corrosion products of either steel, in spite of the fact that it is supposed to result from corrosion that occurs in proximity to salt water, according to [Misawa et al. 1974].

Figure 4.18 shows the results of x-ray diffraction (XRD) tests on the corrosion products of the old and new steel specimens and a sample of corrosion taken from a weathering steel bridge situated on Highway 402 between London and Sarnia in Ontario. The results of all three tests showed a very large amorphous component; however, the data were reduced to provide the following graph (Figure 4.18).

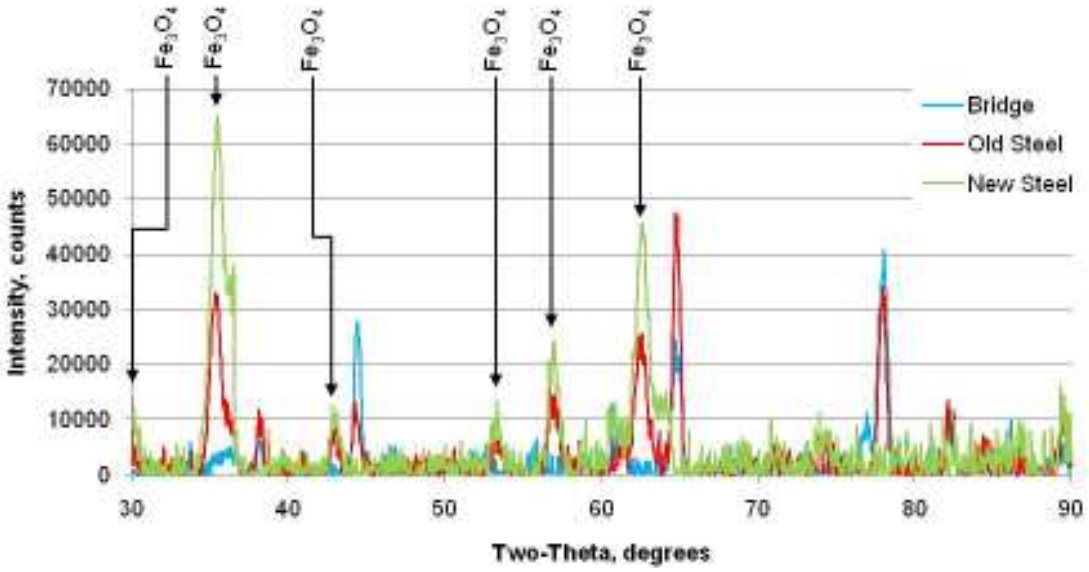

Figure 4.18: XRD results for new, old, and bridge steel rust

The only iron oxide identified with certainty was magnetite (Fe_3O_4). This iron oxide formed mostly on the old and new steel specimens, possibly as a result of their regular immersion in a salt solution. The results of the XRD test seem to indicate a greater similarity between the old steel rust and the rust from the overpass than that of the new steel.

The results of the weight measurements of corrosion products from four of the uncoated specimens can be found in Table 4.7. For these specimens, the weight of the rust layer was compared with the weight of all corrosion products combined. It was found that the rust layer comprised approximately 75% of the total weight of the corrosion product on average, so the total weight lost was multiplied by this factor to estimate the weight of steel lost from the face of the sample.

Table 4.7: Uncoated specimen mass and section loss

	w_o (g)	w_{pickle} (g)	W_{loss} (g)	t_{loss} (mm)
O0W1	354.6	339.0	15.6	0.57
O0W4	316.0	301.9	14.1	0.60
N0W1	375.6	359.6	16.0	0.59
N0W4	377.8	362.4	15.3	0.56

The thickness loss values were calculated based on the area of the exposed top surface and a steel unit density of 7.85 mg/mm^3. From the results shown in Table 4.7, it can be inferred that the old steel corrodes at a slightly slower rate than the new steel, confirming the trend shown in Figure 4.12; however, more tests are needed to establish this conclusively.

Metallized Specimens

Figure 4.19 is a graph of the mass change to the metallized specimens over the duration of the corrosion test.

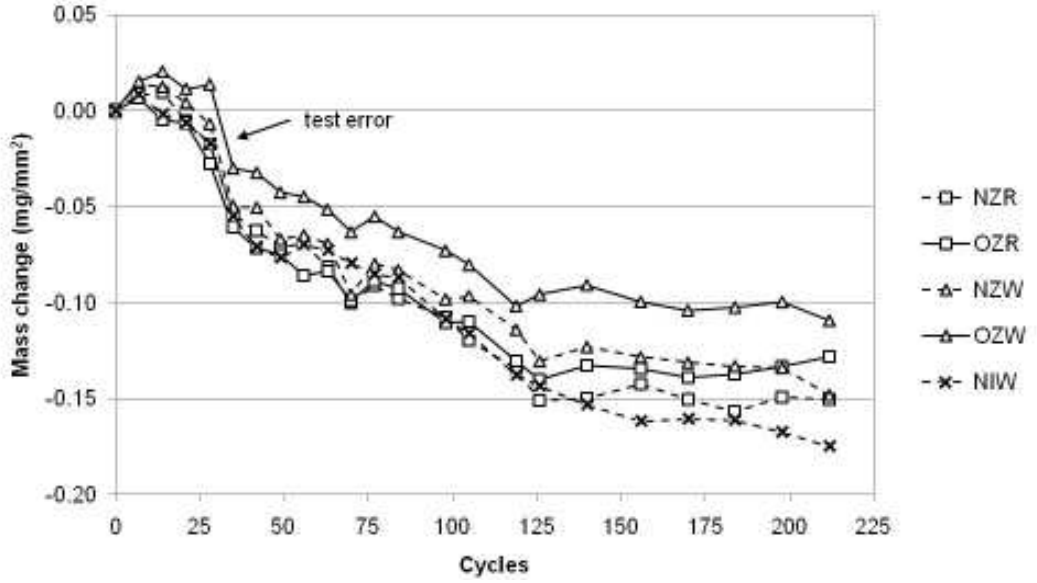

Figure 4.19: Corrosion test mass change results - metallized specimens

The metallized specimens essentially experienced three stages. The first, which lasted from the start of the test to about the 15th cycle, showed the specimens increasing in mass. In the second phase, from the 15th cycle to about the 110th, the specimens' mass

dropped rapidly, and the third, from approximately the 110th cycle to the end, showed the specimens had ceased to increase or decrease significantly in mass.

The specimen mass increase, which occurred at the start of the test, most likely is the result of the metallizing product forming an adherent corrosion layer. The specimen weight loss likewise occurs when the corrosion product washes off or detaches from the specimen.

Figure 4.20 shows two of the metallized specimens prior to the start of the corrosion test. Both specimens began the test with a coating of shiny metallizing product.

Figure 4.20: NIW3 (left) & NZR4 (right), prior to test start

Figure 4.21 shows the specimens after the test was completed. Both specimens lost their shine shortly after the start of the test.

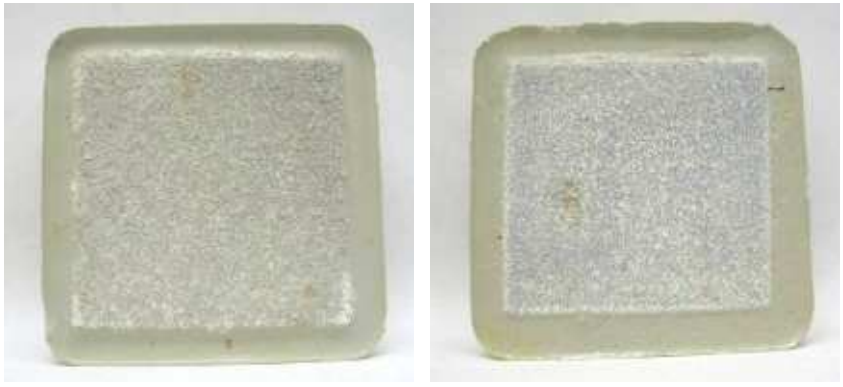

Figure 4.21: NIW3 (left) & NZR4 (right), after test conclusion; orange regions circled

Orange regions in the specimens in Figure 4.21 should not be construed as evidence of corrosion; under a microscope it is evident that they are in fact the result of rust particles that have washed onto the specimens from other sources in the corrosion chamber.

Autopsies of the metallized specimens showed that no steel corrosion was present due to invasion of salt solution along the sides and back of the specimens.

Figure 4.22 is a photomicrograph of a section of a zinc-coated steel specimen.

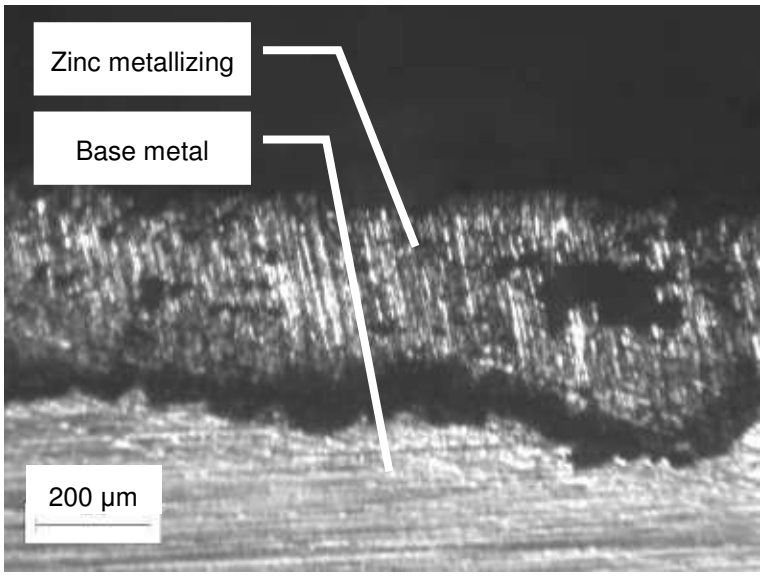

Figure 4.22: Photomicrograph of NZR5 section

In some locations, the zinc metallizing appears to have either been subject to pitting or else had some cavities as a result of the metallizing process. Nevertheless, in no location has the salt solution penetrated through the coating to the steel substrate. Figure 4.23 is photograph of an aluminum alloy-coated specimen section. The metallizing is difficult to see in part because the alloy is darker and less reflective than the zinc metallizing.

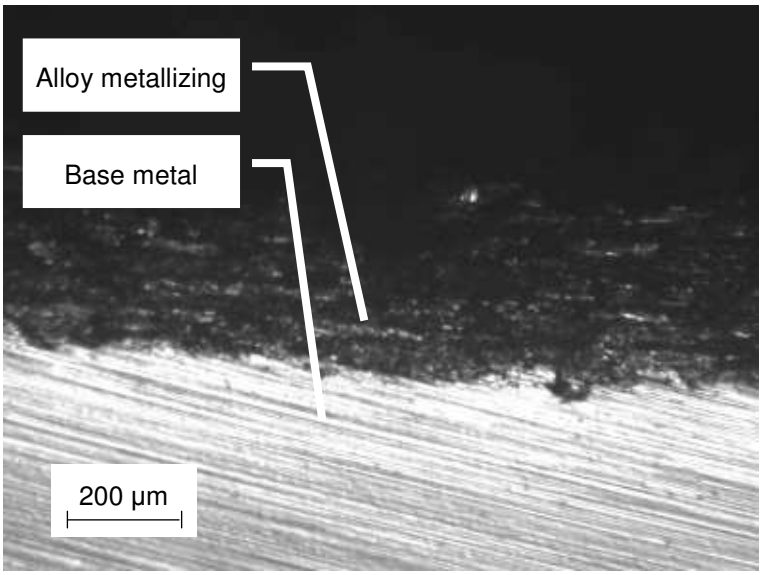

Figure 4.23: Photomicrograph of NIW2 section

In at least one location the metallizing was found to be absent, either because an uneven layer of product was applied or it had corroded away during the test; in any case, corrosion to the steel had yet to occur at this location.

The aluminum alloy coated specimens appeared, on average, to show a greater amount of corrosion product than the specimen coated with pure zinc, especially around the edges of the specimen. Also, these specimens showed a greater amount of mass loss than the specimens metallized with pure zinc. Together, this suggests that the aluminum alloy metallizing product is less effective than the pure zinc product when subjected to a high-chloride environment. However, it should be noted that one reported benefit of the aluminum alloy coating is its resistance to sulphur oxides, which was not examined in this test.

There was no indication that the mass loss rate would either increase or reverse at a later point in the test. Furthermore, there was no indication from the corrosion test that the degree of sandblasting had any effect on the protective ability of the metallizing. The old steel specimens did lose less mass than the new steel specimens on average by the end of the test, but the difference is minor and their behaviour was otherwise very similar.

Figure 4.24 shows the XRD output for the zinc metallizing prior to pickling.

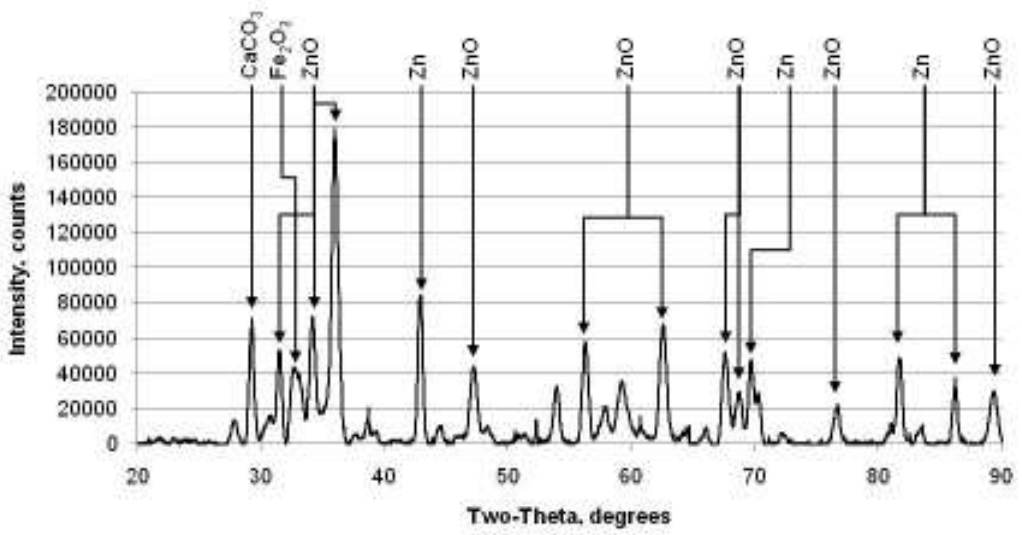

Figure 4.24: XRD output for zinc metallizing

The compounds found on the zinc metallizing were predominantly zinc (Zn) and zinc oxide (ZnO). Also found was an amount of calcium carbonate ($CaCO_3$) and hematite (Fe_2O_3). The former is a component of the salt solution, so it is not surprising to see it collected on the coating surface; as for the iron oxide, since no complete penetration of the coating was visible, it is assumed that it washed onto the surface from one of the uncoated specimens during the test.

Figure 4.25 shows the XRD output for the Al-Zn-In metallized coating after the completion of the test but prior to pickling.

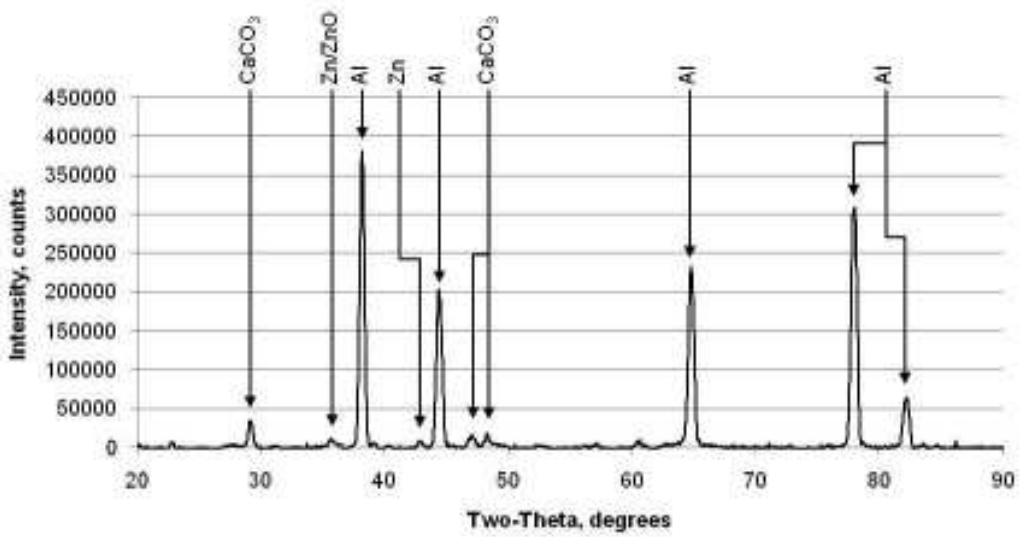

Figure 4.25: XRD output for Al-Zn-In metallizing

Most prominent in the results is the presence of aluminum (Al), although some zinc and zinc oxide are present as well. As with the zinc metallized coating, this coating shows the presence of calcium carbonate ($CaCO_3$).

Taped Specimens

The overall behaviour of the taped specimens for the duration of the corrosion test is shown in Figure 4.26.

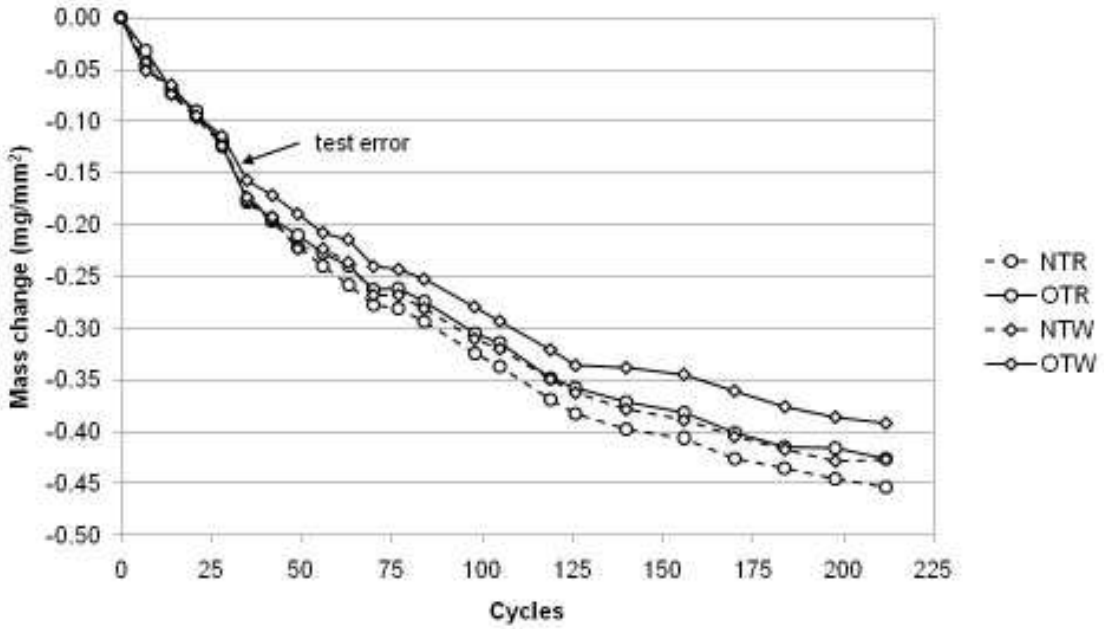

Figure 4.26: Corrosion test mass change results - taped specimens

The taped specimens began with a steep loss in overall mass that gradually began to level off. As with the metallized specimens, the taped specimens all behaved similarly, regardless of the steel composition, degree of sandblasting, and surface roughness of the specimens.

Figure 4.27 shows two examples of taped specimens prior to the start of the test.

Figure 4.27: NTR1 (left) and OTR1 (right), prior to start of test

Figure 4.28 shows the same specimens after they had been removed from the corrosion chamber after 212 cycles.

Figure 4.28: NTR1 (left) and OTR1 (right), after end of test

As can be seen from Figure 4.28, little appears to have happened to most of the taped specimens during the corrosion test. There are some exceptions: on specimen NTR1, a blister had formed in the right-hand side of the tape. Figure 4.29 was taken after the specimen had been sectioned and the PVC layer had been cut and removed from the zinc tape with a scalpel.

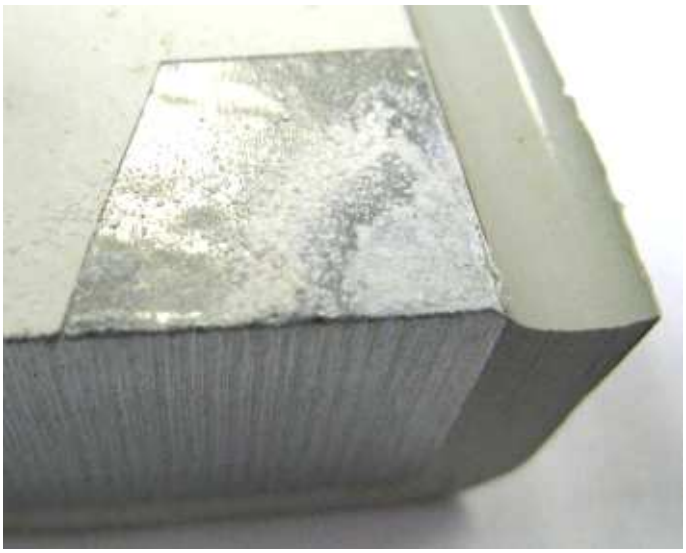

Figure 4.29: Specimen NTR1, after sectioning and PVC layer removal

As can be seen from this figure, a significant amount of powdery white corrosion product, thought to be zinc oxide (ZnO), had collected under the PVC coating.

The source of the mass loss is difficult to determine. As mentioned in Section 3, the tape is a layer of pure zinc covered with a layer of PVC. For an oxidation reaction to occur, the salt solution has to penetrate the layer; for mass loss to occur, the reaction products have to escape the PVC layer again. However, most of the tape specimens do not appear to have experience significant amounts of corrosion. Figure 4.30 shows another taped new steel specimen with its PVC layer removed; very little corrosion product is visible.

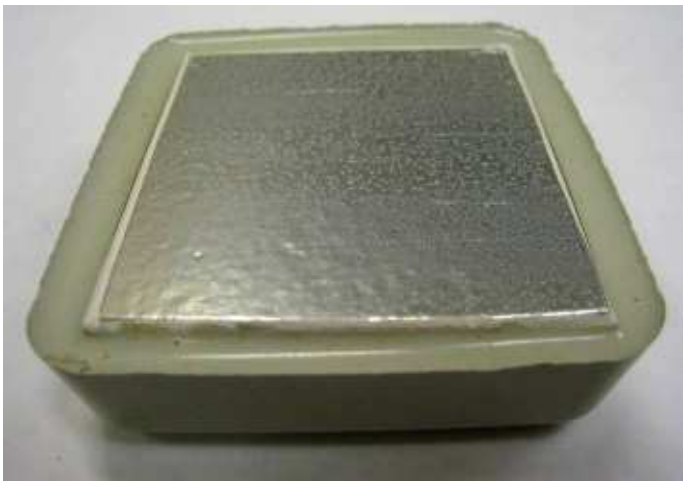

Figure 4.30: Specimen NTR4 with PVC cover removed

The zinc layer in the specimen in Figure 4.30 is still shiny; when the zinc layer corrodes, it becomes darker and duller. It is possible that some part of the mass loss is due to the degradation of the PVC topcoat of the tape.

Figure 4.31 is a photomicrograph of a section taken from a tape-coated new steel specimen.

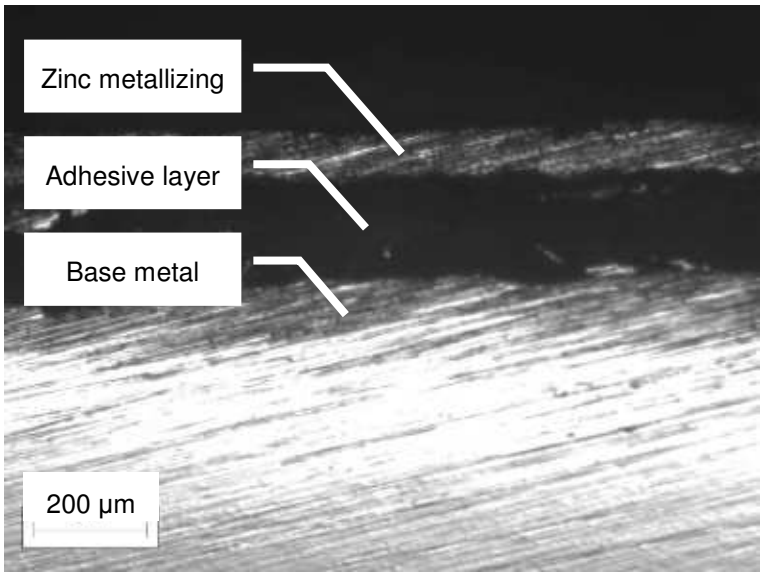

Figure 4.31: Photomicrograph of NTR5 section

The PVC coating is not visible because it had peeled back during the sanding process. No locations were found where the corrosion had penetrated the zinc layer.

Figure 4.32 is a photomicrograph of a taped new steel specimen which was subject to salt solution penetration; the corrosion product forms little bumps on the zinc which are visible through the PVC layer.

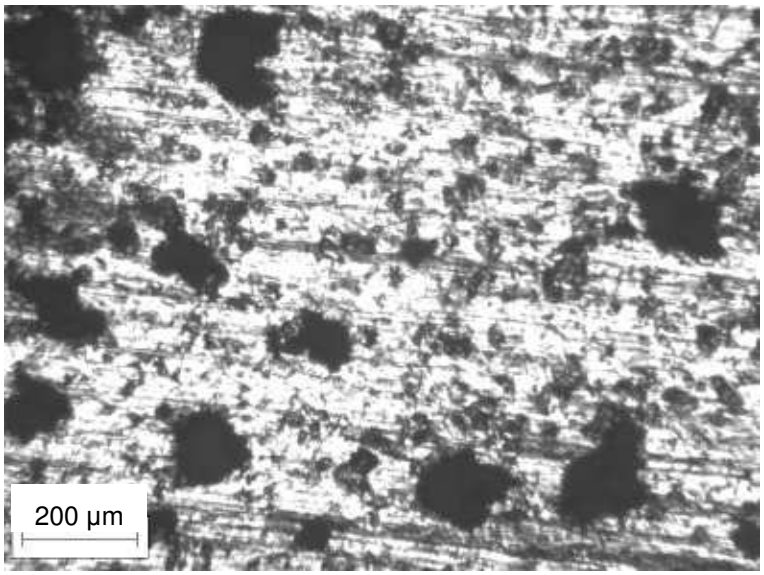

Figure 4.32: Photomicrograph of NTR5 surface

Figure 4.33 shows the XRD results for a taped specimen after the PVC layer was removed with a scalpel. It was possible to visually ascertain that the PVC coating had protected the zinc layer since the zinc was still bright and little corrosion product was visible.

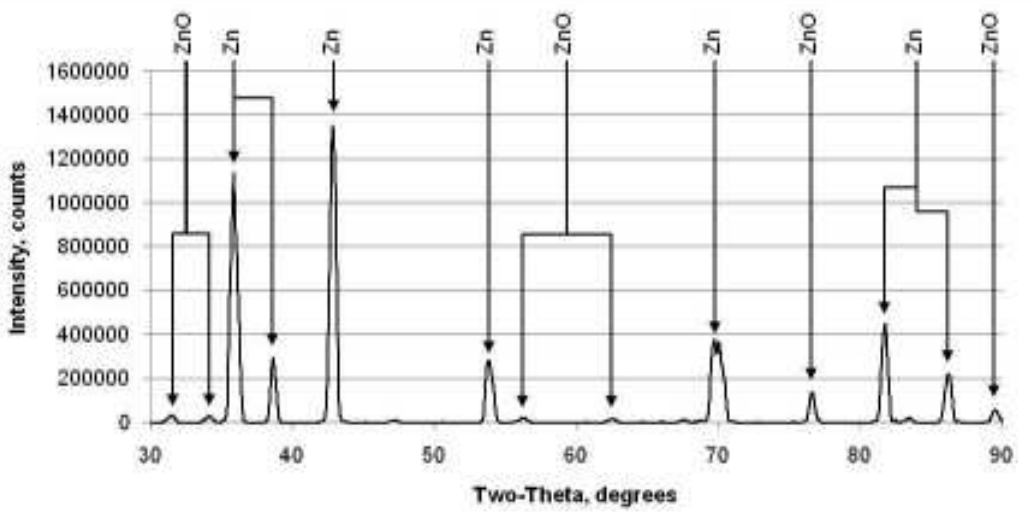

Figure 4.33: XRD results for zinc tape with PVC layer removed

The only compounds found on the zinc tape specimen were zinc and, to a much smaller degree, zinc oxide. This is consistent with what was expected for this specimen.

4.2.4 Supplementary Tests

Calibration Test

Additional uncoated specimens were fabricated and placed in the corrosion tester to measure more precisely the section loss to corrosion that occurs over time. The reason for this was to estimate how a cycle or series of cycles in the corrosion tester related to a given period of corrosion in the real world. A total of twelve plates of the same type of steel as the "new steel" were introduced into the corrosion tester, with three being removed, pickled and weighed every two weeks. These specimens were relatively thin (approximately 3.6 mm thick on average) and had a large surface area. Figure 4.34 is a chart with the specimen corrosion penetration plotted alongside the corrosion penetration curve (± 1 standard deviation) of Equation 2.3.

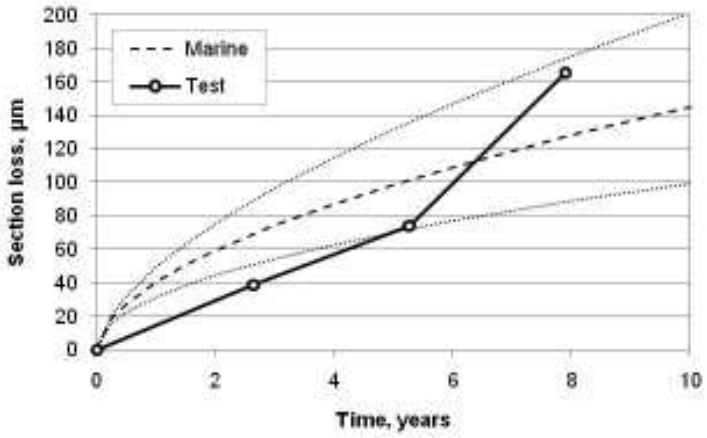

Figure 4.34: Steel plate section loss comparison

Using the method of least squares to match the section loss of the specimens with the corrosion penetration curve for weathering steel in marine environment (because of the additional environmental factors required for the other corrosion rates, only marine corrosion rate was used to calculate the equivalent test duration), it can be estimated that a single cycle is equivalent to approximately 70 days; as such, the uncoated specimens were tested for the equivalent of 15 years, and the coated specimens were tested for the equivalent of 40 years. However, it must also be noted that the section loss on the plate specimens shown in Figure 4.34 was considerably smaller than that found on the uncoated specimens exposed for a similar period. Using the average thickness loss in Table 4.7 and the corrosion equation with the values for the marine corrosion rate, it

would appear that the specimens were in the corrosion machine for the equivalent of 120 years. This disparity is inexplicable.

Epoxy Test

Four epoxy blanks were also introduced into the corrosion machine in order to test their behaviour under the test conditions. The four blanks were cast in the same forms but had varying masses, so that their surface area was largely the same but their volumes and masses varied substantially. Table 4.8 contains the masses of the blanks at the start of the test.

Table 4.8: Blank masses

Blank #	Mass (g)
1	121.53
2	92.23
3	83.75
4	47.95

The results of the test are shown in Figure 4.35 and Figure 4.36.

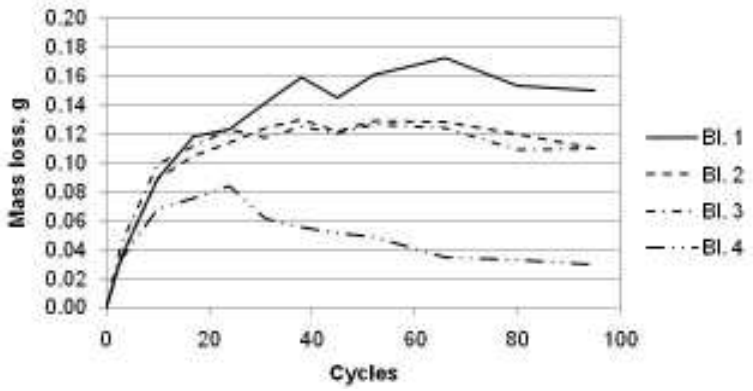

Figure 4.35: Mass loss over time for blank specimens

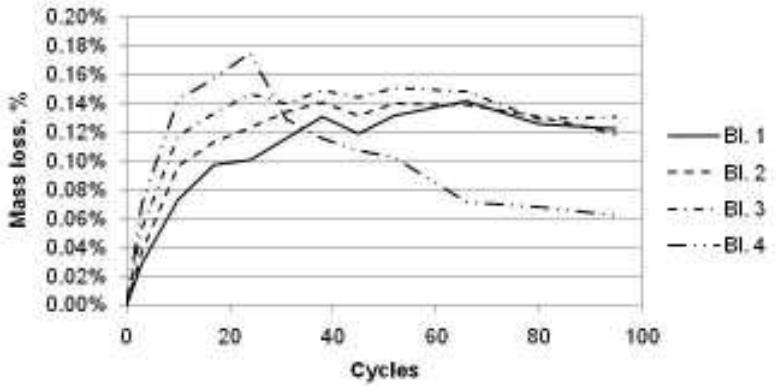

Figure 4.36: Percentage mass loss over time for blank specimens

Over the course of the first 20 cycles the epoxy blanks increased in mass; after this, the rate of mass gain either slowed or, in the case of the smallest, thinnest specimen, reversed into mass loss. In any case, this test clearly indicates that the mass loss in the taped and metallized specimens is not a result of mass loss on the part of the epoxy.

CHAPTER 5: STRUCTURAL ANALYSIS OF CORRODING BRIDGE GIRDERS

5.1 Introduction

In order to assess the reliability of the corroding highway structures, it was necessary to create analytical models that take into account the following four factors:

1. the capacity of the structure;
2. the loading the structure must sustain;
3. the effects of progressive corrosion on the structural capacity; and
4. the statistical variations associated with factors 1 – 3.

Programs that consider these structural and statistical issues were written in Microsoft Excel, with Visual Basic for Applications (VBA) employed where appropriate. The following two program types were created:

1. Deterministic analysis programs to perform deterministic structural design checks of the structures. The output, in each case, is a table of deterministic design ratios (strength/resistance) for various limit states and locations along the bridge span.
2. Probabilistic or reliability analysis programs to determine the probability of failure associated with the various limit states and locations along the bridge span versus the number of years in service.

Variants of these programs were created for analyzing the following structure types:

1. simply supported box girder bridges;
2. simply supported I-girder bridges; and
3. two-span continuous box girder bridges.

5.2 Deterministic Analysis Programs

5.2.1 General

All of the structural analysis programs written for the current study follow the procedures and principles of the [CAN/CSA-S6-06] Canadian Highway Bridge Design Code. Specifically, they include the ultimate limit state calculations outlined in Section 10 of

this code; likewise, the loading, load factors, and load distribution are taken from Sections 3 and 5 of [CAN/CSA-S6-06].

Limit State Equations

A total of five failure modes are considered at several points along the span; each failure mode or "limit state" is identified and quantified by [CAN/CSA-S6-06], as follows:

1. shear ($V_f / V_r \le 1.0$);
2. moment ($M_f / M_r \le 1.0$);
3. shear + moment ($0.727 M_f / M_r + 0.455 V_f / V_r < 1.0$);
4. bearing ($B_f / B_r \le 1.0$); and
5. web breathing or fatigue effects in the web ($h/w \le 3150/\sqrt{F_{yg}}$);

where V, M, and B are shear, moment, and bearing, respectively. The subscript f denotes the factored load effect and the subscript r denotes the resistance of the girder. Also, h is the web height, w is the web thickness, and F_{yg} is the yield stress of the girder.

Failure modes 1 to 4 are considered to be ultimate limit states, meaning that their violation would result in structural failure. Mode 5 may be considered as a serviceability limit state, since its violation is not expected to result in immediate structural failure.

For the calculation of shear resistance, the following formula is applied:

$$V_r = \phi_s A_w F_s \text{ where } F_s = F_{cr} + F_t \text{ and:} \tag{5.1}$$

when $h/w \le 502\sqrt{k_v / F_{yg}}$, $F_{cr} = 0.577 F_{yg}$ and $F_t = 0$

when $502\sqrt{k_v / F_{yg}} < h/w \le 621\sqrt{k_v / F_{yg}}$, $F_{cr} = \dfrac{290\sqrt{k_v / F_{yg}}}{h/w}$ and

$$F_t = \left[0.5 F_{yg} - 0.866 F_{cr}\right]\left[1 + (a/h)^2\right]^{-1/2}$$

when $h/w > 621\sqrt{k_v / F_{yg}}$, $F_{cr} = \dfrac{180000 k_v}{(h/w)^2}$ and

$$F_t = \left[0.5F_{yg} - 0.866F_{cr}\right]\left[1 + (a/h)^2\right]^{-1/2}$$

where $k_v = 4 + \dfrac{5.34}{(a/h)^2}$ when $a/h < 1$

and $k_v = 5.34 + \dfrac{4}{(a/h)^2}$ when $a/h \geq 1$

In Equation 5.1, ϕ_s is the resistance factor for steel, A_w is the area of the web, and F_s is the shear strength at the ultimate limit state; a is the horizontal spacing between vertical web stiffeners, F_t is tension field component of post-buckling stress, F_{cr} is the shear buckling stress, and k_v is the shear buckling coefficient. For the calculation of positive moment resistance of the composite box girder bridge, the girder is assumed to behave plastically. Figure 5.1 to Figure 5.3 show the assumed distribution of stresses across the girder depth for various neutral axis locations.

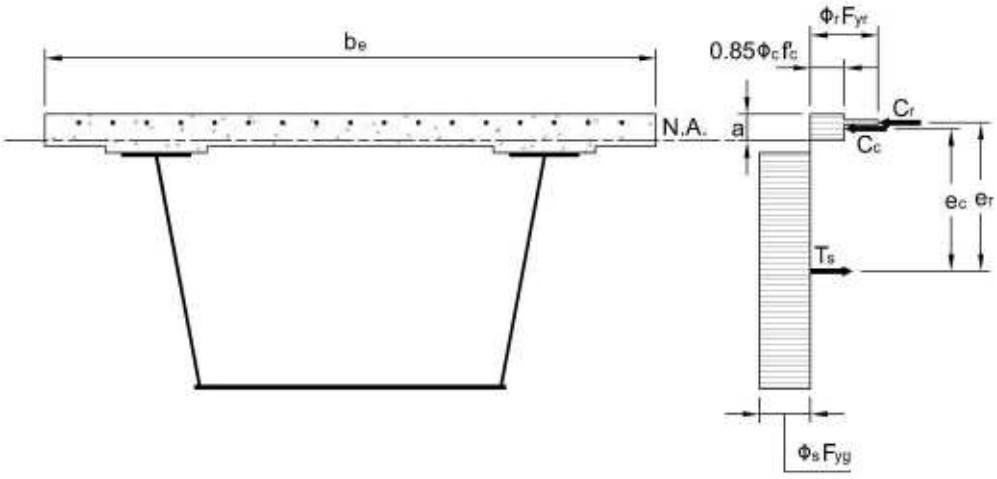

Figure 5.1: Plastic section analysis - neutral axis in the slab

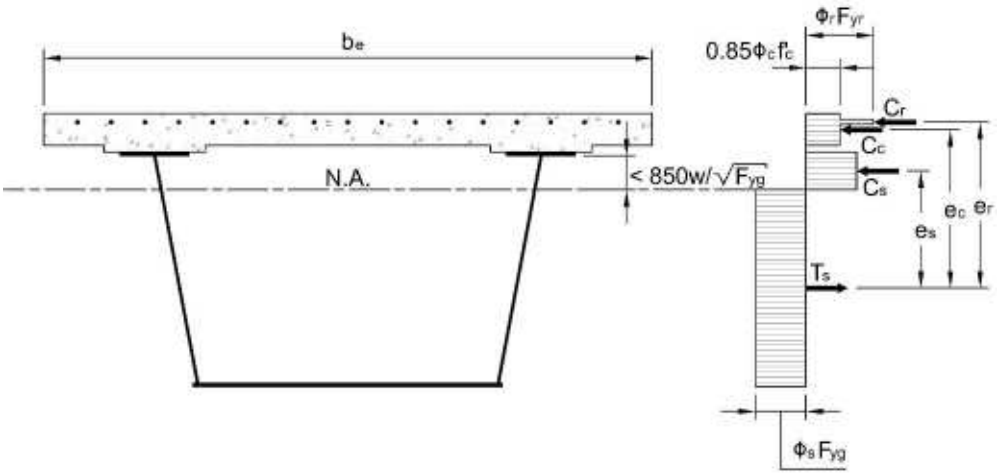

Figure 5.2: Plastic section analysis - neutral axis in upper web

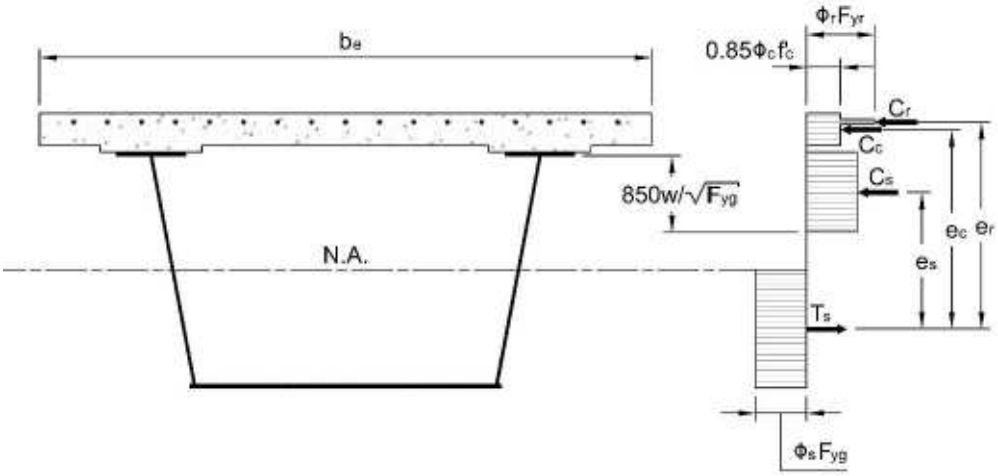

Figure 5.3: Plastic section analysis - neutral axis in lower web

In Figure 5.1 to Figure 5.3, the tension in the lower part of the steel girder (T_s) in each case is counterbalanced by the compression in the top part of the steel girder (C_s), the concrete slab (C_c), and the reinforcement (C_r). The moment resistance is a function of these forces and the eccentricities between them (e_s, e_c, and e_r). f'_c is the assumed nominal concrete compressive strength, f_{yr} is the assumed nominal yield strength of the rebar, and F_{yg} is the assumed nominal yield strength of the weathering steel girder.

When the neutral axis is in the slab (Figure 5.1), the moment resistance is:

$$M_r = C_c e_c + C_r e_r \tag{5.2}$$

When the neutral axis is in the web (Figure 5.2), but less than $850w/\sqrt{F_{yg}}$ below the top of the web, the moment resistance is:

$$M_r = C_c e_c + C_r e_r + C_s e_s \tag{5.3}$$

When the neutral axis is more than $850w/\sqrt{F_{yg}}$ below the top of the web (Figure 5.3), the moment resistance is:

$$M_r = C_c e_c + C_r e_r + C_s e_s \tag{5.4}$$

Equations 5.3 and 5.4 differ in that, when the neutral axis becomes further than $850w/\sqrt{F_{yg}}$ from the bottom of the top flange, part of the web in compression ceases to contribute in compression (see Figure 5.3). For the calculation of bearing resistance at the abutments, the following formula is applied:

$$B_r = 1.50\phi_s A_s F_y + MIN\begin{Bmatrix} \phi_{be} w(N+4t)F_{yg}, \\ 0.60\phi_{be} w^2 \sqrt{F_{yg} E_s} \end{Bmatrix} \tag{5.5}$$

Equation 5.5 is in two parts, of which the first calculates the bearing resistance of the stiffeners and the second calculates the bearing resistance of the web. However, the bearing resistance of the stiffeners is taken as zero if $b/t > 200/\sqrt{F_{yg}}$, where b and t are the width and thickness of the stiffener, respectively. Figure 5.4 is a depiction of the bearing arrangement for the box and I-girder bridges.

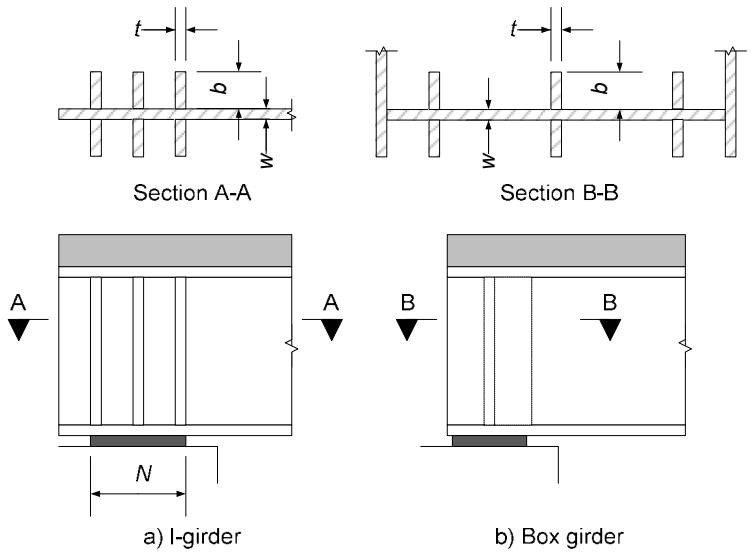

Figure 5.4: Bearing stiffener arrangement for box and I-girder

In Equations 5.1 – 5.5, the ϕ factors are material resistance factors for the concrete (ϕ_c), rebar (ϕ_r), and steel (ϕ_s). The factor ϕ_{be} is a special resistance factor for beam end web bearing. The values for the factors are contained in Table 5.2.

Table 5.1: Resistance factors [CAN/CSA-S6-06]

Element	Factor
Structural steel, ϕ_s	0.95
Reinforcing steel, ϕ_r	0.90
Concrete, ϕ_c	0.75
Bearing (at abutment), ϕ_{be}	0.75

The resistance factors are applied at the ultimate limit state to account for variability of material properties and dimensions, as well as quality of work, type of failure, and the uncertainties associated with these parameters [CAN/CSA-S6-06]. These factors are only applied in the deterministic programs; in the probabilistic programs, they are all set to 1.0 and statistical "bias factors" are used to modify the resistances.

Loading Analysis

Only dead and live (traffic) loads are considered in the current analysis, since these typically dominate the design of short- and medium-span bridges. Two types of dead load are taken into account. The superimposed dead load refers to the sidewalk and wearing surface, while the dead load itself refers to the slab and steel girder self weight.

The slab, wearing surface, sidewalks and barriers were treated as uniformly distributed loads (UDL); their gravity loads per metre were summed and divided by the number of girders. The self-weight of the girder was likewise treated as a UDL.

The unit weights assumed to calculate the dead loads are given in Table 5.2.

Table 5.2: Unit weights of structural components [CAN/CSA-S6-06]

Component	Weight
Bituminous wearing surface	23.5 kN/m^3
Concrete	24.0 kN/m^3
Steel	77.0 kN/m^3

As prescribed in [CAN/CSA-S6-06], the live load (LL) is taken as the greater of a five-axle truck load and a truck-plus-lane load, as shown in Figure 5.5 and Figure 5.6.

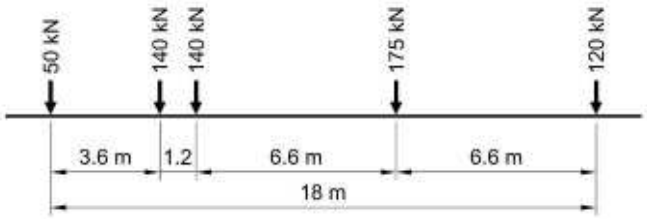

Figure 5.5: CL-625 ONT axle load

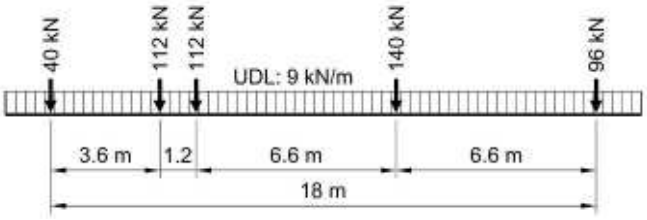

Figure 5.6: CL-625 ONT lane load

Factors

Table 5.3 shows the factors applied for ultimate limit state verification under the dead plus live load combination (load combination ULS1 [CAN/CSA-S6-06]). These factors assume that the dead load will always be detrimental. In the probabilistic programs, these factors are set to a value of 1.0 and their effect is accounted for statistically.

Table 5.3: Load factors [CAN/CSA-S6-06]

Load type	Factor
Live load (traffic)	1.70
Superimposed dead load (wearing surface)	1.50
Cast-in-place dead load (concrete deck)	1.20
Manufactured dead load (steel girder)	1.10

Along with the live load factor, the live (traffic) load effects are multiplied by an additional factor, which takes into account the dynamic component of the live load, called the dynamic load allowance (DLA). The value of the DLA varies with the number of axles of the CL-W truck used in the analysis. Axle numbers are as per the drawing in Figure 5.5. The DLA values are contained in Table 5.4.

Table 5.4: Dynamic load allowances [CAN/CSA-S6-06]

Axle(s) used	DLA
Only one axle	0.40
Any two axles, or axles 1 to 3	0.30
Any three axles, except for axles 1 to 3, or more than three axles	0.25

In the statistical programs, the axle load (but not the lane load) is multiplied by (1 + DLA). In the probabilistic programs, the DLA is treated as a statistical variable.

In certain cases, there is also a modification factor for multi-lane loading (by which the live load effects may be multiplied), to take into account the likelihood of having more than one lane loaded at any given time. These values are contained in Table 5.5.

Table 5.5: Modification factor for multi-lane loading [CAN/CSA-S6-06]

Number of loaded design lanes	Factor
1	1.00
2	0.90
3	0.80
4	0.70

For multi-girder bridges, there is also a live load amplification factor (LLAF) that may be applied to the live load to account for the transverse sharing of these loads between the girders. The LLAF for the moment on a single-span bridge is:

$$F_m = \frac{SN}{F\left[\frac{\mu C_f}{100}\right]} \geq 1.05 \tag{5.6}$$

Where F_m is the amplification factor to account for the transverse variation in the maximum longitudinal moment intensity, as compared to the average longitudinal moment intensity, S is the centre-to-centre girder spacing, and N is the number of girders. The values for F, the width dimension that characterizes the load distribution for the bridge, and C_f, the correction factor used to adjust the F value for longitudinal moment and longitudinal vertical shear, are contained in Table 5.6.

Table 5.6: F and C_f values for moment [CAN/CSA-S6-06]

	Box girder		I girder	
Lanes	F	C_f	F	C_f
2	$8.5 - 0.3\beta$	$16 - 2\beta$	$6.80 - (3/L)$* $7.20 - (14/L)$**	$10 - (25/L)$
3	$11.5 - 0.5\beta$	$16 - 2\beta$	$8.70 - (4/L)$* $9.60 - (21/L)$**	$10 - (25/L)$
4	$14.5 - 0.7\beta$	$16 - 2\beta$	$10.00 - (5/L)$* $11.20 - (22/L)$**	$10 - (25/L)$

* For external girder ** For internal girder

The values in Table 5.6 assume a bridge span of at least 10 m. The lane width modification factor, μ, is calculated with the following equation:

$$\mu = \frac{W_e - 3.3}{0.6} \leq 1.0 \tag{5.7}$$

where W_e is the width of the design lane. For the box girders, the β parameter is taken as:

$$\beta = \pi \left[\frac{B}{L}\right]\left[\frac{D_x}{D_{xy}}\right]^{0.5} \tag{5.8}$$

where B and L are the bridge width and length respectively; D_x is the total bending stiffness (equal to the modulus of elasticity times the moment of inertia) of the bridge cross-section divided by the width of the bridge, and D_{xy} is the total torsional stiffness (equal to the shear modulus times the torsional inertia) of the bridge cross-section divided by the width of the bridge. The LLAF for the shear is:

$$F_v = \frac{SN}{F} \tag{5.9}$$

where the S and N values are the same as above. The F value is tabulated in [CAN/CSA-S6-06]; Table 5.7 summarizes the relevant values for box and I-girders.

Table 5.7: *F* values for shear [CAN/CSA-S6-06]

Lanes	Box girder	I-girder
2	7.20	6.10
3	9.60	8.20
4	11.20	9.50

The procedure described above for the application of the LLAF is a simplified, and conservative, approach; other, more laborious means of calculating this factor exist, such as by finite element modelling. For its valid application, certain requirements are laid out in [CAN/CSA-S6-06]. These requirements are listed in Table 5.8.

Table 5.8: LLAF requirements

Box girder (multispine) bridges	I-girder bridges
• bridge has constant width • support conditions are closely equivalent to line support at the ends of the bridge • overhang is not more than 1.80 m and does not exceed the spacing of the two outermost adjacent webs • at least two longitudinal girders of approximately equal flexural rigidity and spacing • each spine has only two webs • number of lanes is larger than or equal to the number of spines • bridge's length is greater that its width	• bridge has constant width • support conditions are closely equivalent to line support at the ends of the bridge • overhang is not more than 1.80 m and does not exceed 60% of the spacing between the girders • at least three girders of approximately equal flexural rigidity and spacing

5.2.2 Simply Supported Structures

In the deterministic and probabilistic analysis programs for simply supported structures, the span of the structure is divided into ten sections, with the relevant limit states being calculated at the beginning and end of each section (eleven locations along the span).

Also, up to seven different sections can be specified for the span; each of these sections can have its own length, girder geometry, corrosion rate, and corrosion scenario.

To calculate the live (truck) loading, the axle loads are moved along the length of the bridge (at the specified axle spacing) at 1 m increments, and the maximum shear and moment resultants at each of the eleven locations along the span are kept for the analysis procedure. Both dead and live load effects are calculated with closed form equations in the VBA program as a preliminary stage to the bridge analysis.

5.2.3 Two-Span Continuous Structures

The program for analyzing two-span continuous bridges is similar to the single-span program in many respects; however, the two-span program is necessarily more complex. Because a two-span continuous structure is statically indeterminate, it was necessary to build a finite element model to perform the analysis. Due to the regularity of the problem and in order to more easily integrate the structural analysis into a single program with the resistance verification, a finite element code was written in VBA for this purpose.

The finite element model is composed of beam elements, which have four degrees of freedom each, representing the vertical displacement, q_1 and q_3, and the rotation, q_2 and q_4, of the two nodes. A typical element is depicted in Figure 5.7.

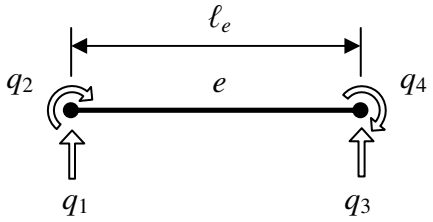

Figure 5.7: Free body diagram of beam element

The two-span continuous model is composed of two spans of ten elements each, for a total of twenty elements and twenty-one nodes. As such, the girder of each span can be broken up into segments with different cross-sectional geometries. It is not necessary that the two spans are identical. The element stiffness matrix is as follows:

$$k^e = \frac{EI}{\ell_e^3}\begin{bmatrix} 12 & 6\ell_e & -12 & 6\ell_e \\ 6\ell_e & 4\ell_e^2 & -6\ell_e & 2\ell_e^2 \\ -12 & -6\ell_e & 12 & -6\ell_e \\ 6\ell_e & 2\ell_e^2 & -6\ell_e & 4\ell_e^2 \end{bmatrix} \tag{5.10}$$

As with any finite element program, the individual element stiffness matrices are combined into a global stiffness matrix and joined with the global force matrix to solve for displacements and reactions.

Loading Analysis

The loading cases for a two-span continuous structure are the same as for a simply supported structure. The live load due to the CL-625 ONT truck is again assumed; and again, both the axle and lane variants of this loading are considered. However, for the two-span continuous bridge the truck is moved across only eleven locations on each span, and the centre of gravity of the truck is used to locate it.

Limit State Equations

Since the negative moment puts a significant portion of the web into compression, the structural resistance to negative moment is calculated using the elastic section modulus. Furthermore, different sections are considered for different stages of loading: the load of the girder plus the slab is compared against the resistance of the girder alone, while the load of the girder, slab, wearing surface, and rails is compared against the resistance of the composite section before creep, and the live load is compared against the resistance of the composite section after creep. The purpose of this is to simulate the loads introduced into the system at each stage of the construction sequence.

Three different limit states are considered with respect to moment: the stresses in the reinforcement (1) and the top fibre of the top flange (2) must not exceed the yield stress, and the bottom flange (3), which is in compression, must not buckle. Therefore, three equations are required to verify the moment limit state:

For the bottom flange: $M_{fd}/S + \left(M_{fsd} + M_{fl}\right)/S' \leq \phi_s F_{cr}$ (5.11)

where the elastic section moduli are calculated with respect to the bottom fibre, for the steel girder alone and for the composite section respectively. Figure 5.8 shows how the stresses are calculated and the section is checked for overload.

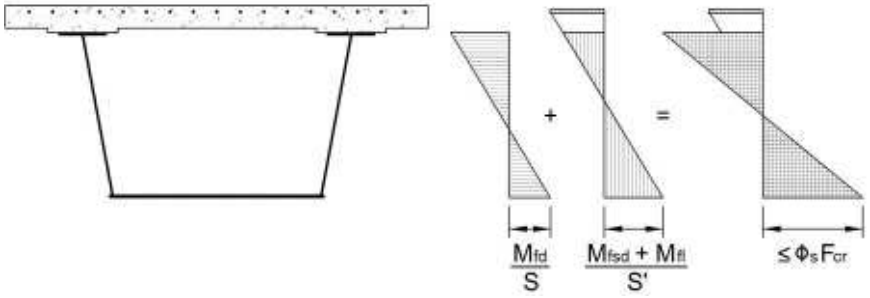

Figure 5.8: Elastic section analysis – negative moment [CAN/CSA-S6-06]

M_{fd} is the factored bending moment due to dead load (the self-weight of the girder and slab), M_{fsd} is the factored bending moment due to superimposed dead load (sidewalks, barriers, and wearing surface), and M_{fl} is the factored bending moment due to the live load (traffic). S and S' are the elastic section moduli of the steel girder alone and the girder plus reinforcement respectively. F_{cr} is the buckling stress of the compression flange.

The value for F_{cr} is found as follows [CAN/CSA-S6-06]:

1. when $b/t \le 510/\sqrt{F_{yg}}$, $F_{cr} = \phi_s F_{yg}$

2. when $510/\sqrt{F_{yg}} < b/t \le 1100/\sqrt{F_{yg}}$, $F_{cr} = 0.592 F_{yg}\left[1 + 0.687 \sin\frac{\pi C}{2}\right]$, where

   $$C = \frac{1100 - (b/t)\sqrt{F_{yg}}}{590}$$

3. when $b/t > 1100/\sqrt{F_{yg}}$, $F_{cr} = \frac{7.24 \times 10^5}{(b/t)^2}$

where F_{yg} is the yield strength of the girder, and b and t are the thickness and width of the bottom flange respectively.

For the top flange: $M_{fd}/S + (M_{fsd} + M_{fl})/S' \le \phi_s F_{yg}$ (5.12)

where the elastic section moduli are calculated with respect to the top fibre of the steel section, for the steel girder alone and for the composite section respectively.

For the top layer of reinforcement: $\left(M_{fsd} + M_{fl}\right) \Big/ S' \leq \phi_r F_{yr}$ (5.13)

where the elastic section modulus is calculated with respect to the centroid of the top layer of slab reinforcement for the composite section.

In [CAN/CSA-S6-06] a girder section is defined by its class, which is determined by the width-to-thickness ratios of its component members. Class 1 and 2 sections are capable of achieving the full plastic moment capacity; Class 3 sections only have elastic moment capacity (as such, only the outermost fibre of the girder may undergo yield stress), while Class 4 sections would experience local buckling below this applied moment level [Kulak & Grondin 2006]. Due to the fact that the webs and bottom flanges of the box girder section lose section as time progresses in the program, either one or both may become Class 4 members. [CAN/CSA-S6-06] requires that either the web or the flange be a Class 3 member, but in the context of this research this requirement was thought to be overly restrictive. In order to take into account the additional reduction in the resistance due to member slenderness of the continuous box girder under negative moments, the box girder section is treated as a stiffened plate girder: in the case where $2d_c / w > 1900 \Big/ \sqrt{F_{yg}}$, the negative moment resistance is multiplied by the following factor:

$$1 - \frac{1}{300 + 1200 A_{cf} / A_w} \left[\frac{2d_c}{w} - \frac{1900}{\sqrt{F_{yg}}} \right] \tag{5.14}$$

where d_c is the depth of compression portion of web in flexure, w is the web thickness, A_{cf} is the area of the compression flange, and A_w is the area of the web.

For the calculation of bearing resistance at the midspan, the following formula is applied [CAN/CSA-S6-06], which is similar to Equation 5.5 for end bearing:

$$B_r = 1.50 \phi_s A_s F_{yg} + MIN \begin{Bmatrix} \phi_{bi} w (N + 10t) F_{yg}, \\ 1.45 \phi_{bi} w^2 \sqrt{F_{yg} E_s} \end{Bmatrix} \tag{5.15}$$

The value for ϕ_{bi} is 0.80. Again, the first part of the equation is the contribution of the stiffeners, which is taken as zero if $b/t > 200/\sqrt{F_{yg}}$,

Factors

The load and resistance factors for a two-span continuous structure are the same as for a simply supported structure. For the LLAF, the positive and negative section lengths are calculated according to Figure 5.9.

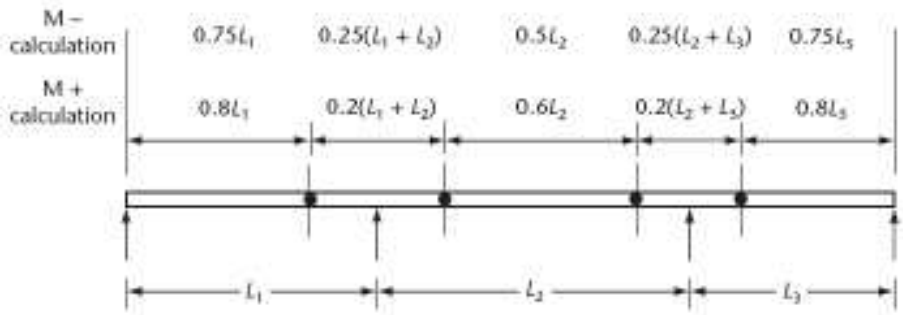

Figure 5.9: Section lengths for multi-span bridge [CAN/CSA-S6-06]

5.3 Probabilistic Analysis Programs

5.3.1 General

The basic methodology employed in developing the probabilistic (reliability) analysis programs can be described as an iterative analysis procedure (Monte Carlo simulation) built around a corrosion rate equation. Corrosion penetration is calculated at a set time interval, and the geometrical and, consequently, structural properties of the bridge are modified accordingly. When the resistance of the section becomes less than the load effect, i.e. when a limit state is "violated", the program records the year, location along the bridge span, and mode of failure.

The corrosion model is intended to simulate general corrosion, so the thickness loss is for the structural plate as a whole. The program was written such that the section loss can be set to occur to the web and flange, together or separately, and on one or both sides of the corroding structural plate. Figure 5.10 shows the locations that corrosion can be set to occur in the probabilistic programs.

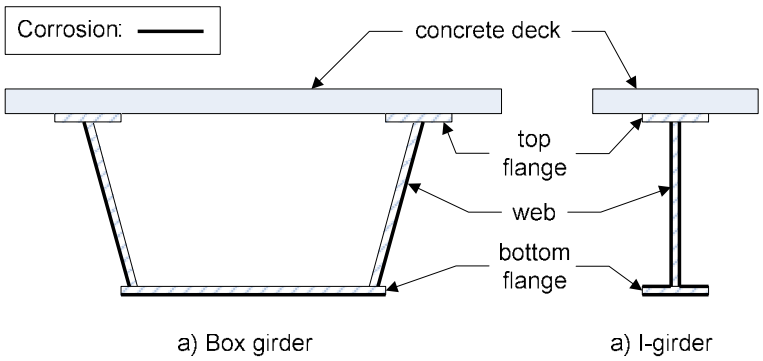

Figure 5.10: Assumed corrosion locations

The steel surfaces with a bold line in Figure 5.10 can be made subject to corrosion in the programs. These surfaces include the exposed surfaces of the web and bottom flange of the box girder, and both sides of the web and bottom flange of the I-girder. Note that, in Chapter 6, a number of analyses are presented for the case of an I-girder with only the top of the bottom flange corroding (rather than both the top and bottom), to simulate a particular corrosion scenario that has been observed in some jurisdictions (including Ontario) [Albrecht & Naeemi 1984, Albrecht et al. 1989].

The program is set to operate for a predetermined number of runs and stores the output of each one. The program employs a basic Monte Carlo simulation algorithm to consider the statistical variability in the various input parameters [Melchers 2002].

5.3.2 Simply Supported Structures

Figure 5.11 shows a flow chart of the operation of the probabilistic (reliability) analysis program for the simply supported case.

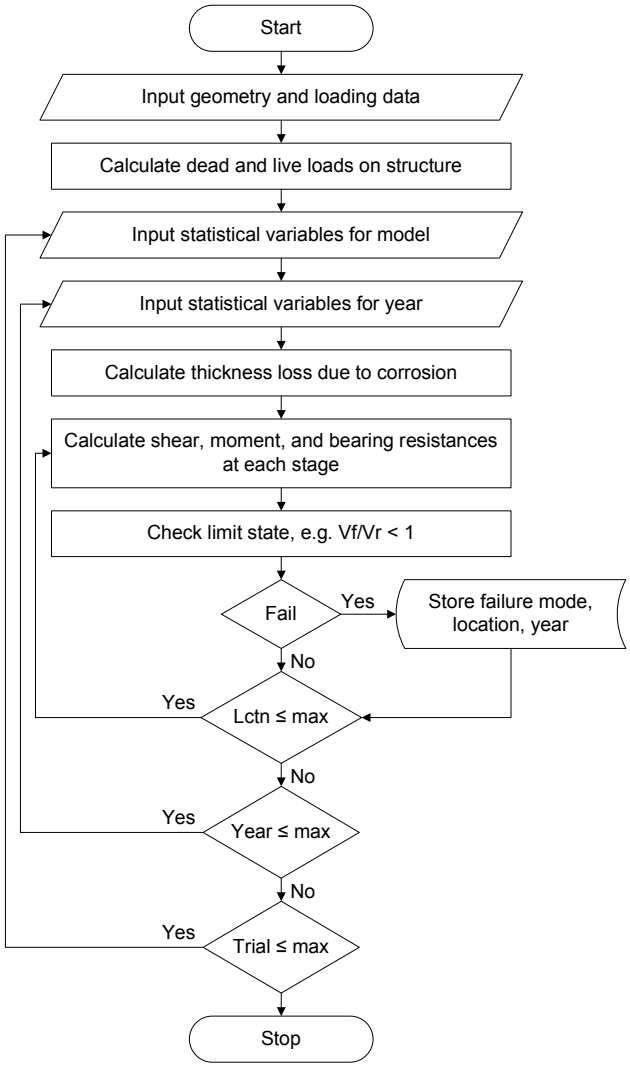

Figure 5.11: Probabilistic program flowchart – simply supported structures

5.3.3 Two-Span Continuous Structures

The two-span continuous program is considerably more complex as the load effects are dependent on the cross-section properties for this indeterminate structural system. Likewise, it has a significantly longer run time. Because the cross section of the girder diminishes with each passing increment of time, causing a redistribution of the loading, it is necessary to analyze the structure anew at each time increment. Figure 5.12 shows the probabilistic program flowchart for the two-span continuous structure analysis.

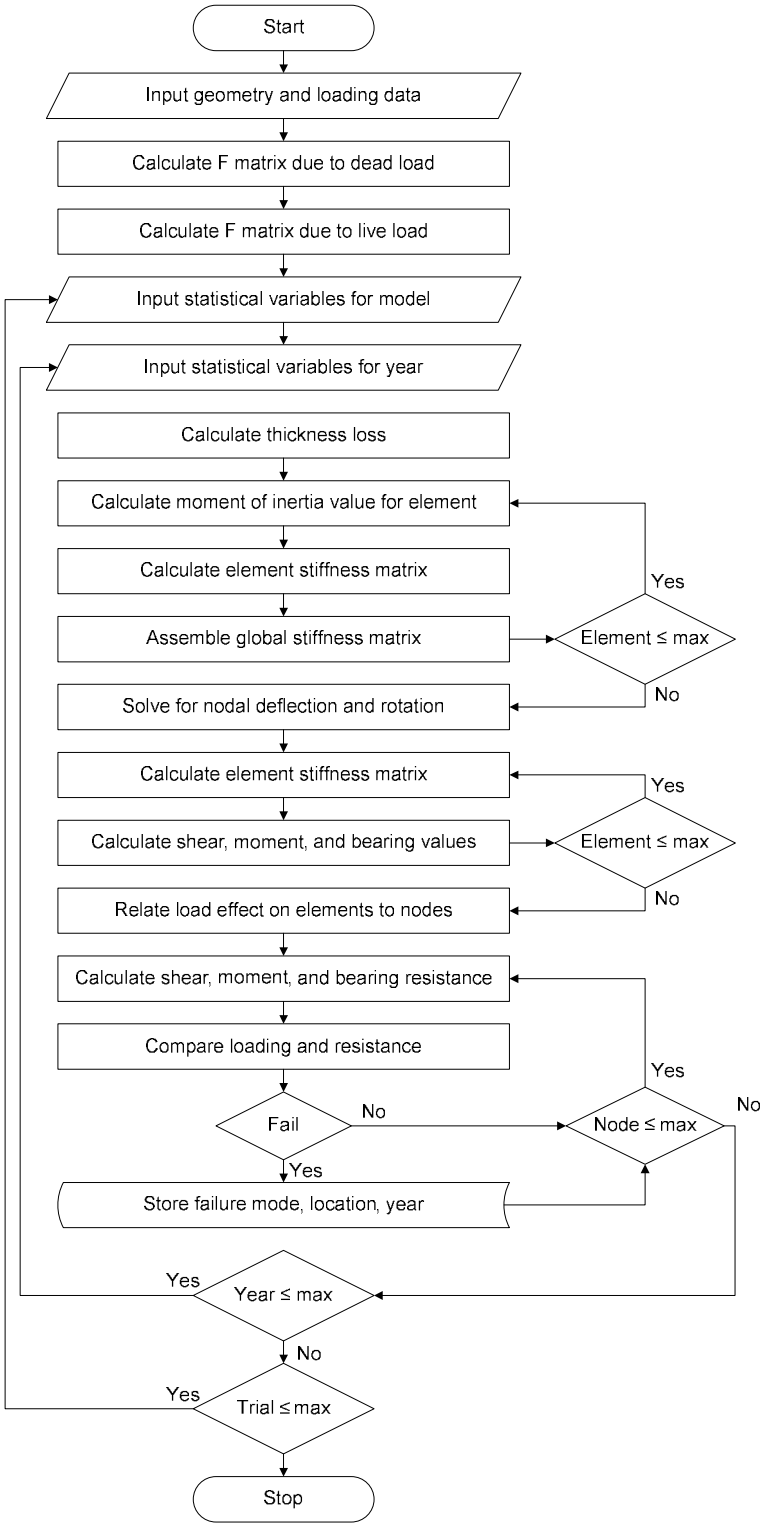

Figure 5.12: Probabilistic program flowchart – two-span continuous structures

5.3.4 Statistical Variables

For the probabilistic analysis, the uncertainties associated with various deterministic model parameters can be considered by multiplying them by appropriate statistical variables or "bias factors". These parameters include the material strengths, calculated resistances, and dead and live loads and effects. The assumed statistical distributions for the corresponding bias factors are listed in Table 5.9.

Table 5.9: Statistical variables and assumed distributions

Input Parameter	Bias Factor		
	Dist. Type	Mean	Std. Dev.
Compressive strength of concrete (f'_c)	Lognormal	0.805	0.150
Yield strength (F_{yg}) of girder	Lognormal	1.101	0.092
Yield strength (F_{yr}) of rebar	Lognormal	1.115	0.100
Moment resistance (M_r) factor	Normal	1.098	0.096
Shear resistance (V_r) factor	Normal	1.178	0.103
Manufactured components DL	Normal	1.030	0.080
Cast-in-place components DL	Normal	1.050	0.100
Superimposed DL	Normal	1.030	0.300
LL analysis factor	Normal	0.930	0.120
Dynamic factor (DLA)	Normal	1.100	0.072
LL shear and moment factor	Gumbel	See Table 5.10	

The source for all these values is [CAN/CSA-S6-00 Calibration], except for the values for f'_c and F_{yr}, which both come from [Cheung & Li 2002]

The values for the mean and standard deviation of the bias factors associated with the concrete compressive strength, f'_c and rebar yield strength, f_{yr} were derived from available test data in [Tabsh & Nowak 1991]. The values used are in the lower end of the range of values found in relevant works; nevertheless, they were thought to be appropriate due to the difficult nature of the work (i.e. bridge vs. normal construction),

the problems associated with placing concrete in certain conditions. The values for the mean and standard deviation of the girder yield stress, F_{yg}, bias factor originate from the work of Kennedy & Baker [1984] on the subject of resistance factors for steel highway bridges. The factors for steel and concrete take into account three sources of error: material, geometrical, and manufacturing/construction.

The factors modifying the dead load of the manufactured and cast-in-place structural elements (the steel girder and concrete slab) were originally from the work done by Nowak and Grouni for calibrating the Ontario Highway Bridge Design Code, which was subsequently verified by other sources for [CAN/CSA-S6-06]. The factor modifying the superimposed dead load, meaning the asphalt wearing surface, is based on field data reported in [CAN/CSA-S6-00 Calibration].

The live load (LL) analysis factor is recommended by the Canadian Highway Bridge Design Code Subcommittee on Analysis; the live load distribution methods of [CAN/CSA-S6-06] are considered to have an intrinsic conservatism, and this factor is required as a result. Two options are given, depending on the level of sophistication of the analysis method.

The dynamic loading factor (DLA) is based on field measurements, performed in Ontario, of a variety of bridges. Trucks requiring special permits were not distinguished since a lower rate of travel is required, thus bringing their contribution in line with those of the regular traffic.

The additional live load (LL) shear and moment factors (see Table 5.10) are also taken from data specific to Ontario, where a survey of trucks was performed in 1995. Only normal traffic, as opposed to traffic operating with a special permit, was considered. Trucks with an average axle weight $\leq$ 4.0 T were screened out, but the total number of trucks (N = 13391) was used as the sample size. Models of a number of these vehicles were driven over bridges of varying lengths in order to determine their shear and moment resultants. These data were combined to generate load-effect histograms.

In [CAN/CSA-S6-00 Calibration], a Gumbel distribution is used to represent the extreme annual statistics for different load effects (i.e. shear, moment) and bridge spans / configurations. A methodology for doing this is presented in this reference, along with

the resulting load effect extreme value distributions for a Class A highway over a one year time period. The methodology can be summarized as follows: Since the actual distribution of load effects is generally not perfectly normal, a representative normal distribution (RND) had to first be established; this was done by focussing on the tail end of the distribution, which was assumed to have properties similar to that of the RND tail. First, a load effect sample was generated, by simulating the passage of a limited number of actual measured trucks (~10,000) over a load effect influence line for a particular bridge span / configuration. Next, two assumptions were made, regarding the resulting sample: first, that the highest value in the sample load effect distribution is an extreme value in the Gumbel distribution for that sample size, and second, that this highest value is three standard deviations above the mean in the Gumbel distribution. If the highest value was significantly larger than the next highest value, the former was used in order to prevent the distribution from being affected by suspect measurements. As such, values for mean and standard deviation of the RND can be derived, and from them the Gumbel distribution for the extreme load effect events corresponding with a certain period of time (for a given traffic volume). By following the same method as that presented in [CAN/CSA-S6-00 Calibration] herein, it was possible to develop bias factor mean and variance values for any time period / highway class.

In [CAN/CSA-S6-06], four different classes of highway (A to D) are defined by their average daily truck traffic (ADTT) rates (see Table 5.10).

Table 5.10: Highway classes [CAN/CSA-S6-06]

Highway class	ADTT (per lane)
A	1000 – 4000
B	250 – 1000
C	50 – 250
D	< 50

Traffic rate variations are only considered for the 40 m simply supported bridge analyzed herein. The bias factor values still change, however, for different spans / configurations, since the influence lines are different. Table 5.11 contains these values. The means and

coefficients of variation in this table reflect the different load effect sample distributions for shear (V) and moment (M). The extreme value distributions presuppose a certain time interval, which is likewise provided in Table 5.11.

Table 5.11: LL shear and moment bias factors (based on 10 year extreme event statistics)

Highway class	Structure type	Span (m)	Interval (yr)	Mean	CoV
A	Simply supported	40	10	1.503 (V) 1.461 (M)	0.033 (V) 0.033 (M)
B	Simply supported	40	10	1.446 (V) 1.405 (M)	0.036 (V) 0.036 (M)
C	Simply supported	40	10	1.386 (V) 1.346 (M)	0.040 (V) 0.040 (M)
D	Simply supported	40	10	1.312 (V) 1.273 (M)	0.045 (V) 0.045 (M)
A	Simply supported	30	10	1.541 (V) 1.542 (M)	0.032 (V) 0.032 (M)
A	Simply supported	35	10	1.543 (V) 1.501 (M)	0.032 (V) 0.033 (M)
C	Two-span continuous	40	8	1.097 (V) 1.290 (M)	0.040 (V) 0.042 (M)

Along with the statistical variables listed in Table 5.9, two additional parameters are statistically varied in the reliability program, namely the *A* and *B* factors of the corrosion penetration equation (Equation 2.3). The means and standard deviations of these factors for the rural, marine, and urban environments are given in Table 5.12.

Kayser [1988] calculated numerical values for the *A* and *B* variables using experimentally obtained corrosion data for rural, industrial, and marine environments compiled in [Albrecht & Naeemi 1984]. These results were assembled in order to come up with values for each corrosion rate, as well as their statistical distributions.

Table 5.12: Corrosion rate parameters

Environment	Variable	Mean	CoV
Rural	*A*	33.3	0.34
	B	0.498	0.09
Marine	*A*	40.2	0.22
	B	0.557	0.10
Urban	*A*	50.7	0.30
	B	0.567	0.37

The above data are based upon corrosion of weathering steel specimens in the United States, the United Kingdom, and Germany. Noteworthy is the relatively high coefficient of variation of the urban corrosion rate's *B* variable, because as the power variable, it introduces a high degree of variability into the corrosion penetration results. A lognormal distribution is assumed for each of these statistical variables.

5.3.5 Statistical Programming

Monte Carlo Simulation

Monte Carlo simulation (MCS) enables the statistical analysis of a complex structural system by repeating the loading and resistance calculations until a statistically significant number of "trials" has been collected. Rather than solving a single, highly complex equation, which would take into account the interaction of a number of statistical variables, Monte Carlo simulation enables the calculation to be performed numerous times with randomly selected values (generated anew each time) for the various statistical variables. The probability of failure is then calculated from the following equation:

$$p_f = \frac{n\left(G(\bar{z}) \le 0\right)}{N_t} \qquad 5.15$$

where N_t is the total number of trials, and $n\left(G(\bar{z}) \le 0\right)$ is the total number of trials for which the limit states were violated (ref. Equations 2.8 to 2.10).

Random Number Generation

Random numbers (between 0 and 1) are generated herein in Microsoft Excel. These numbers, which are uniformly distributed, must be transformed into corresponding trial values for each statistical variable using the specified probability distribution. The manner in which this is accomplished is shown in Figure 5.13. In this figure the probability density function (PDF) of the uniform distribution is shown in quadrant III. The corresponding uniform cumulative density function (CDF) is shown in quadrant II. In quadrant I is the CDF that is specified for the statistical variable, and in quadrant IV is the resulting PDF of the variable [Ang & Tang, 1984].

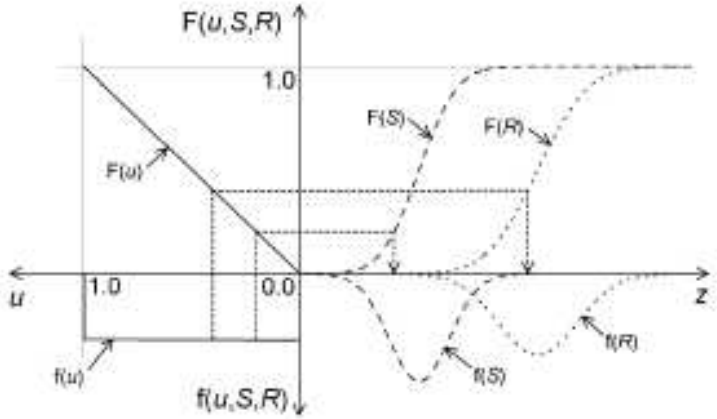

Figure 5.13: Monte Carlo Simulation – relation between *u* and *z* [Walbridge 2005]

In Figure 5.13, two random numbers, u_i, have been generated for two statistical variables, z_i, one for the load (or solicitation, *S*) and the other for the resistance (*R*). In order to transform the two random numbers into two trial values, they must be multiplied by $F^{-1}(z)$ or the inverse CDF for the specified distribution, which can be thought of as reflecting the random value onto the CDF ($F(z)$) as depicted in Figure 5.13. Note that the distributions shown in quadrant II have different means and standard deviations. In the example "trial" shown in Figure 5.13, failure does not occur since the sample resistance is larger than the sample solicitation [Walbridge 2005].

Statistical Distributions

As shown in Table 5.9, three different types of distribution, namely normal, lognormal, and Gumbel, were used herein to represent the uncertainties associated with various

deterministic model parameters. The equations for the PDF and CDF for each distribution type are given in Table 5.12.

Table 5.12: Statistical distribution equations [Melchers 2002]

Distribution	Equation
Normal	PDF: $f_X(x) = \frac{1}{(2\pi)^{1/2}\sigma_X} \exp\left[-\frac{1}{2}\left(\frac{x-\mu_X}{\sigma_X}\right)^2\right],\ -\infty \le x \le \infty$ CDF: $P(X \le x) = F_X(x) = \frac{1}{(2\pi)^{1/2}} \int_{-\infty}^{s} e^{-\frac{1}{2}v^2}\, dv,\ -\infty \le x \le \infty$ where $s = (x-\mu_x)/\sigma_x$. There is no simple expression for $F_X(x)$.
Lognormal	PDF: $f_x(x) = \frac{1}{(2\pi)^{1/2} xe} \exp\left[-\frac{1}{2}\left(\frac{\ln x - \lambda}{\varepsilon}\right)^2\right],\ 0 \le x \le \infty$ CDF: $F_x(x) = \int_{-\infty}^{x} f_x(u)du = \Phi\left(\frac{\ln x - \lambda}{\varepsilon}\right)$ (no explicit form) where $\lambda = E(\ln x) = \mu_{\ln x}$ and $\varepsilon^2 = \mathrm{var}(\ln x) = \sigma^2_{\ln x}$
Gumbel	PDF: $f_Y(y) = \alpha \exp\left[-\alpha(y-u) - e^{-\alpha(y-u)}\right],\ -\infty \le y \le \infty$ CDF: $F_Y(y) = \exp\left[-e^{-\alpha(y-u)}\right],\ -\infty \le y \le \infty$ where $\alpha^2 = \frac{\pi^2}{6\sigma_Y{}^2}$ and $u = \mu_Y - \frac{1.1396}{\alpha}$

The normal distribution is a basic distribution that can be used to describe any variable that groups about a mean value, e.g., the standard bell curve. This distribution is used for most of the load factors. Figure 5.14 shows an example of normal, lognormal, and Gumbel distribution PDFs. Note that the mean and standard deviation of each of the PDFs shown in Figure 5.14 are 1.0 and 0.5 respectively.

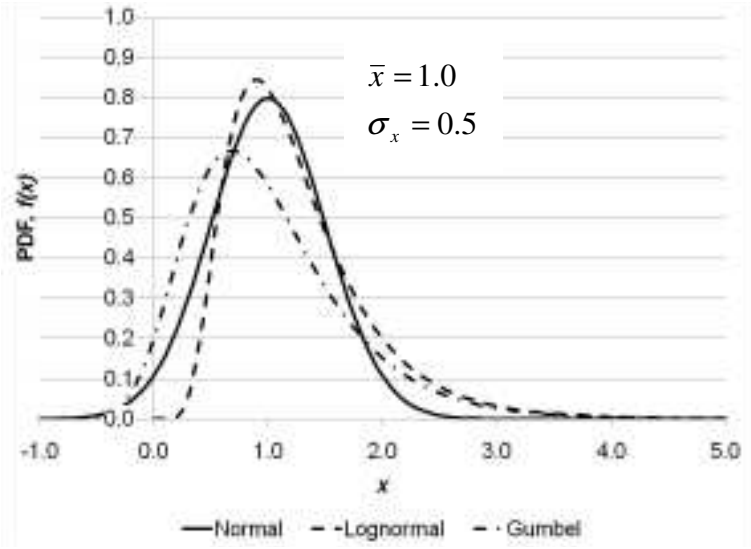

Figure 5.14: Normal, Lognormal, and Gumbel distribution PDFs

In a lognormal distribution, the natural logarithm of a randomly generated value between 0 and 1 has a normal distribution, rather than the number itself. It is a single-tailed distribution; this is why it is commonly used for material strengths and corrosion rates (and other parameters for which a negative trial value is not admissible).

Gumbel distribution is an extreme value distribution. It is commonly used to model the distribution of the extreme values from a number of samples. Like the normal distribution PDF, negative values are possible, but values significantly larger than the mean are more likely.

5.3.6 Reliability

A procedure for determining an appropriate target reliability index, β_{target}, for a given bridge is laid out in Chapter 14 of [CAN/CSA-S6-06]. The categories of the structural system (S), the element (E) under consideration, and the inspection level (INSP) of the structure are considered in deciding the β_{target} value.

System Behaviour

If the structural system under consideration would totally collapse as a result of failure of the element under consideration, the system category is S1. If element failure probably will not result in total collapse, the system category is S2, while if it will lead to local failure only, the system category is S3.

Element Behaviour

If the element under consideration fails suddenly, with little or no warning, the element is classified as E1. If the failure is sudden and not preceded by a warning, but retains some post-failure capacity, then the element category is E2. If the element under consideration fails gradually, with warning of its impending failure, it is E3.

Inspection Level

If the element under consideration is not inspectable, it belongs to the INSP1 category. If, however, the inspection is performed to the satisfaction of the evaluator and the results of the inspection are available to him, it is INSP2. Finally, if the evaluator has directed the inspection of every critical component and evaluation calculations, it is INSP3.

Category Values

The values for the categories described above are provided in Table 5.13.

Table 5.13: Target reliability index, β_{target}, for normal traffic [CAN/CSA-S6-06]

System behaviour category	Element behaviour category	Inspection level		
		INSP1	INSP2	INSP3
S1	E1	4.00	3.75	3.75
	E2	3.75	3.50	3.25
	E3	3.50	3.25	3.00
S2	E1	3.75	3.50	3.50
	E2	3.50	3.25	3.00
	E3	3.25	3.00	2.75
S3	E1	3.50	3.25	3.25
	E2	3.25	3.00	2.75
	E3	3.00	2.75	2.50

For a highway structure like the ones being considered herein, β_{target}, ranges from 2.75 to 3.25. The structural system category for bridges with multiple girders is S2, the elements are in the E3 category, and the inspection level can vary according to the means of the owner and the apparent condition of the structure.

CHAPTER 6: STRUCTURAL ANALYSIS RESULTS AND INTERPRETATION

In this chapter, the deterministic and reliability models developed in Chapter 5 are used to: 1) examine the decline in the structural performance over time due to corrosion for different structure types, 2) perform sensitivity studies to determine the significance of various parameters on the structural performance, and 3) estimate the remaining service lives of two existing structures for which inspection results have been made available by MTO. Steps 1) and 2) are performed on hypothetical structures, designed using the deterministic models from Chapter 5, as explained in the following section.

6.1 Bridge Designs

In order to examine the effects of various parameters on the performance of different structure types, it was necessary to first design a number of hypothetical weathering steel highway bridges with the key structural parameters varied within suitable ranges. The parameters that are the focus of this study are summarized as follows:

1. Corrosion Scenario. For the box and I-girder structures, both corrosion to the web and flange, and to the flange-only, are examined. For the I-girder structures, corrosion to the top of the bottom flange-only is considered as well.
2. Highway Class. Bridges with traffic volumes matching the maximums of those of Highway class A – D (see Table 5.10) are examined.
3. Girder Strength. Bridges with three different girder yield strengths (300, 350, and 480 MPa) are examined.
4. Bridge Span. Bridges with spans of 30, 35, and 40 m are examined.
5. Number of Lanes. Two- and four-lane bridges are examined herein.

Of these five parameters, numbers 3, 4, and 5 each require a new bridge design. Table 6.1 contains a list of the resulting bridge designs and their designations.

Table 6.1: Bridge designs used for sensitivity studies

Bridge number	Girder strength (MPa)	Span (m)	Number of lanes
I-1 & B-1	350	40	4
I-2 & B-2	300	40	4
I-3 & B-3	480	40	4
I-4 & B-4	350	30	4
I-5 & B-5	350	35	4
I-6 & B-6	350	40	2

Bridge B-1 is the standard bridge for this study. Its geometry is based on typical highway overpass structures currently used by the MTO. Similar box and I-girder designs are also analysed to extend the results to other jurisdictions and bridge structures passing over waterways (MTO currently allows the use of I-girders in this case).

6.1.1 Design Criteria

The following criteria (or in some cases, "rules of thumb") have been applied for the design of the single-span box and I-girder bridges:

- All of the plate sizes and girder dimensions are converted from imperial nominal dimensions, to reflect the reality at the time of construction of these structures, as well as the current structural steel supply in Canada.
- A girder-plus-slab span-to-depth ratio of between 24:1 and 25:1 is assumed, based on a review of bridge designs with similar structural configurations.
- The thickness of the bottom flange is never less than the web thickness.
- The slab is 191 mm thick, with a 76.2 mm thick wearing surface.
- Lane widths of 4200 mm and sidewalk and barriers dimensions are assumed as per the existing MTO highway structure designs on hand.
- As per [CAN/CSA-S6-06], the minimum web thickness is taken as 10 mm.

- As per [CAN/CSA-S6-06], the inclination of the web plates for box girders is not allowed to exceed 1 horizontal to 4 vertical (≥ 76.0°).
- For box girder bridges, the number of girders is set to equal the number of lanes. For I-girder bridges, the number of girders is twice the number of lanes.

Based on a review of several actual highway bridges, the structures herein have been designed not to be in excess of 80% of their factored capacity (factored load divided by factored resistance). This design approach was implemented to make the analysis bridges similar to those in the field, all of which showed a significant structural reserve. One source of this supplementary capacity in real structures is the additional plate thickness required by [CAN/CSA-S6-06] for steel structures in corrosion environments. The MTO practice is to add 1 mm to the minimum required section to account for section loss due to corrosion. Figure 6.1 shows the effect of the additional millimetre on design B-1.

For Figure 6.1 and all following figures, M refers to moment failure mode, V refers to shear failure mode, M+V refers to the combined moment and shear failure mode, and B refers to the bearing failure mode. In this figure, the "resistance fraction" is the factored load divided by the factored resistance. A resistance fraction < 1.0 therefore represents a "safe" design. The continuous lines show the resistance fraction of the bridge with the additional millimetre, while the dashed lines show the bridge without it. Also, as mentioned in Chapter 5, the performance of the single-span and two-span bridges is measured at equidistant points along their lengths; the results of this are what is shown in the figures below.

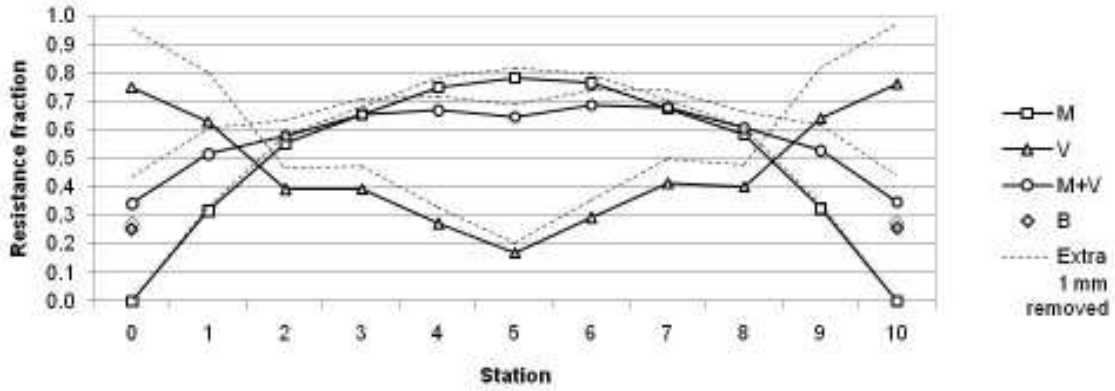

Figure 6.1: Bridge B-1, effect of 1 mm additional thickness

For the simply-supported bridges, the spans were divided into four sections of equal length; different plate sizes were chosen for the abutment and midspan portions. For the two-span continuous bridges, the bridge was divided into three sections, of which the first and the last are the same; 70% of the span length is for the abutment span, while 30% of both spans, for a total of 60% of the span length, is for the pier span. As with the single-span bridge, different plate sizes were chosen for the different spans.

6.1.2 Box Girder Bridge Designs

Table 6.2 and Table 6.3 contain the resulting geometrical data for the abutment and midspan segments of the simply-supported box girder bridges, respectively. Figure 6.2 is a drawing showing the notation of the plate girder elements.

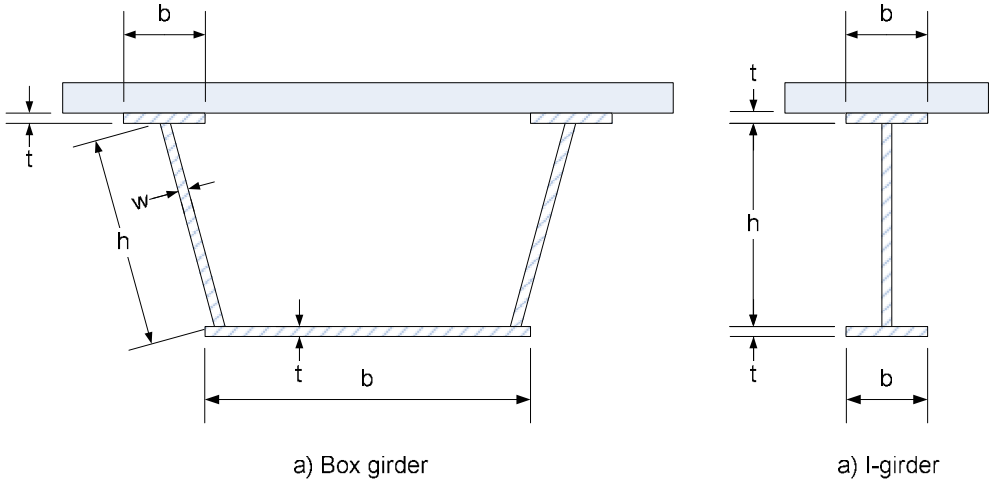

Figure 6.2: Plate geometry dimensions

Table 6.2: Box girder bridge geometry - abutments

Element	Dim.	B-1	B-2	B-3	B-4	B-5	B-6
Top flange	*b*	406	406	406	406	406	406
	t	19.1	19.1	12.7	12.7	19.1	19.1
Webs	*h*	1370	1370	1370	998	1196	1370
	w	12.7	12.7	12.7	11.1	12.7	14.3
	Ø	79.3°	79.3°	79.3°	79.4°	79.5°	79.3°
Bottom flange	*b*	1830	1830	1830	1980	1905	1830
	t	15.9	14.3	12.7	12.7	12.7	15.9
Box height		1350	1350	1350	965	1170	1350

Table 6.3: Box girder bridge geometry - midspan

Element	Dim.	B-1	B-2	B-3	B-4	B-5	B-6
Top flange	*b*	406	406	406	406	406	406
	t	25.4	25.4	15.9	19.1	25.4	25.4
Webs	*h*	1370	1370	1370	998	1196	1370
	w	11.1	11.1	11.1	11.1	11.1	12.7
	Ø	79.3°	79.3°	79.3°	79.4°	79.5°	79.3°
Bottom flange	*b*	1830	1830	1830	1980	1905	1830
	t	20.6	25.4	12.7	15.9	17.5	22.2
Box height		1350	1350	1350	965	1170	1350

In contrast with the design of the shear and moment carrying main girder elements, the design of the bearing stiffeners at the abutments is complicated somewhat by the fact that the design bearing resistance drops suddenly to zero if a slenderness limit is exceeded. In all of the box girder designs, the end plate thickness, w (see Equation 5.5), has been made the same thickness as the girder web, and the bearing length, *N*, has been set to equal 305

mm. The bearing stiffener designs for the box girder bridges are summarized in Table 6.4.

Table 6.4: Box girder geometry – bearing stiffeners

Element	Dim.	B-1	B-2	B-3	B-4	B-5	B-6
Bearing stiffener	*b*	152	152	152	152	152	152
	t	17.5	17.5	20.6	17.5	17.5	17.5

The following diagrams show the resistance fractions for all of the girder designs. These are based on the limit state equations described in Section 5.2.1. The resistance fractions of the box girder bridges are shown in Figure 6.3 through Figure 6.8.

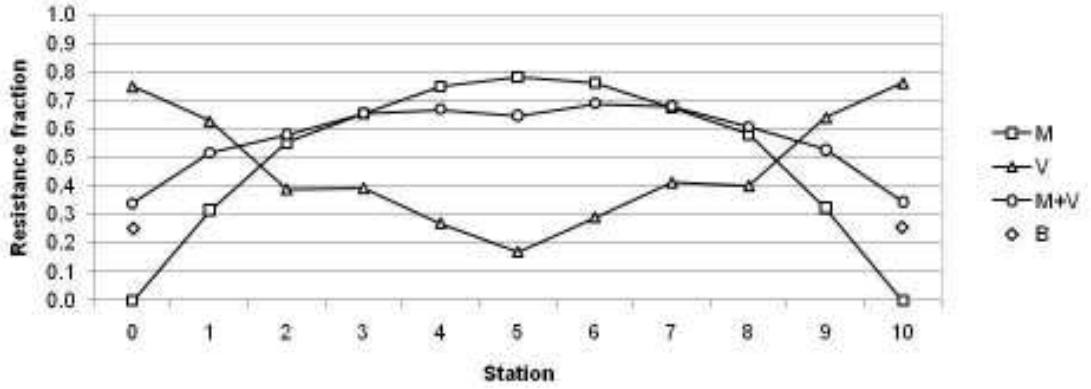

Figure 6.3: Bridge B-1 (base case) resistance fractions

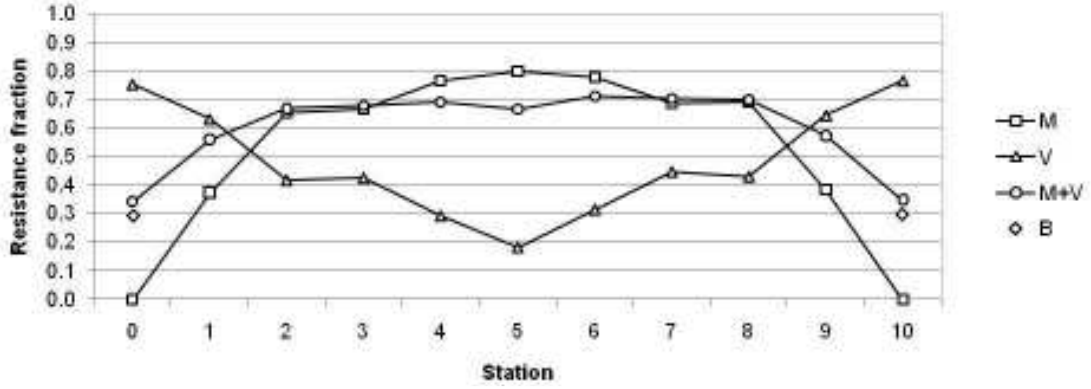

Figure 6.4: Bridge B-2 (300 MPa girder yield strength) resistance fractions

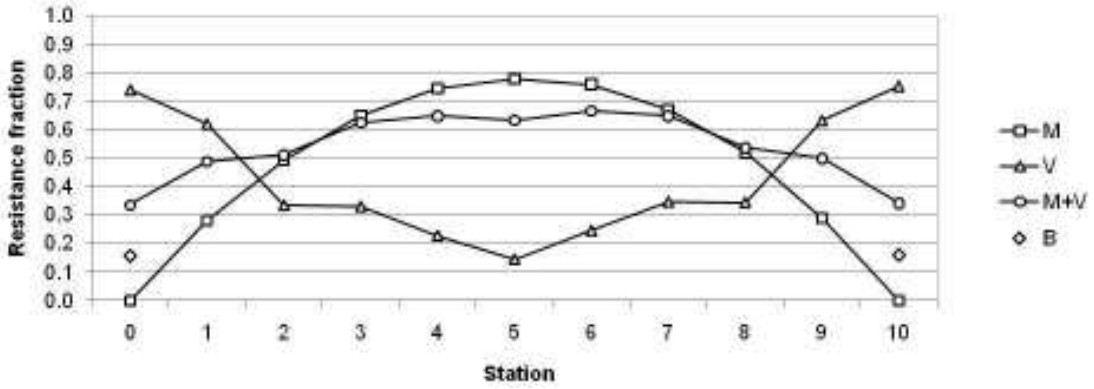

Figure 6.5: Bridge B-3 (480 MPa girder yield strength) resistance fractions

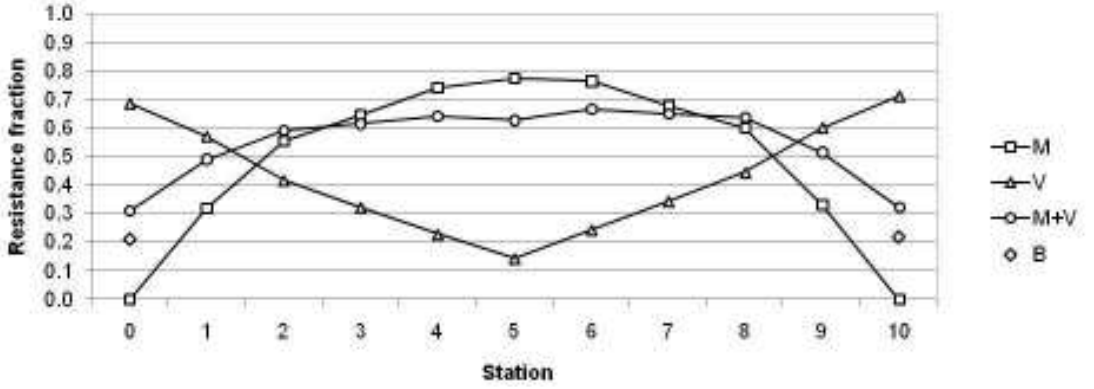

Figure 6.6: Bridge B-4 (30 m span) resistance fractions

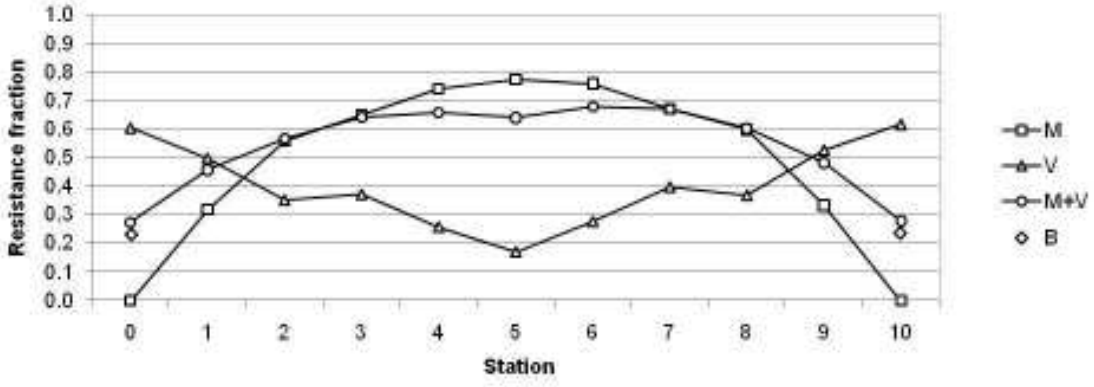

Figure 6.7: Bridge B-5 (35 m span) resistance fractions

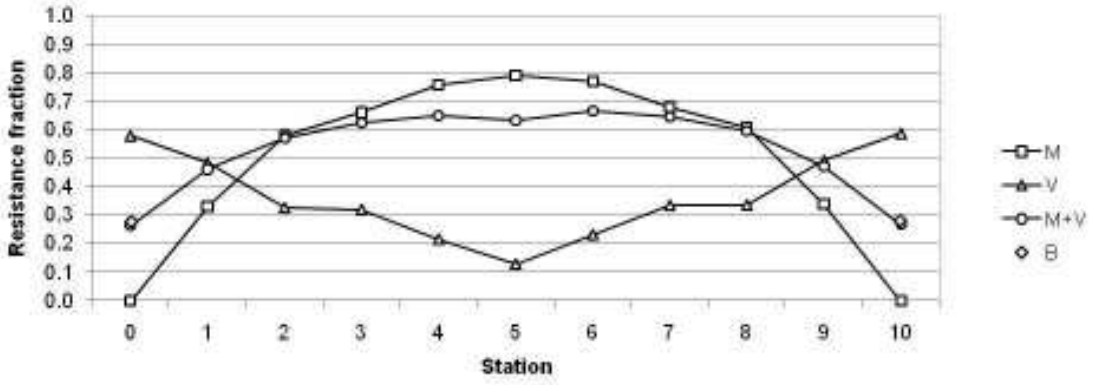

Figure 6.8: Bridge B-6 (2 lanes) resistance fractions

Looking at the above figures, it can be seen that the general trends are similar. The resistance fraction for the maximum shear is frequently substantially lower than the maximum moment resistance fraction. This is because the web is typically a relatively slender section, so the addition or subtraction of 1/16" (the smallest increment of thickness change considered herein) is more noticeable. Also, the calculation for shear resistance, V_r, is nonlinear, i.e. an increase of section or yield strength does not result in a linearly proportional increase in shear resistance (see Equation 5.1).

6.1.3 I-Girder Bridge Designs

Table 6.5 to Table 6.7 contain the geometrical data for the abutment and midspan bridge girder segments and the bearing stiffeners of the simply-supported I-girder bridges, designed using the deterministic model from Chapter 5.

Table 6.5: I-girder geometry - abutments

Element	Dim.	I-1	I-2	I-3	I-4	I-5	I-6
Top flange	*b*	406	406	406	406	406	406
	t	17.5	22.2	14.3	20.6	20.6	22.2
Web	*h*	1370	1370	1370	965	1170	1370
	w	14.3	14.3	14.3	11.1	12.7	14.3
Bottom flange	*b*	406	406	406	406	406	406
	t	17.5	22.2	14.3	20.6	20.6	22.2

Table 6.6: I-girder geometry - midspan

Element	Dim.	I-1	I-2	I-3	I-4	I-5	I-6
Top flange	*b*	610	610	610	508	508	508
	t	28.6	34.9	17.5	27.0	30.2	34.9
Web	*h*	1370	1370	1370	965	1170	1370
	w	12.7	12.7	12.7	11.1	11.1	12.7
Bottom flange	*b*	610	610	610	508	508	508
	t	28.6	34.9	17.5	27.0	30.2	34.9

Table 6.7: I-girder geometry - bearing stiffeners

Element	Dim.	I-1	I-2	I-3	I-4	I-5	I-6
Bearing stiffener	*b*	152	152	152	152	152	152
	t	17.5	17.5	19.1	17.5	17.5	17.5

Similarly to the box girder designs, in all of the I-girder designs, the bearing length was set to equal 305 mm. The resistance fractions for the simply-supported I-girder bridges are presented in Figure 6.9 to Figure 6.14.

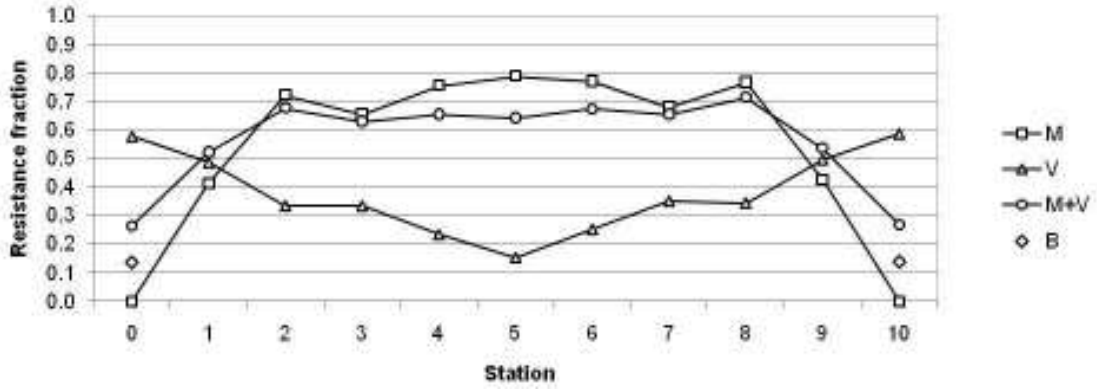

Figure 6.9: Bridge I-1 (base case) design margin

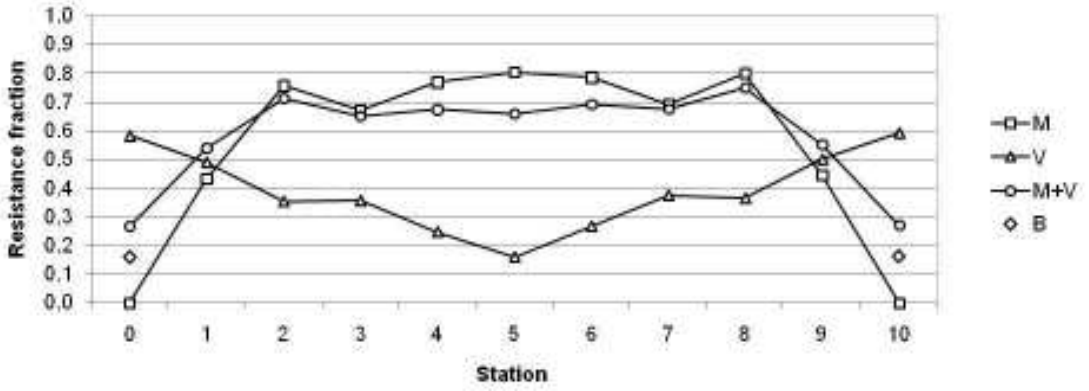

Figure 6.10: Bridge I-2 (300 MPa girder yield strength) design margin

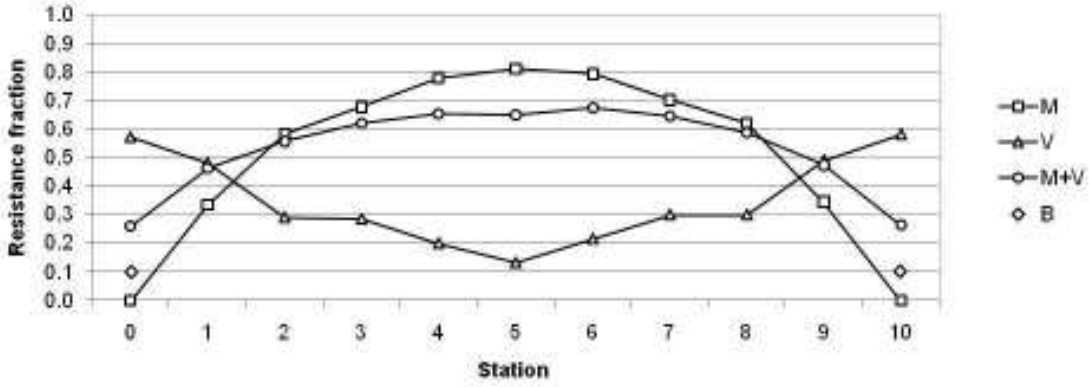

Figure 6.11: Bridge I-3 (480 MPa girder yield strength) design margin

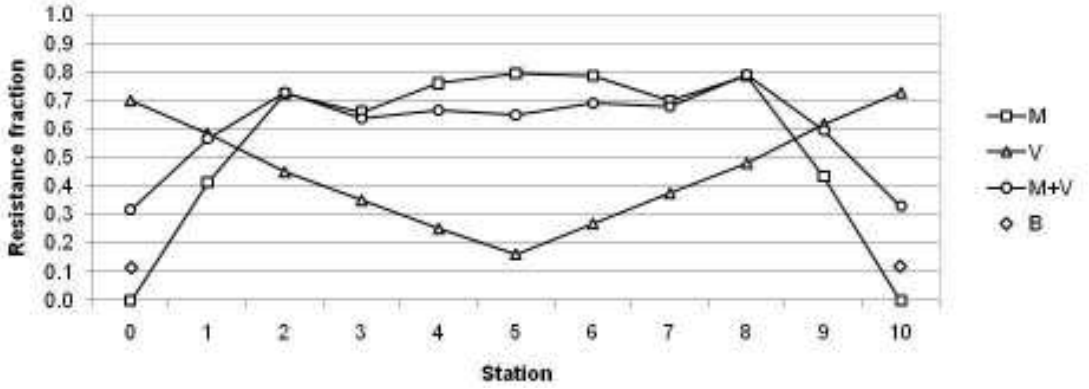

Figure 6.12: Bridge I-4 (30 m span) design margin

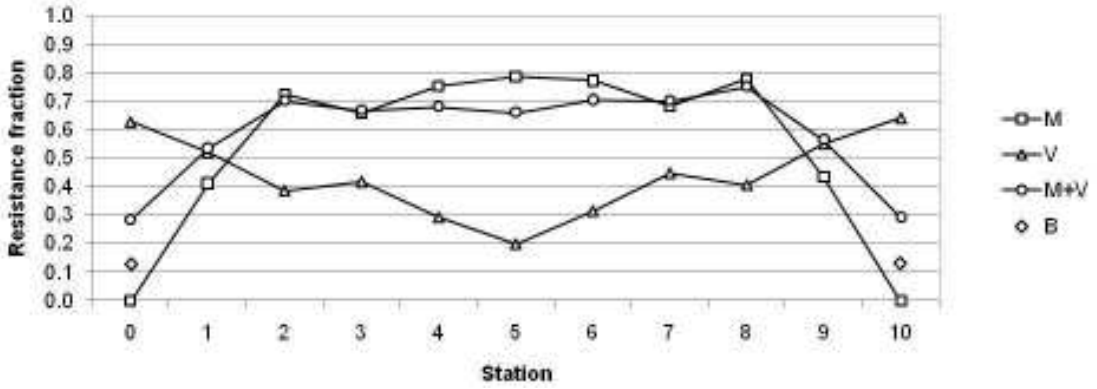

Figure 6.13: Bridge I-5 (35 m span) design margin

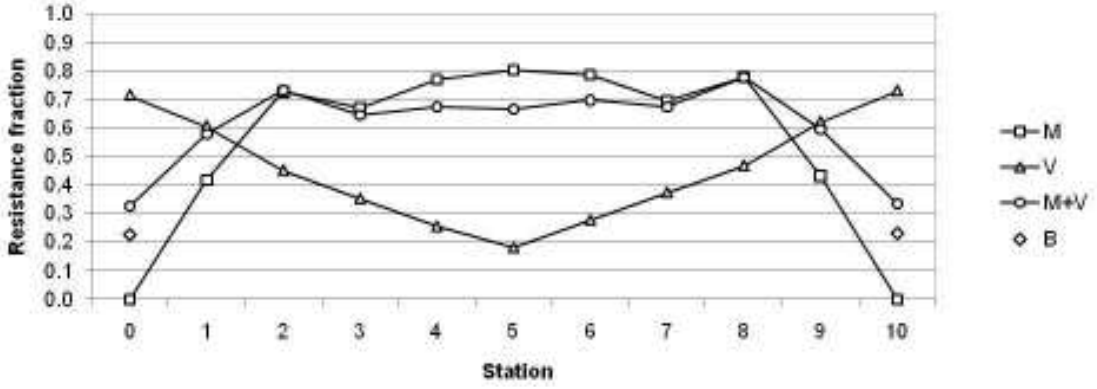

Figure 6.14: Bridge I-6 (2 lane) design margin

6.1.4 Two-Span Continuous Bridge

Only a single two-span continuous box girder bridge geometry is examined in the current study for the following practical reasons:

1) Only the values for the LL shear and moment bias factors, and not the basic live load effect sample histograms, are available in [CAN/CSA-S6-00 Calibration] for two-span continuous bridge girders.

2) The reliability model for two-span continuous bridge analysis is much slower by at least an order of magnitude, since the load effect distributions are dependent on the cross section geometry, which changes as the corrosion progresses. Specifically, using the developed model, a single probabilistic analysis of a two-span bridge for a 100 year service life took around x hours (for MCS with x trials) on a single PC, thus limiting for practical reasons the extent to which this structure type could be reanalyzed in the parametric study.

The two-span bridge model (referred to as T-1 henceforth) is only used to examine the effects of the corrosion scenario for this structure type. Only a structure with two 40 m spans is considered, and only for a single, typical traffic volume (a Class C highway). The two-span continuous bridge girder geometry is described in Table 6.8.

Table 6.8: Two-span girder geometry - general

Element	Dim.	Abutment segment	Pier segment
Top flange	*b*	457	610
	t	25.4	34.9
Webs	*h*	1370	1370
	w	12.7	12.7
	Ø	79.3°	79.3°
Bottom flange	*b*	1830	1830
	t	12.7	34.9
Box height		1350	1350

Regarding the bearing flange geometry, the same was assumptions are made here as for the simply-supported box girder: i.e. the girder end plates are set to be the same thickness as the adjacent web. The bearing plate arrangement is summarized in Table 6.9.

Table 6.9: Two-span girder geometry - bearing

Element	Dim.	Abutment bearing	Pier bearing
Bearing stiffener	*b*	152	152
	t	17.5	25.4

Here, as with the simply-supported bridges, a bearing length of 305 mm is used. Figure 6.15 is graph of the resistance fractions for the moment, shear, and bearing failure modes.

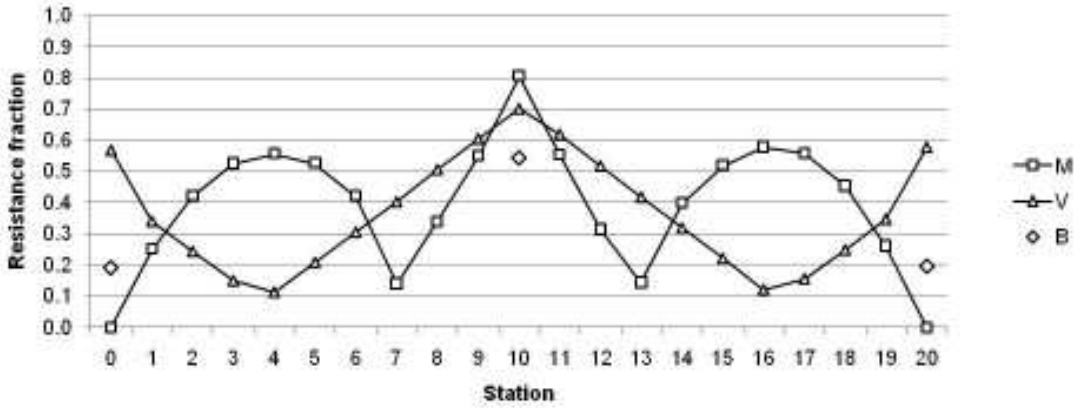

Figure 6.15: Bridge T-1 (base case) design margin

For the two-span continuous bridge, the shear + moment failure mode is not considered since out-of-phase effects were not calculated. The shear + moment case combines the maximum values at a given location; however, because out-of-phase effects were not calculated, the values which are given do not actually occur concurrently. These values do not occur simultaneously with respect to the moving truck load. Rather, the maximum shear and moment values at a given location are caused by the live load acting at different points along the bridge length. This effect is less significant for the single-span bridge, because the maximum values for shear and moment do not occur at the same location; maximum shear occurs at the abutments, and maximum moment occurs at midspan. For the two-span bridge, however, the maximum shear and moment values both occur at the pier. Therefore, shear and moment calculations which ignore the phase effects return overly conservative results for the shear + moment case. On the other hand, it is likely that the results of an accurate calculation of the shear + moment case would be relatively minor as compared to the results of shear and moment separately, since the truck cannot cause maximum shear and moment loading from a single location along the bridge span. Therefore, it has been deemed safe to omit this failure mode.

6.2 Base Case Analysis

The following sections contain the results of the base case analyses for each bridge type (Bridges B-1, G-1, and T-1). After this, a comparison of the results is presented. For the simply-supported bridge base cases, corrosion occurs to the web and flange, and a Class A traffic rate is assumed. The two-span bridge is also subjected to web + flange corrosion, but a Class C traffic rate is assumed in this case.

For evaluating the structural performances of the various bridge types, it should be remembered that, according to [CAN/CSA-S6-06], the target reliability for highway structures ranges from 2.75 to 3.25, depending on the inspection level. Also according to [CAN/CSA-S6-06], the minimum design life of a bridge structure is 75 years.

6.2.1 Simply-Supported Box Girder Bridge Base Case

The following are the results for the 40 m simply-supported box girder bridge (B-1), the "standard" used for comparison purposes in the sensitivity studies presented herein. Figure 6.16 to Figure 6.18 show the results for this bridge subjected to the corrosion penetration rates for urban, marine, and rural environments, respectively. For all the base case reliability graphs, the grey dashed lines indicate β = 2.75 and 3.25. In these figures, separate curves are shown for each individual ultimate limit state. A "total" curve is also added, representing the reliability for all of the limit states combined.

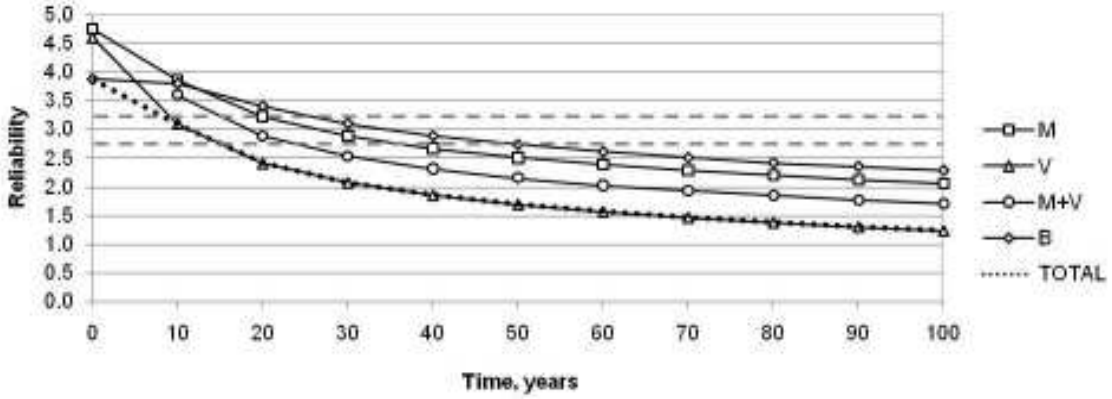

Figure 6.16: Bridge B-1, urban corrosion rate

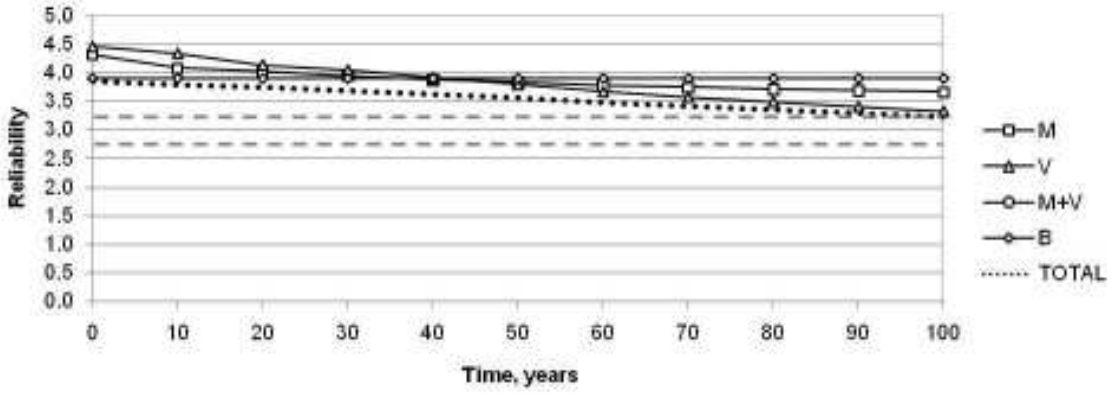

Figure 6.17: Bridge B-1, marine corrosion rate

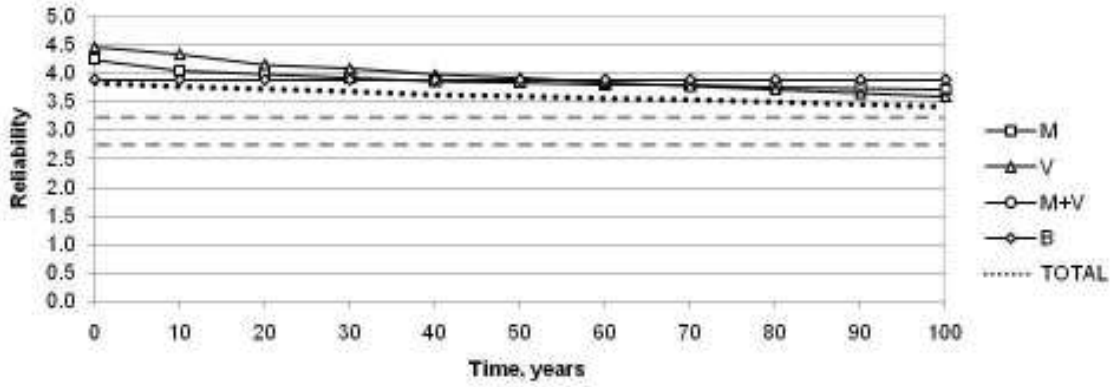

Figure 6.18: Bridge B-1, rural corrosion rate

Based on these figures, the following comments can be made regarding the structural performance of the simply-supported box girder bridge base case (B-1):

- At the urban corrosion rate, the structure is so affected by the section loss that all of the failure modes are capable of causing the reliability index to drop below the minimum level of 2.75 before the planned service life is reached (75 years).
- At the marine and rural corrosion rates, none of the failure modes (alone or in combination) bring the structure to a reliability of less than 3.25 within the 100 year analysis period.
- Corrosion at the assumed urban rate causes an initially steep rate of decline in reliability for all of the failure modes examined; however, this decline almost immediately begins to level off.
- For the marine and rural corrosion rates, the reliability curves for all of the failure modes have an approximately constant rate of decline; however, the rural rate of decline is less than the marine.
- For every corrosion rate, the first mode of failure (at time = 0 years) is bearing. It is later surpassed by shear and moment failure modes. How much later depends on the assumed corrosion rate (urban, marine, or rural).
- For the marine and rural corrosion rates, the shear failure mode has the steepest rate of decline; the bearing failure mode has the flattest.
- In all cases, shear eventually becomes the definitive failure mode of the structure.

- The shear + moment failure mode only ever occurs in the bridge subjected to the urban corrosion rate.

The eventual preponderance of the shear failure mode is due to the relatively thin section of the web as compared to the flange. The bearing reliability, on the other hand, does not appear to be affected by corrosion occurring at the assumed marine and rural rates. An investigation of the input parameter values that resulted in bearing failures showed that the bearing failures that do occur are the result of a combination of a higher-than-expected girder yield strength (which essentially causes the slenderness limit in the bearing formula to "trip" earlier) and high dead or live load effect bias factors.

6.2.2 Simply-Supported I-Girder Bridge Base Case

Figure 6.19 to Figure 6.21 show the output for the I-1 simply-supported I-girder bridge.

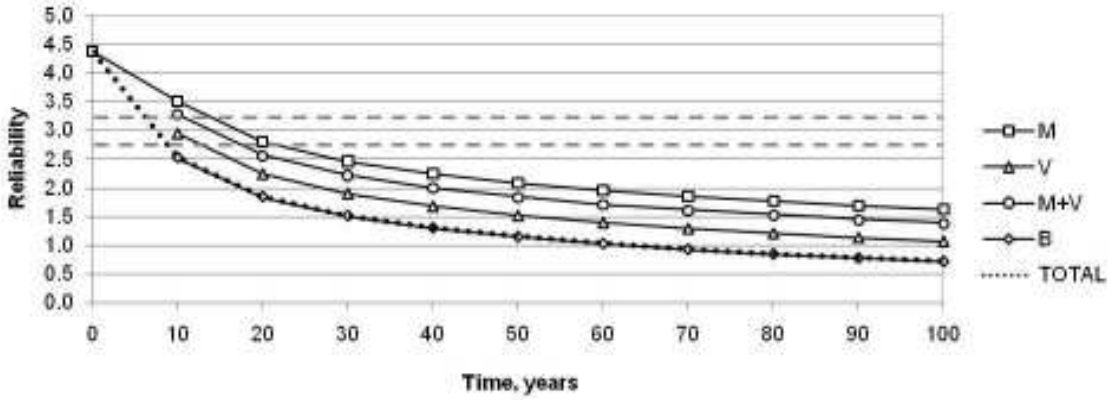

Figure 6.19: Bridge I-1, urban corrosion rate

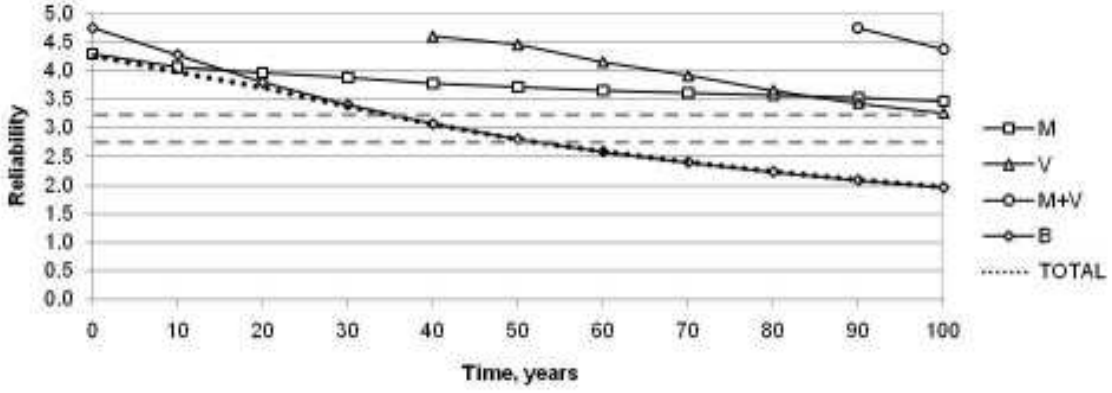

Figure 6.20: Bridge I-1, marine corrosion rate

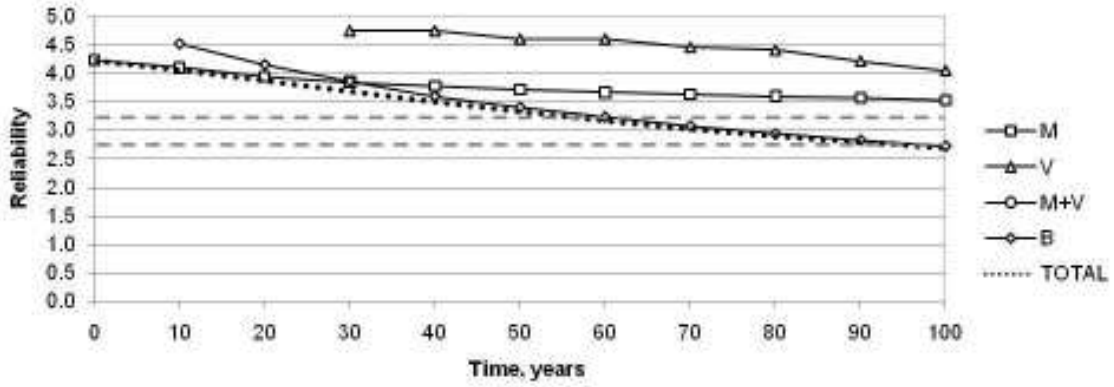

Figure 6.21: Bridge I-1, rural corrosion rate

For the simply-supported I-girder bridge base case (Bridge I-1).

- At the urban corrosion rate, all four examined ultimate limit states can cause the reliability of the I-girder structure to drop below the minimum allowable level of 2.75 before the planned service life is reached (75 years).
- For all three corrosion rates, at year zero, the critical mode of failure is moment.
- Over time, at all three corrosion rates, the critical failure mode shifts to bearing.
- The shear + moment case has little or no influence on the combined (total) reliability curve for any of the assumed corrosion rates.

For the I-girder, the bearing failure mode has a greater effect over the long term because all of the bearing flanges are exposed to corrosion, unlike for the box girder bridge where half of them are sealed inside the girder. In this case, it is the thickness loss that causes the slenderness ratio to "trip". Moment resistance is provided primarily by the bottom flange, which has a thicker section; it is less affected by progressive corrosion progression, so its reliability degradation is slower.

6.2.3 Two-Span Continuous Box-Girder Bridge Base Case

Figure 6.22 to Figure 6.24 show the output for the two-span bridge base case.

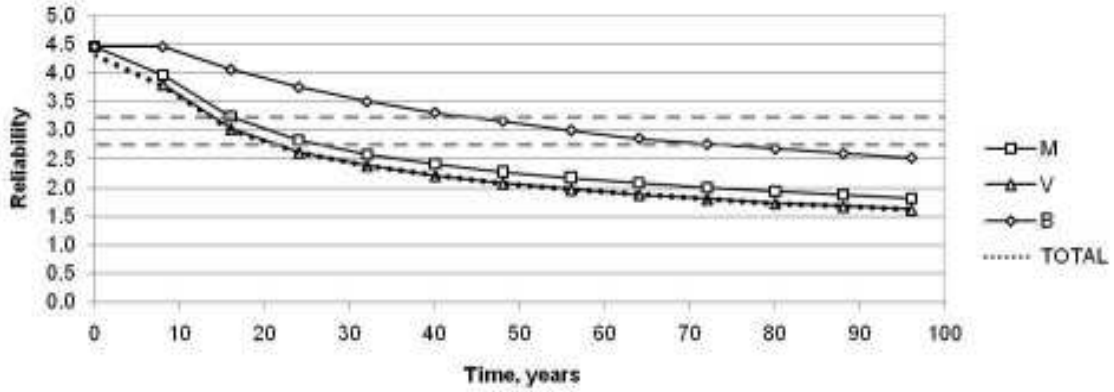

Figure 6.22: Bridge T-1, urban corrosion rate

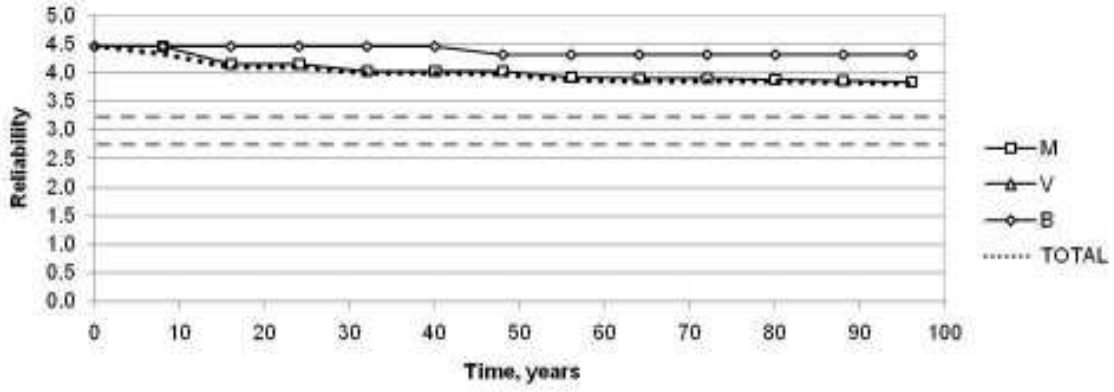

Figure 6.23: Bridge T-1, marine corrosion rate

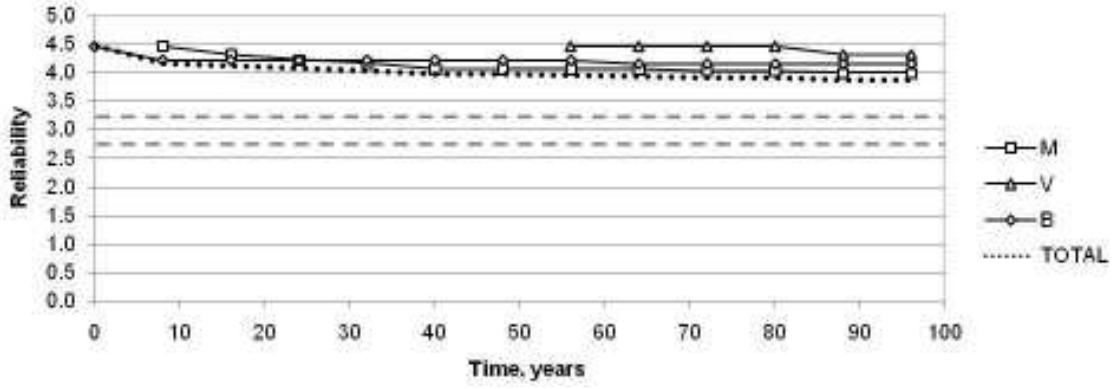

Figure 6.24: Bridge T-1, rural corrosion rate

For the two-span continuous box girder bridge (Bridge T-1):

- Only at the urban corrosion does the reliability of the structure drop to 2.75 or lower within the analysis period of 100 years.
- At the urban corrosion rate, shear is the dominant failure mode.

- At the marine and rural corrosion rates, moment is the dominant failure mode. Shear only appears in the rural case, and failures are rare.
- The structure's performance at the marine and rural corrosion rates is similar.

The appearance of the shear failure mode in the rural corrosion rate graph, and not in the marine corrosion rate graph, is likely due to the randomness of the problem, since the marine corrosion rate should be slightly higher.

6.2.4 Base Case Comparison

Figure 6.25 is a comparison of the reliability versus time curves for the three base cases presented in the previous sections under the three assumed corrosion rates, where all ULS failure modes are considered together.

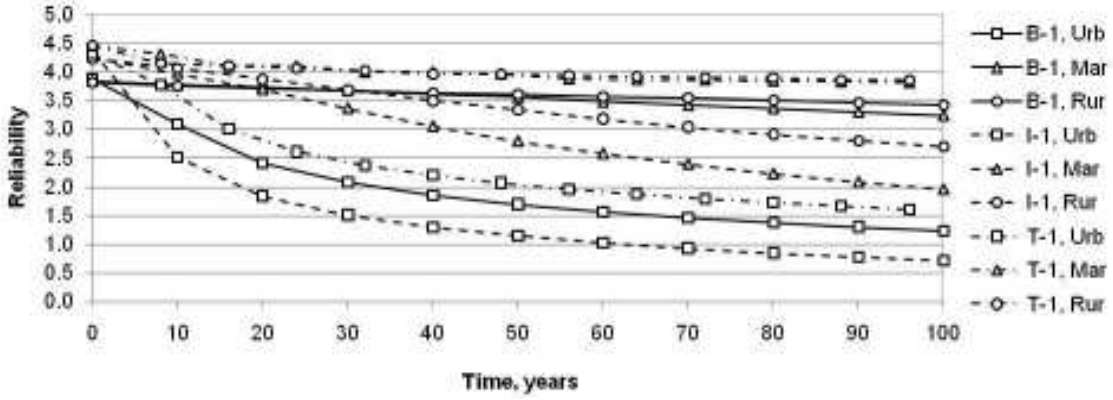

Figure 6.25: Base case summary, combined failure modes, all corrosion rates

Figure 6.26 is a comparison of the reliability versus time curves for the base cases under the three assumed corrosion rates, where only moment failure mode is considered.

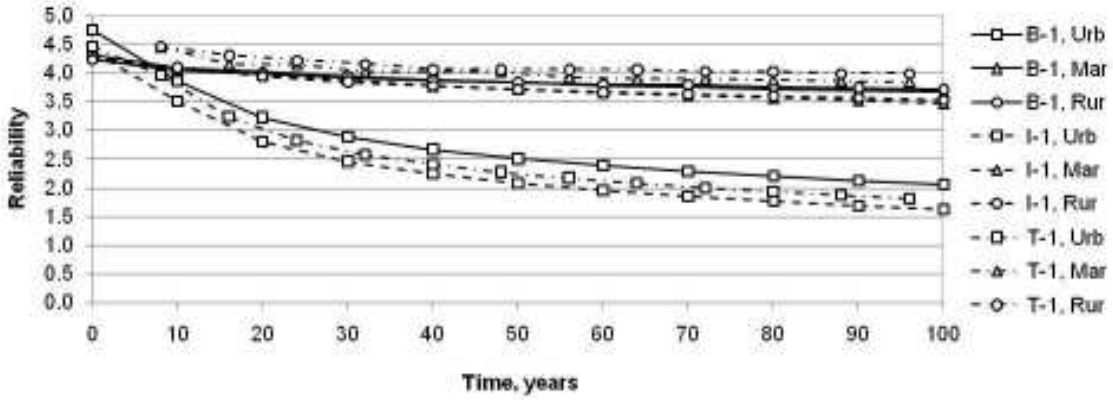

Figure 6.26: Base case summary, moment failure mode, all corrosion rates

Figure 6.27 is a comparison of the reliability versus time curves for the base cases under the three assumed corrosion rates, where only shear failure mode is considered.

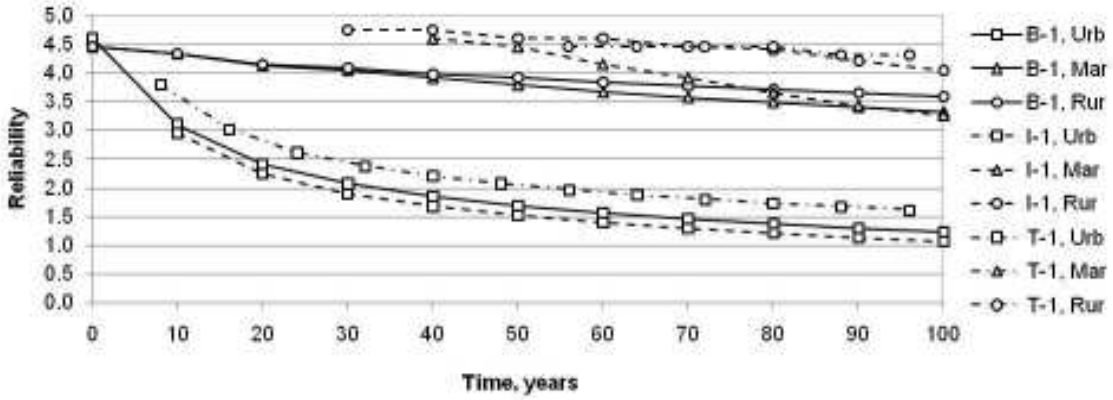

Figure 6.27: Base case summary, shear failure mode, all corrosion rates

When the base cases for the three bridge types are compared, it can be seen that:

- The I-girder bridge is the most susceptible to corrosion, followed by the box girder bridge and the two-span continuous box-girder bridge, in that order.
- For corrosion rates other than urban, only the I-girder bridge has a reliability level that ever drops below 2.75 within the planned service life (75 years).

The I-girder bridge is more susceptible to corrosion than the other bridges because both surfaces of the girder web and flange, as well as the bearing flanges, experience corrosion penetration. Since both types of bridges were designed with a 20% reserve in their structural capacity, this confirms the [CAN/CSA-S6-06] ordinance stating that steel members should have additional thickness for each surface exposed.

The continuous box girder fares better than the single-span box girder in part because the critical failure mode, i.e. bending moment at the midspan, is counteracted by a relatively thick steel element (the midspan bottom flange) that is relatively resistant to corrosion. It is possible that the hyperstatic nature of the two-span continuous bridge also plays a role, as with this structure type, as thinning of the bottom flange may simply lead to a transfer of moment from the midspan to the interior support.

As noted in Section 5.2.1, according to [CAN/CSA-S6-06] the bearing stiffeners only contribute to bearing resistance when $b/t \leq 200/\sqrt{F_{yg}}$, where b and t are the width and

thickness of the stiffener and F_{yg} is the yield strength of the plate. According to [CISC 2006], the width-thickness limits are not related to the class of section, but are a function of other considerations, i.e., the edge conditions and residual stresses of the component. Because this slenderness ratio is a function of the yield stress of the girder, it introduces a non-rational element into the bearing reliability calculations. For example, where the yield strength is higher, a thicker plate is required for the bearing stiffener, even though its maximum bearing stress (as opposed to overall resistance) is higher (see Equations 5.5 and 5.15). Where the use of higher strength steel should result in a smaller required section, here the opposite is the result. Also, because steel strength is one of the statistical variables, higher strength bearing plates result in immediate failure of the bridge, a result which, again, is non-rational. Because of misconceptions which may result from this, the bearing failure mode is not considered in the sensitivity studies.

6.3 Sensitivity Studies

6.3.1 Corrosion Scenario

Simply-Supported Box Girder Bridge

Figure 6.28 to Figure 6.30 show the shear and moment failure mode output for the B-1 box girder bridge subjected to the three corrosion rates and several different corrosion "scenarios". In these figures, the W+F corrosion scenario refers to corrosion of the web and the flange together, while the F scenario refers to corrosion of the flange-only (see Figure 5.10 for a diagram of the corrosion locations). Regarding the moment failure, the first corrosion scenario can be thought of as a "worst case" scenario. The second was considered herein as it was believed to be more representative of the corrosion observed on overpass structures, in the splash zones of trucks passing underneath (see Figure 1.1).

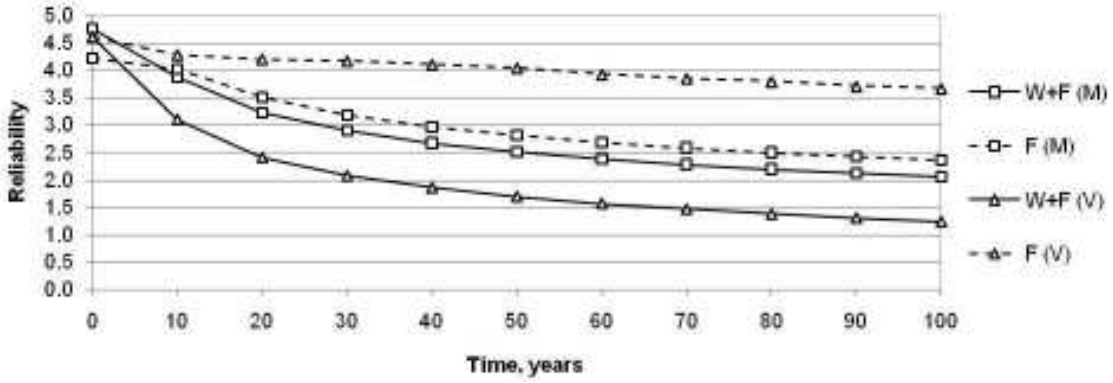

Figure 6.28: Bridge B-1, urban corrosion rate, corrosion scenario varied

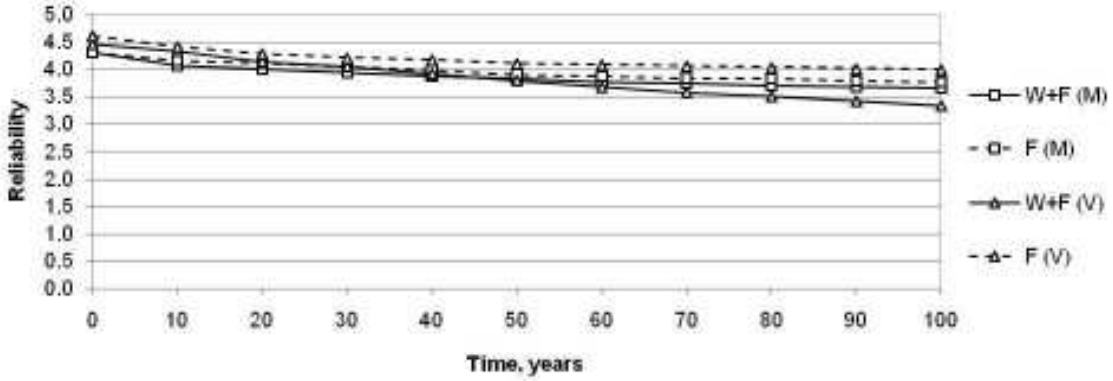

Figure 6.29: Bridge B-1, marine corrosion rate, corrosion scenario varied

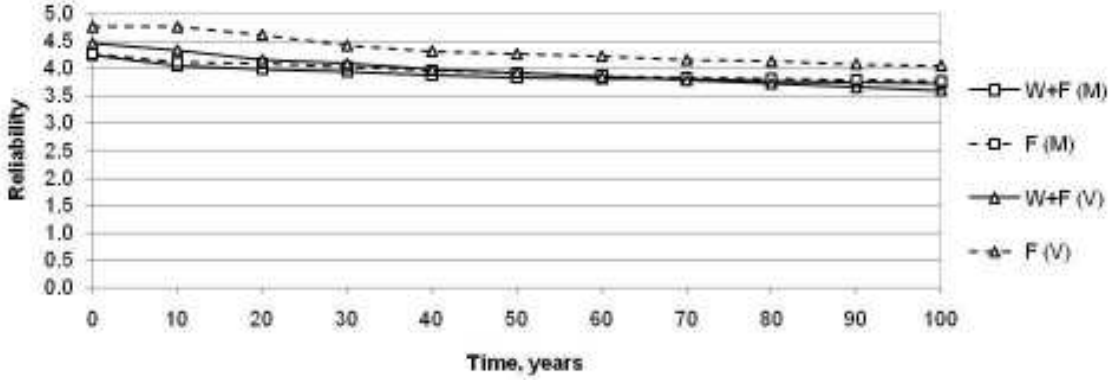

Figure 6.30: Bridge B-1, rural corrosion rate, corrosion scenario varied

Based on Figure 6.28 to Figure 6.30, the following observations are made:

- At all corrosion rates, corrosion to the flange-only leads to a noticeable increase in the reliability due to moment failure. However, there is a very significant increase in the reliability relating to the shear resistance. The moment values are relatively similar, but the shear values are very different.

- At the urban corrosion rate, the effect of web corrosion is noticeable; this is less true for the marine corrosion rate, and not true for the rural corrosion rate.
- At the urban corrosion rate, the uncorroded web more than triples the service life of the structure (15 years vs. 55 years).

I-Girder Bridge

Figure 6.31 to Figure 6.33 present the results of a similar set of analyses on the simply-supported I-girder structure (Bridge I-1). In this case, however, three corrosion scenarios are examined: corrosion to the web and both surfaces of the flange (W+F), corrosion to both surfaces of the flange (F), and corrosion to the top of the flange-only (TOF) (see Figure 5.5 for a diagram of the corrosion locations).

Shear failure, being consequent upon corrosion of the web, only occurred in the web + flange corrosion scenario, so this is the only one to appear on the following figures.

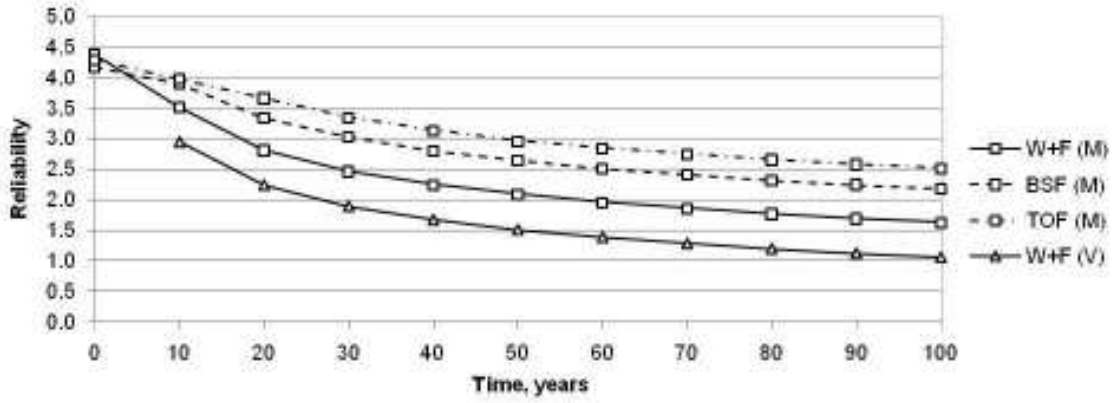

Figure 6.31: Bridge I-1, urban corrosion rate, corrosion scenario varied

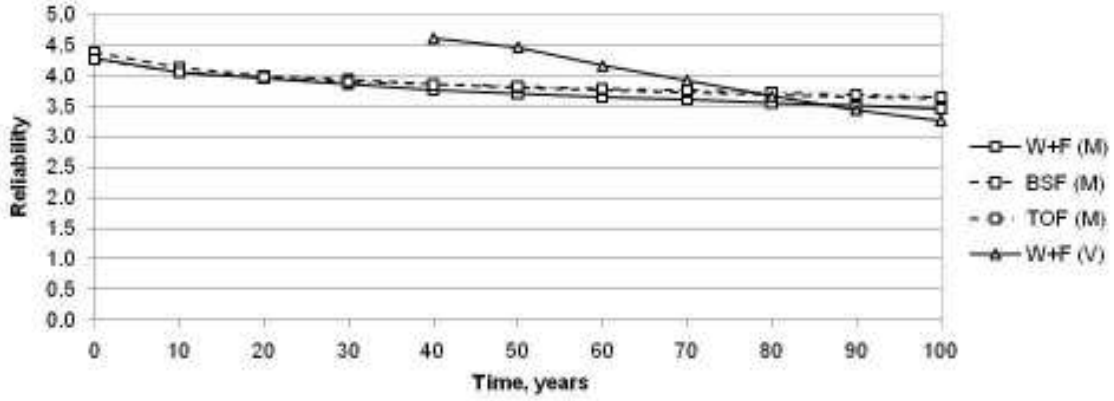

Figure 6.32: Bridge I-1, marine corrosion rate, corrosion scenario varied

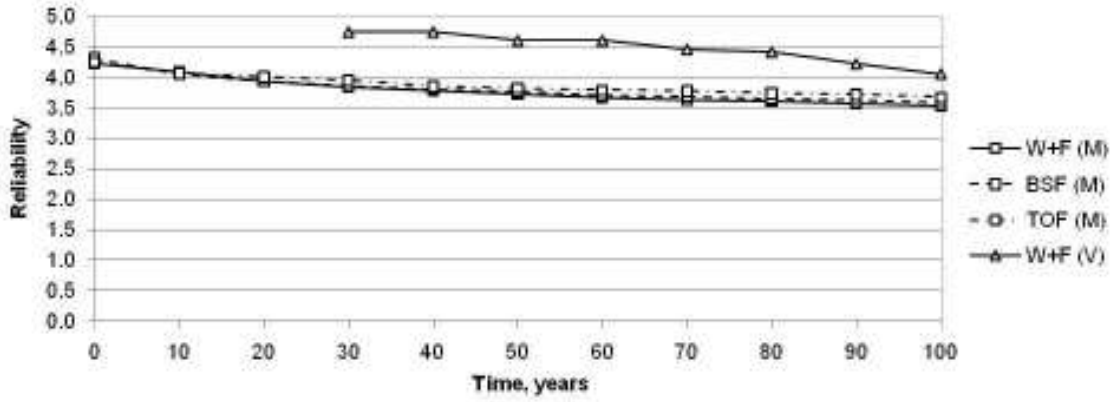

Figure 6.33: Bridge I-1, rural corrosion rate, corrosion scenario varied

Based on Figure 6.31 to Figure 6.33, the following observations are made:

- At all corrosion rates, corrosion to the web and the flange together cause the greatest decline in reliability; however, it is only at the urban corrosion rate that this decline differs substantially from the other scenarios.
- At the urban corrosion rate, there is a significant difference in the results for the different corrosion scenarios; however, at the lower corrosion rates the difference diminishes to the point that it becomes negligible.
- At the marine and rural corrosion rates, the I-1 bridge does not drop below 3.25 over the 100 year analysis period.

The reason for the similarity between the reliability lines at the marine and rural corrosion rates is that the web in fact contributes a relatively small amount to the moment resistance.

Two-Span Continuous Box-Girder Bridge

Figure 6.34 to Figure 6.36 show the effect of progressive corrosion on the two-span continuous box-girder bridge. In this case, both moment and shear failures occur.

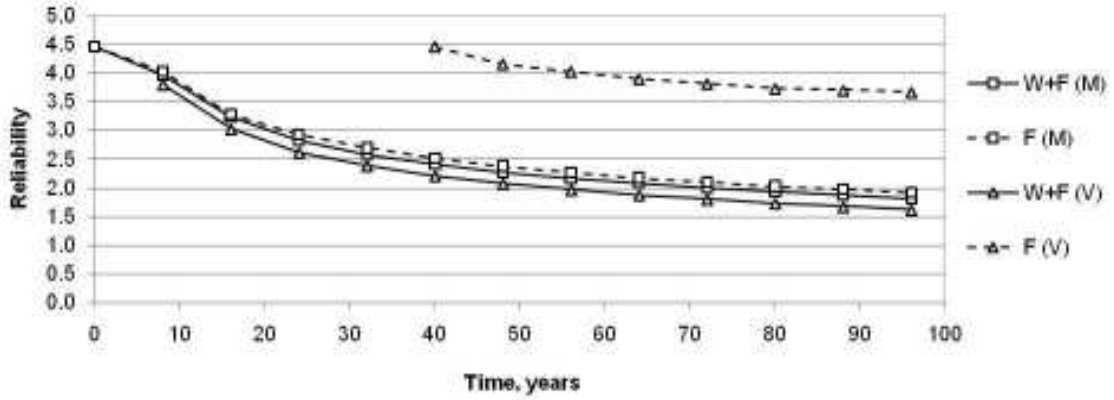

Figure 6.34: Bridge T-1, urban corrosion rate, corrosion scenario varied

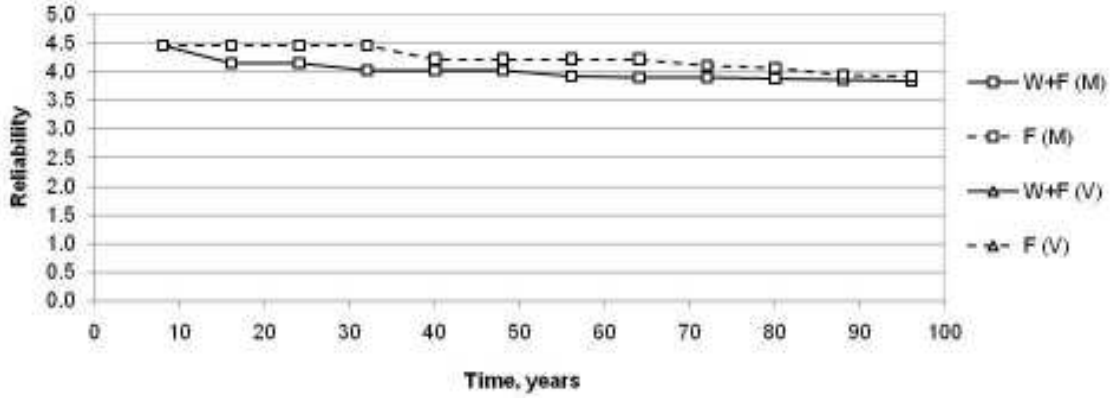

Figure 6.35: Bridge T-1, marine corrosion rate, corrosion scenario varied

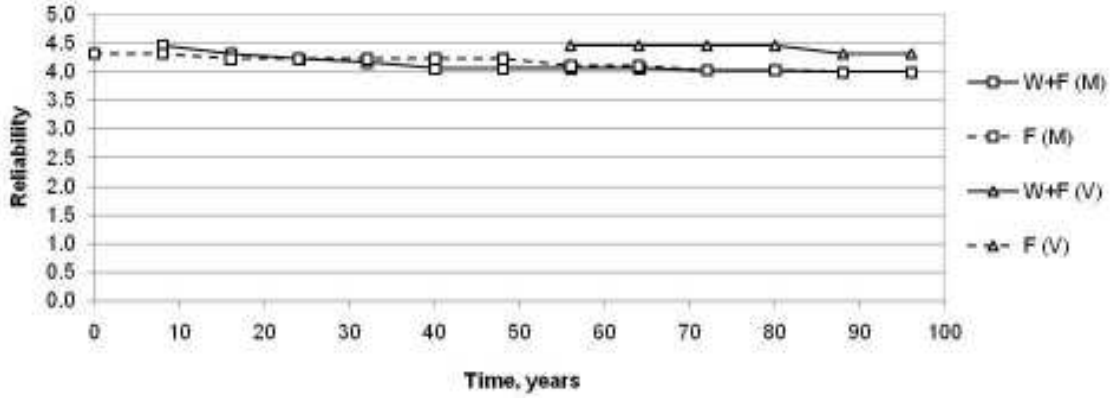

Figure 6.36: Bridge T-1, rural corrosion rate, corrosion scenario varied

Based on the data in Figure 6.34 to Figure 6.36, the following observations are made:

- At the urban corrosion rate, the reliability curves for the moment failure mode with and without corrosion to the web are very similar.

- At the urban corrosion rate, the effect of the shear failure modes is vastly increased if the web is included in the corrosion scenario.
- At the marine and rural corrosion rates, the T-1 bridge does not drop below 3.25 over the 100 year analysis period, regardless of the corrosion scenario.

It should be noted that most of the moment failures for the two-span continuous bridge are at the pier where negative bending occurs; the failures are a result of the flange failing to provide sufficient compression resistance. This suggests again that the web does not contribute significantly to the negative moment resistance.

Comparison

Based on the above results, the following observations are made:

- When only the flange is corroding, none of the bridge types has a shear reliability value below 3.25 over a 100 year service life.
- Regarding moment resistance at the urban corrosion rate, the two-span bridge appears to benefit least from flange-only corrosion, followed by the single-span box girder and I-girder, respectively.

6.3.2 Highway Class

Box Girder Bridge

Figure 6.37 to Figure 6.39 show the reliability results for 40 m long box bridge, subject to the various corrosion rates, and with different ADTT values (see Table 5.11 for these values). The ADTT is related to the live load shear and moment bias factors.

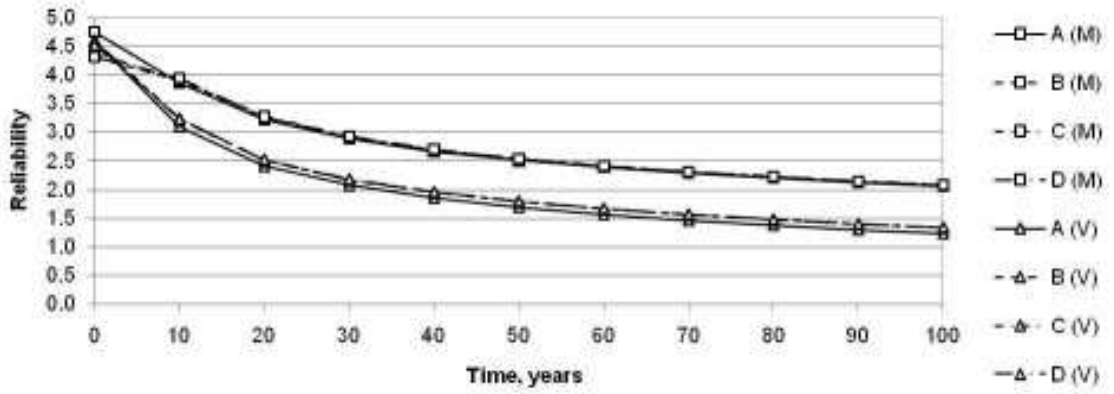

Figure 6.37: Bridge B-1, urban corrosion rate, highway class varied

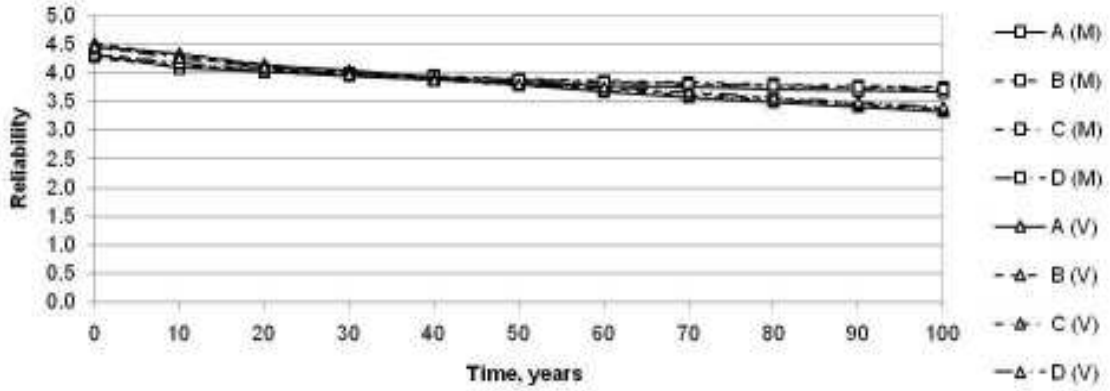

Figure 6.38: Bridge B-1, marine corrosion rate, highway class varied

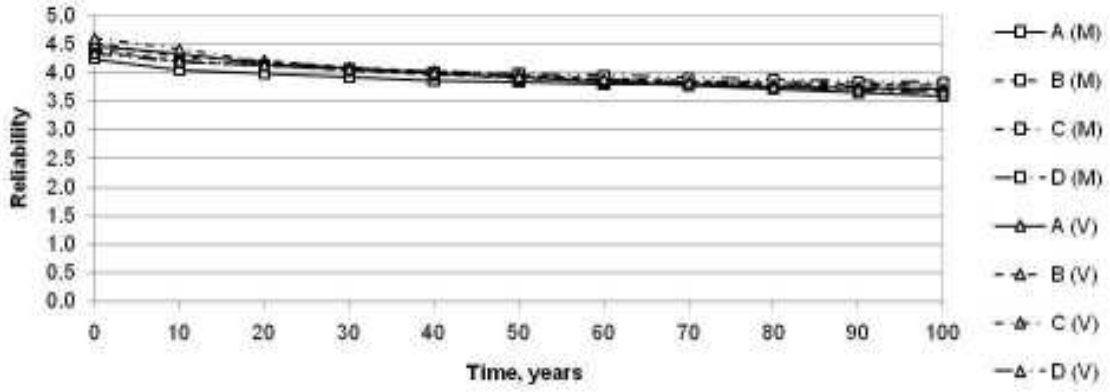

Figure 6.39: Bridge B-1, rural corrosion rate, highway class varied

I-Girder Bridge

The results of a similar study are presented below for the 40 m long I-girder bridge.

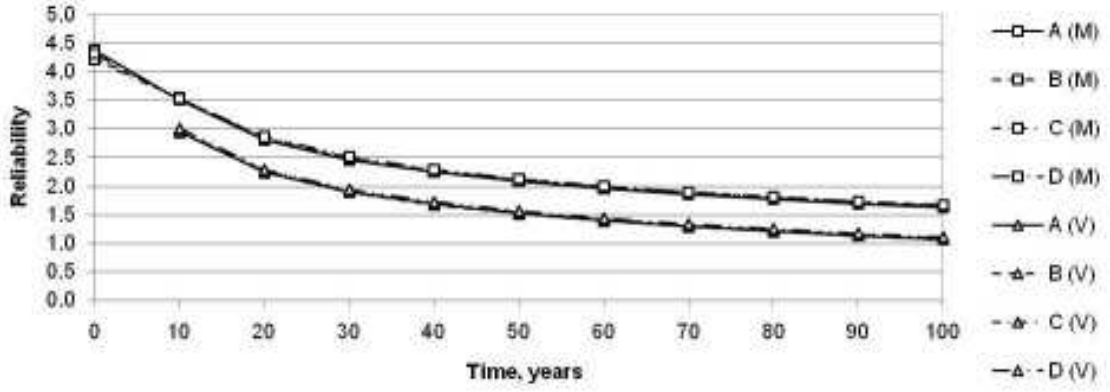

Figure 6.40: Bridge I-1, urban corrosion rate, highway class varied

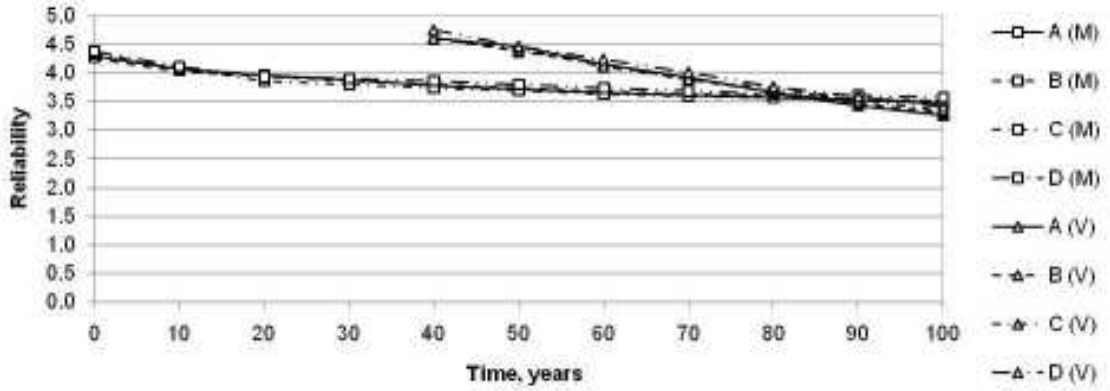

Figure 6.41: Bridge I-1, marine corrosion rate, highway class varied

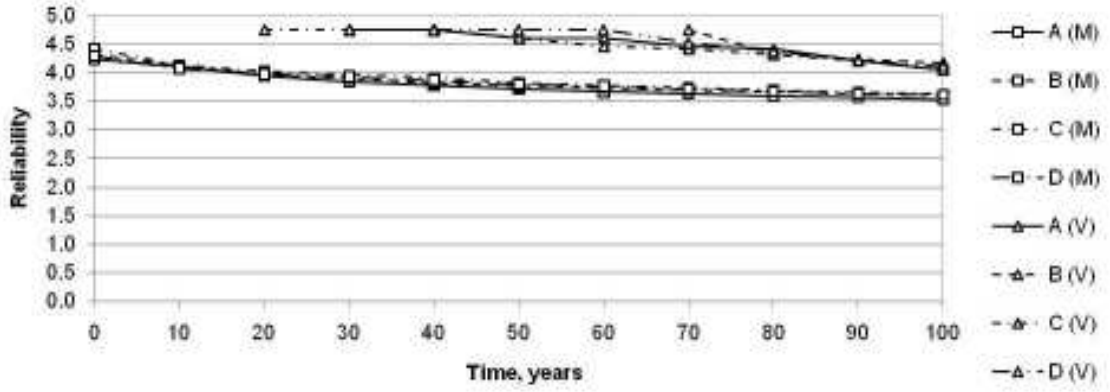

Figure 6.42: Bridge I-1, rural corrosion rate, highway class varied

Comparison

Based on these figures, it can be concluded that the highway class is not an important factor for either girder type. This can be explained by the fact that as the traffic volume increases, the mean of the bias factor for the extreme live load effect tends to increase. However, the standard deviation tends to decrease (see Table 5.11).

6.3.3 Girder Yield Strength

Box Girder Bridges

Figure 6.43 to Figure 6.45 show the results for bridges where the girders are composed of steels with various yield strengths. The bridges being compared here are B-1 (F_{yg} = 350 MPa), B-2 (F_{yg} = 300 MPa), and B-3 (F_{yg} = 480 MPa). Note that the analysis in this section assumes that all of the steel grades corrode at the same rate.

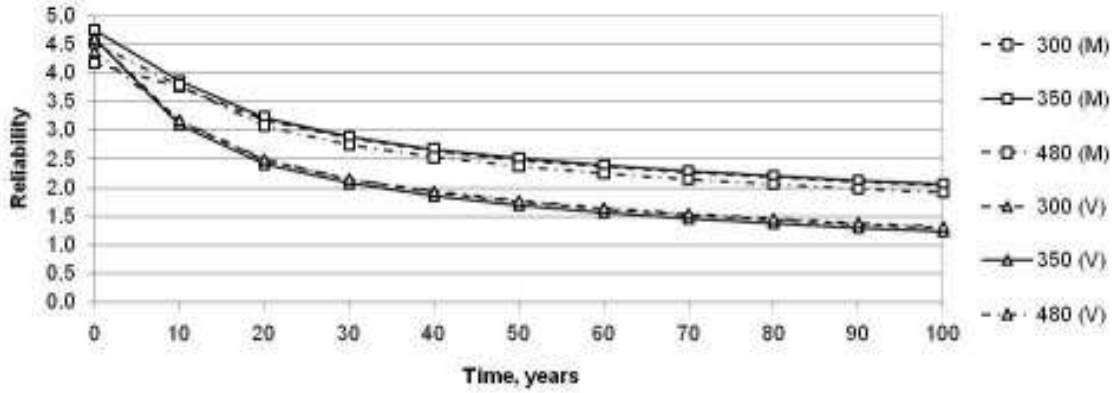

Figure 6.43: Bridges B-1, B-2, B-3, urban corrosion rate.

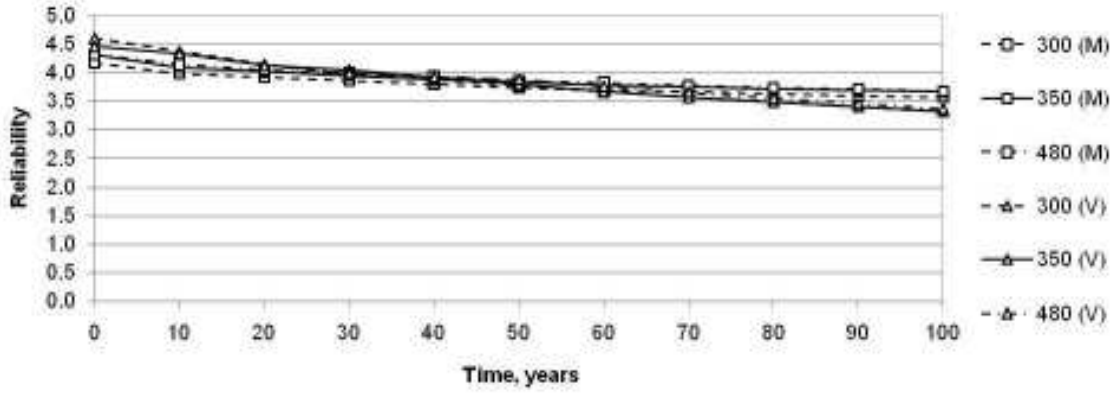

Figure 6.44: Bridges B-1, B-2, B-3, marine corrosion

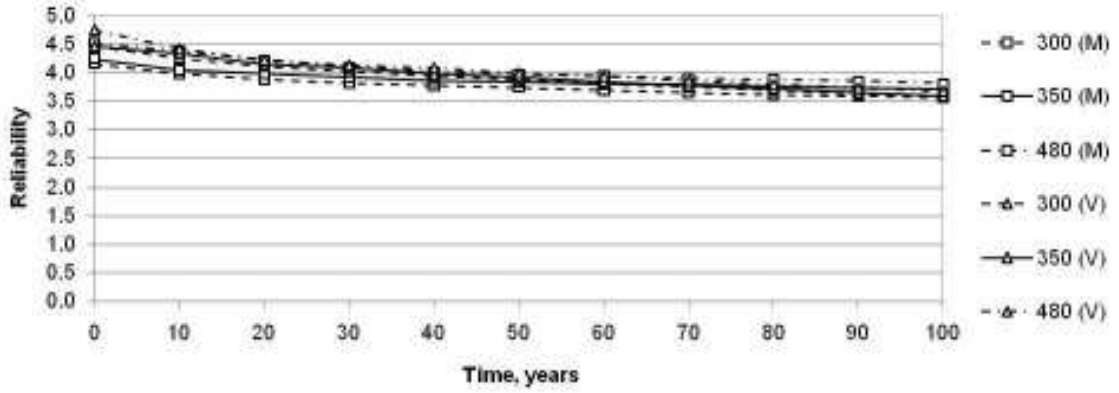

Figure 6.45: Bridges B-1, B-2, B-3, rural corrosion

For the simply-supported box girder bridges with varying steel strengths:

- The reliability of the structures drops below 2.75 only in the case of urban corrosion rate. At the marine and rural corrosion rates, the reliability does not drop below 3.25 over the 100 year time frame.

- At the urban corrosion rate, the time-dependent reliability with respect to the moment resistance of Bridge B-3 (F_{yg} = 480 MPa) drops faster than the other two structures, but only by a small amount.
- Otherwise, there are no significant differences among the results for the three bridges. The failure modes are tightly grouped for each corrosion rate.

Bridges B-1, B-2, and B-3 all have the same web thickness at the abutments and midspan (12.7 mm and 11.1 mm respectively). As a result of this, the effect of steel yield strength on the shear failure mode is not distinguishable. However, the flange thicknesses for B-1, B-2, and B-3 are different (20.6 mm, 25.4 mm, and 12.7 mm respectively), and, at least at the urban corrosion rate, the structure with the highest yield strength and thinnest bottom flange also has the lowest reliability, if only by only a small margin.

I-Girder Bridges

Figure 6.46 to Figure 6.48 compare the reliability curves for the simply supported I-girder bridges I-1 (F_{yg} = 350 MPa), I-2 (F_{yg} = 300 MPa), and I-3 (F_{yg} = 480 MPa).

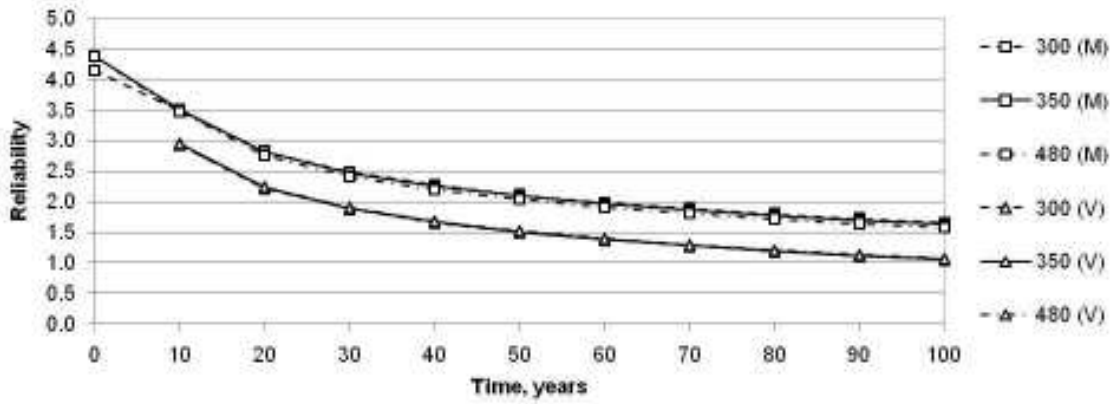

Figure 6.46: Bridges I-1, I-2, I-3, urban corrosion rate.

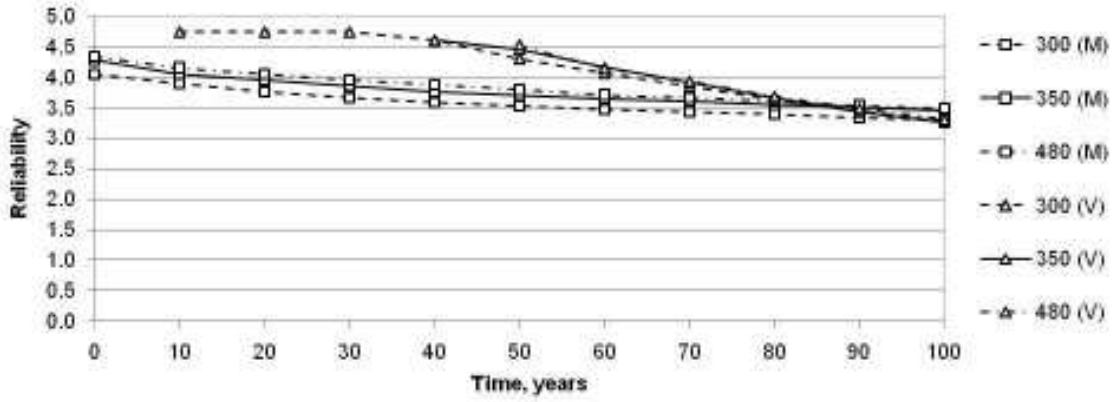

Figure 6.47: Bridges I-1, I-2, I-3, marine corrosion rate

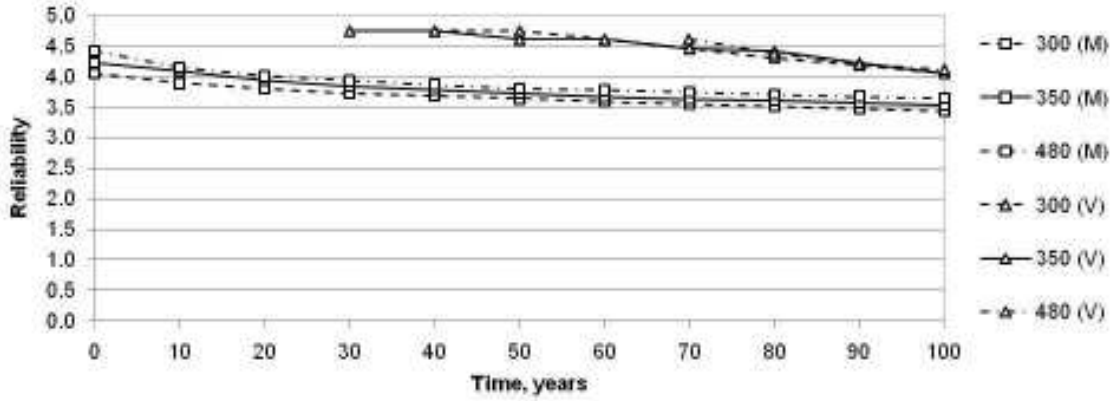

Figure 6.48: Bridges I-1, I-2, I-3, rural corrosion rate

For the I-girder bridges with various girder steel strengths:

- At the urban corrosion rate, the difference between the shear and moment failure modes for the various bridges is negligible; however, at the other corrosion rates, it is more significant, though at no point does the reliability drop below 2.75.
- At all three corrosion rates, the moment and shear bands are closely grouped.
- At the marine and rural corrosion rates, the lower reliability values of Bridge B-2 (F_{yg} =300 MPa) is a result of its lower reliability at year 0.

Regarding the moment failure, the results are counterintuitive: the bridge composed of the lowest strength steel should be the most reliable, by virtue of its thicker section; however, the results here suggest otherwise. The reason for this is that the high strength steel has a higher initial reliability, and this advantage perdures through the test life; however, at high corrosion rates the difference between the bridges is negligible.

Comparison

In general, these results favour high strength steel, since less steel is required and the self-weight of the bridge is lower. While B-2 girder weighs approximately 3.5% more than that of B-1, the B-3 girder weighs 19.8% less than that of B-1. The same is true for the I-girder bridge: the I-2 girder weighs 5.9% more than the I-1 girder, while the I-3 girder weighs 18.7% less than the I-1 girder. Thus there are potential savings to be made in the reduced material used as the girder yield strength is increased, without causing a significant reduction in the time-dependent reliability of the structure.

6.3.4 Bridge Span

Box Girder Bridges

Figure 6.49 to Figure 6.51 show the effect of girder span on the reliability of simply-supported box girder bridges. The bridges being compared are B-1, B-4, and B-5, which have 40 m, 30 m, and 35 m spans respectively.

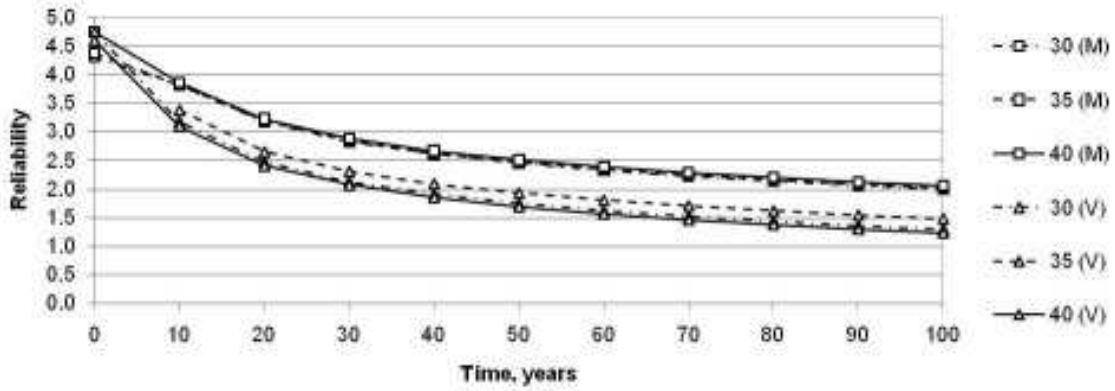

Figure 6.49: Bridges B-1, B-4, B-5, urban corrosion

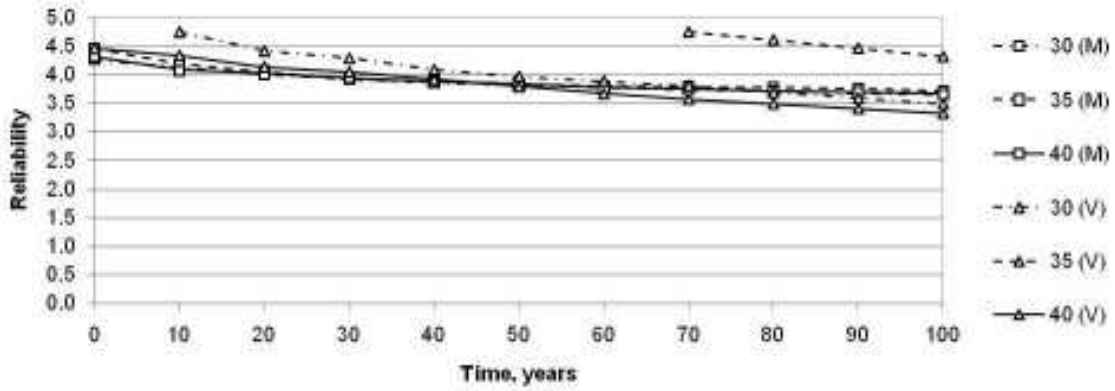

Figure 6.50: Bridges B1, B4, B5, marine corrosion rate.

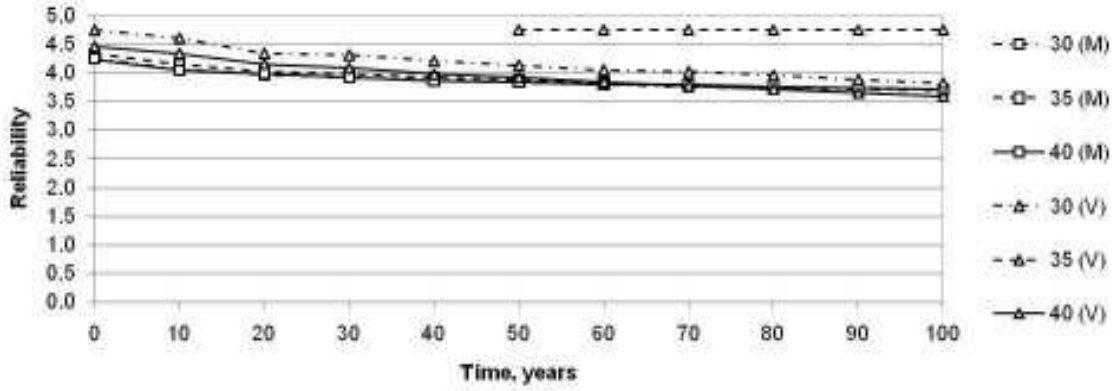

Figure 6.51: Bridges B-1, B-4, B-5, rural corrosion rate.

For the simply-supported box girder bridges of varying lengths:

- At the urban corrosion rate, there is a noticeable difference between the shear failure mode reliability curves of the different bridges, but the moment failure reliability curves are very similar.
- There is also a substantial difference between the shear failure mode reliability curves in the marine and rural corrosion rates.
- Bridge B-5 (35 m span) outperforms B-1 (40 m span) with respect to the shear failure mode; this is due to the fact that they both have the same web thickness, but B-1, being longer, has the larger shear values.

I-Girder Bridges

Figure 6.52 to Figure 6.54 relate to the simply-supported I-girder bridges of varying lengths. I-1, I-4, and I-5 are 40 m, 30 m, and 35 m long, respectively.

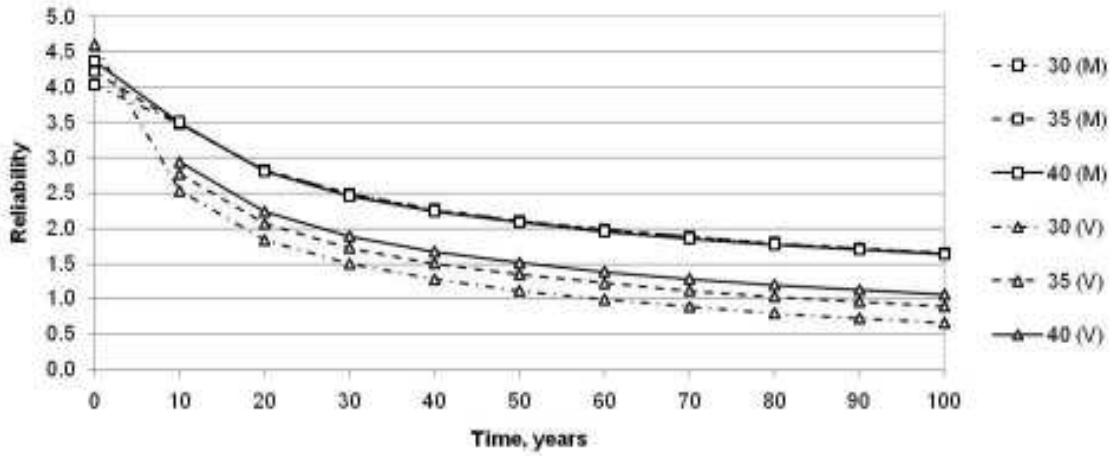

Figure 6.52: Bridges I-1, I-4, I-5, urban corrosion rate.

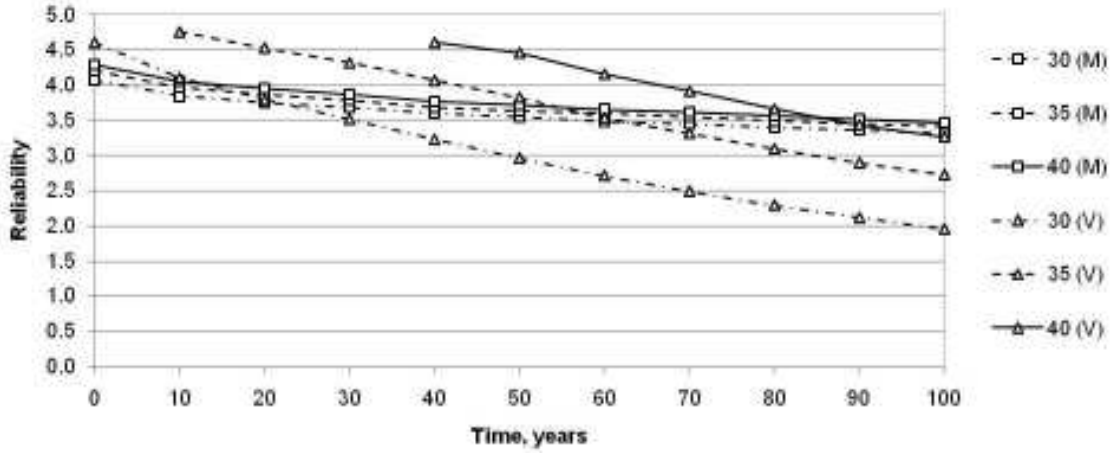

Figure 6.53: Bridges I-1, I-4, I-5, marine corrosion rate.

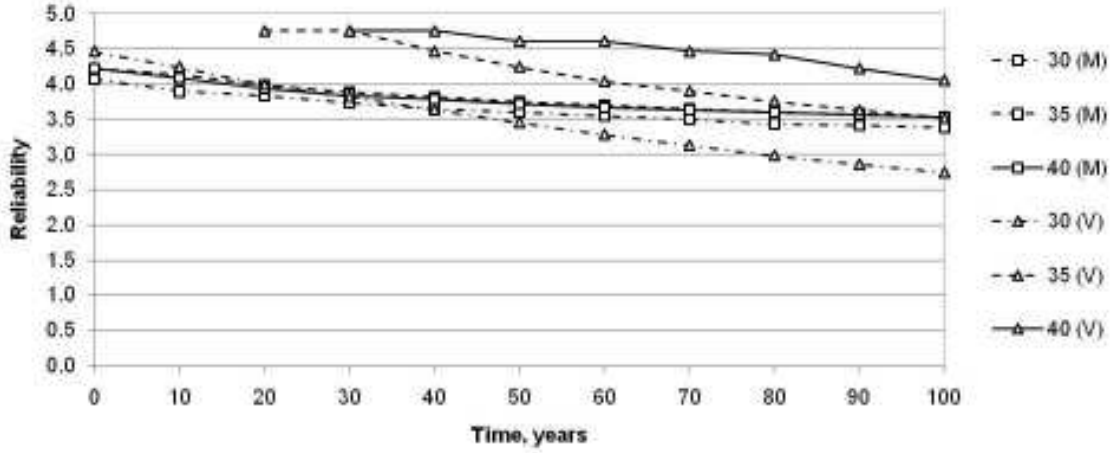

Figure 6.54: Bridges I-1, I-4, I-5, rural corrosion rate.

For the simply-supported I-girder bridges with varying span lengths:

- The moment failure reliability curves of the three bridges are quite similar.
- Shear failure reliability, on the other hand, is quite varied at all corrosion rates.
- The reliability of all three bridges drops below the 2.75 mark prior to the end of the 75 year planned service life at the urban corrosion rate.
- At the marine corrosion rate, the shear failure mode of Bridges I-4 and I-5 drop below the 2.75 mark at 60 and 100 years respectively.
- At the rural corrosion rate, the shear failure mode of Bridge I-4 drops to the 2.75 mark at 100 years. The other bridges stay above 3.25.

The variability of the shear reliability modes is due to the varying thicknesses of the web. Bridges I-1, I-4, and I-5 all have differing web thicknesses at the abutment (14.3 mm, 11.1 mm, and 12.7 mm respectively), where the shear forces are the highest.

Comparison

For the simply-supported box- and I-girder bridges of varying lengths:

- At the urban corrosion rate, the box girder bridges perform better than the I-girder bridges at all span lengths.
- For the I-girder bridges, the shortest span shows the largest decrease in reliability. This is trend is not apparent for the box girder bridges.

6.3.5 Number of Lanes

Box Girder Bridges

Figure 6.55 to Figure 6.57 are for the reliability of the structures with two lanes only (Bridge B-6), as compared to those that have four lanes (Bridge B-1).

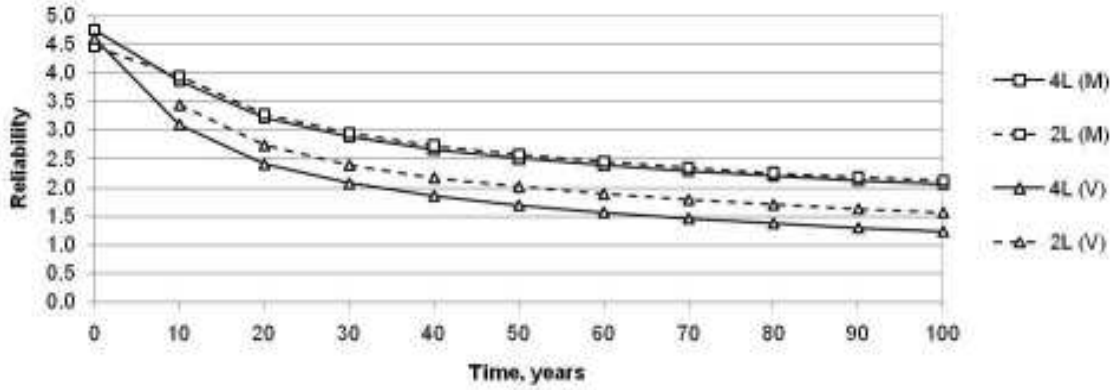

Figure 6.55: Bridges B-1 & B-6, urban corrosion rate

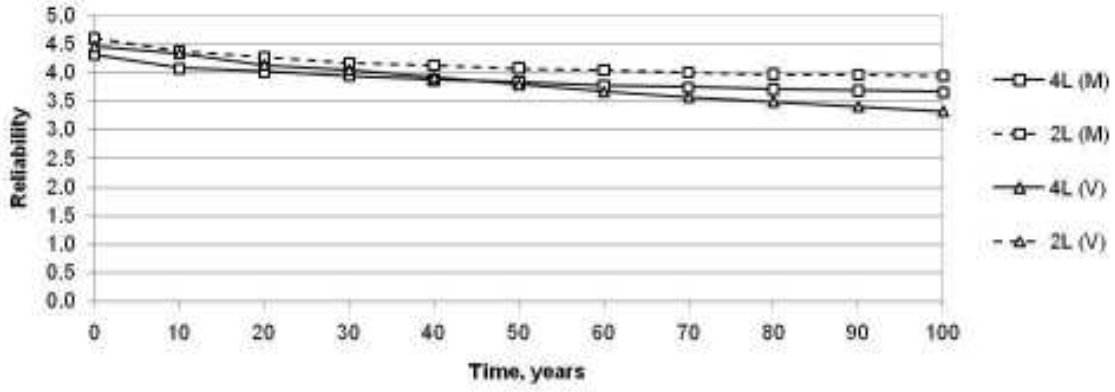

Figure 6.56: Bridges B-1 & B-6, marine corrosion rate

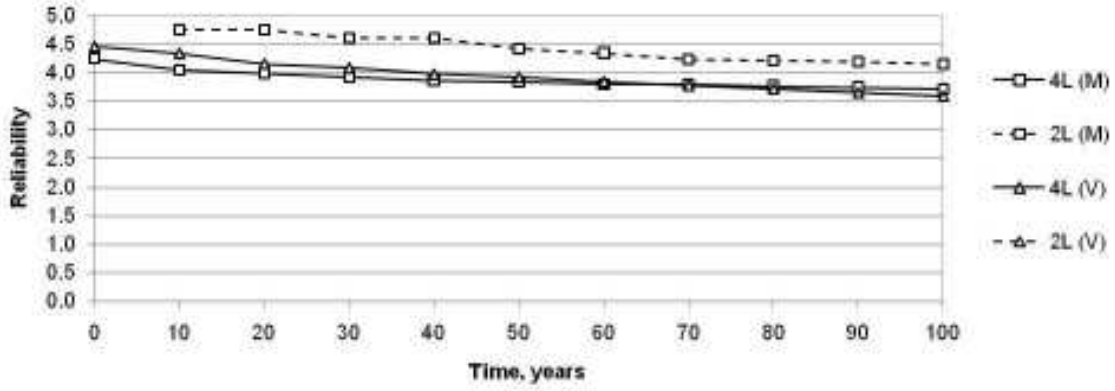

Figure 6.57: Bridges B-1 & B-6, rural corrosion rate

For the box girder bridges with two or four lanes:

- At all corrosion rates, the four-lane bridge is more susceptible to shear and moment failure modes.
- At the marine and rural corrosion rates, the two-lane bridge does not fail in shear.

The reason for the relative susceptibility of the four-lane bridge may be that the web and flange sections of the four-lane bridge are less thick than those of the two-lane bridge. The additional thickness is required because of the weight of the sidewalks and barriers is distributed to fewer girders, and the two-lane bridge has a higher modification factor for live loading (0.9 to 0.7, see Table 5.5).

I-Girder Bridges

Figure 6.58 to Figure 6.60 show a similar comparison for the I-girder bridges.

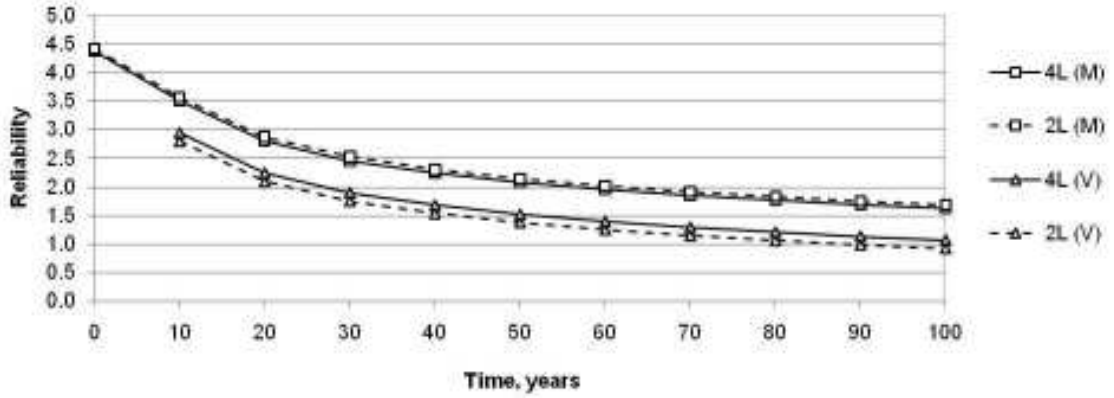

Figure 6.58: Bridges I-1 & I-6, urban rate

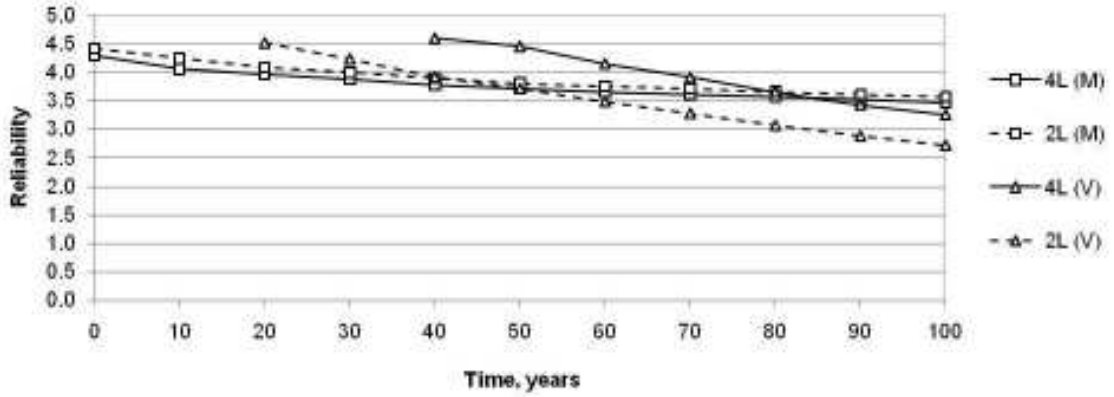

Figure 6.59: Bridges I-1 & I-6, marine corrosion rate

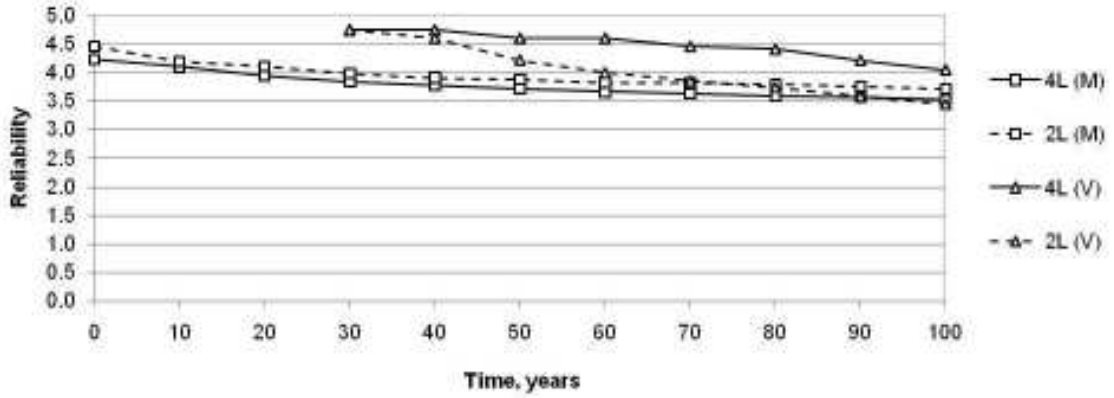

Figure 6.60: Bridges I-1 & I-6, rural corrosion rate

For the I-girder bridges with two or four lanes:

- At all corrosion rates, the two-lane bridge (I-6) is more susceptible to the shear failure mode than the four-lane bridge (I-1).
- At all corrosion rates, the four-lane bridge (I-1) is more susceptible to the moment failure mode than the two-lane bridge (I-6)

Comparison

For the shear failure mode, the two-lane box girder bridge (I-6) is less susceptible than the four-lane box girder bridge (I-1); however, this trend is reversed in the I-girder bridges. The reason for this is that the initial reliability of the four-lane I-girder bridge (I-6) with respect to shear failure is considerably higher than that of the two-lane bridge (I-1). This initial structural advantage remains throughout the duration of the analysis.

6.3.6 Web Breathing Failure Mode

The base case bridges (B-1 & I-1) were also analysed for their resistance to the web breathing limit state (see Section 5.2.1).

Box Girder Bridge

Figure 6.61 shows the results of these tests, for all three corrosion rates, where the comparison is made between the total failure due to the combined ultimate limit states (U) versus the web breathing limit state (WB) on its own.

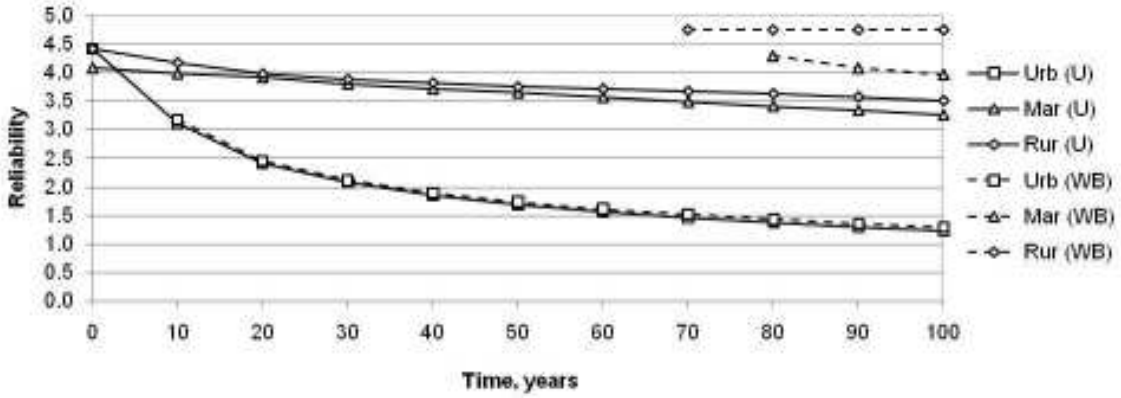

Figure 6.61: Bridge B-1, ULS vs. WB, all corrosion rates

For the box girder bridge:

- The web breathing limit state is never more critical than the ultimate limit states for the box girder bridge.
- The fatigue limit state is likely to affect structural performance only at the urban corrosion rate.

I-Girder Bridge

Figure 6.62 shows a similar comparison for an I-girder bridge.

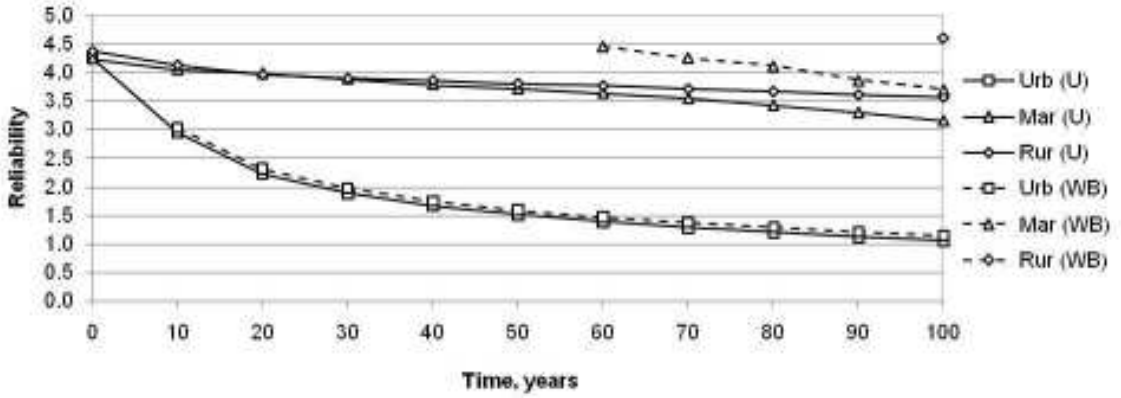

Figure 6.62: Bridge I-1, ULS vs. WB, all corrosion rates

For the I-girder bridge:

- The ULS cases cause a more significant decline in reliability than web breathing.
- Only at the urban corrosion rate is there an unacceptable risk of a web breathing "failure" occurring during the lifespan of the structure.

Comparison

Figure 6.63 compares the web breathing behaviour of the box and I-girder bridges.

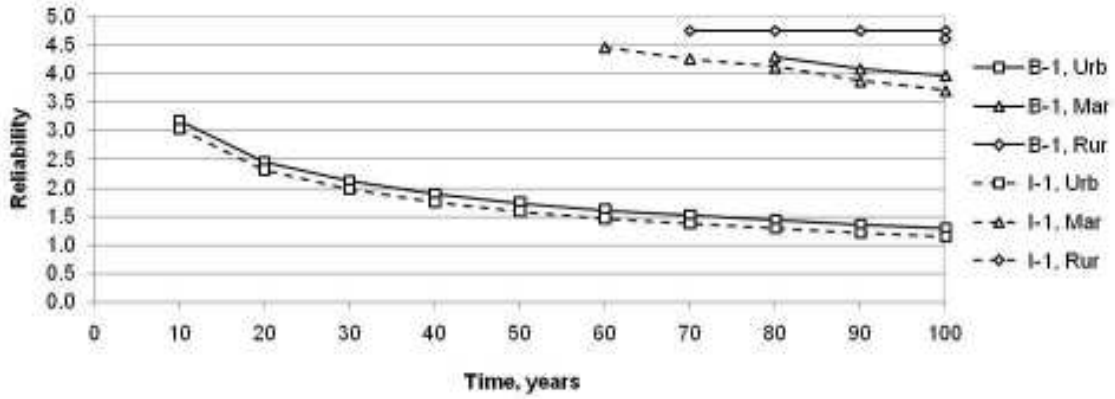

Figure 6.63: Bridges B-1 and I-1, web breathing comparison, all corrosion rates

For the girder type comparison of the web breathing limit state:

- The web breathing behaviour of the I-girder bridge is in all cases slightly worse than that of the box girder bridge.

While the webs are 1/16" thicker on the I-girder bridge (I-1) than the box girder bridge (B-1), they are also attacked from both sides by corrosion, and this makes them more susceptible over time to web breathing failure mode.

6.3.7 Sensitivity Study Summary

General

Two trends in the sensitivity studies are worth noting. First, the idea of a statistical "noise" should be understood. In the probability program, 14 different parameters are varied statistically. Some of these parameters have a more significant impact than others. For example, the corrosion rate has a significant impact, while the highway class does not. The reason that no difference is visible in the highway class variation data (see Figure 6.37 to Figure 6.42) is that, with the numerous parameters being varied simultaneously, a change of one value may be overridden.

The other trend worth noting is the effect of using plate that comes in 1/16" (1.6 mm) increments. This led to a certain "coarseness" in the design of some bridges, which in turn is visible in the reliability data that the analyses produce. One such example of this is

in the comparison of the box girder bridges composed of varying steel strengths, B-1, B-2, and B-3. All of these bridges have the same web thickness at the abutment, as was required by the design; as a result, however, the effect of corrosion on the shear resistance of the bridge (the abutments being points of maximum shear) is less visible.

Corrosion Scenarios

Figure 6.64 and Figure 6.65 show the calculated reliability indices failures due to shear, moment, and shear + moment for the B-1 and I-1 bridges at 0, 25, 50, and 75 years, for the following corrosion scenarios (as illustrated in Figure 5.10): web + flange (W+F), flange-only (F), and top-of-flange-only (TOF). Class A highway traffic volumes are assumed in all cases. The dashed grey lines indicate the 2.75 and 3.25 reliability index levels.

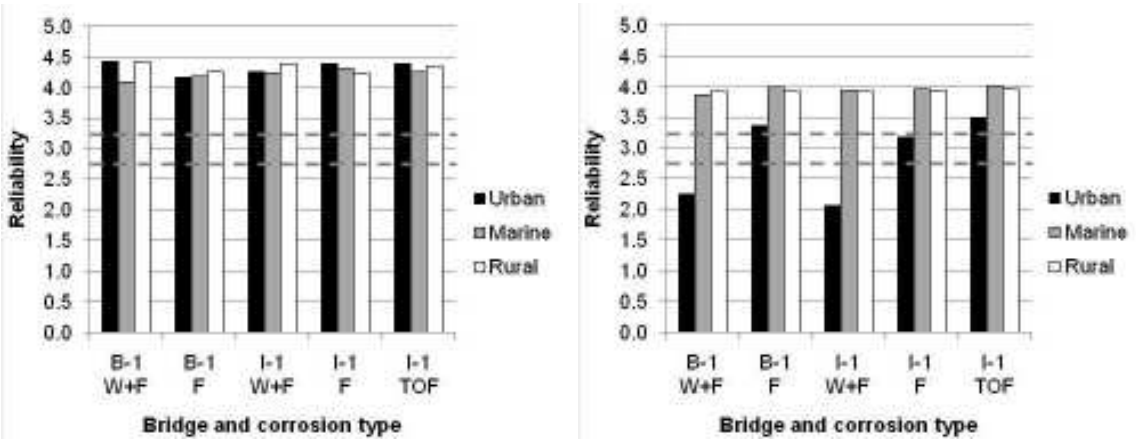

Figure 6.64: Reliability fractions for corrosion scenario bridges at 0 years (left) and 25 years (right)

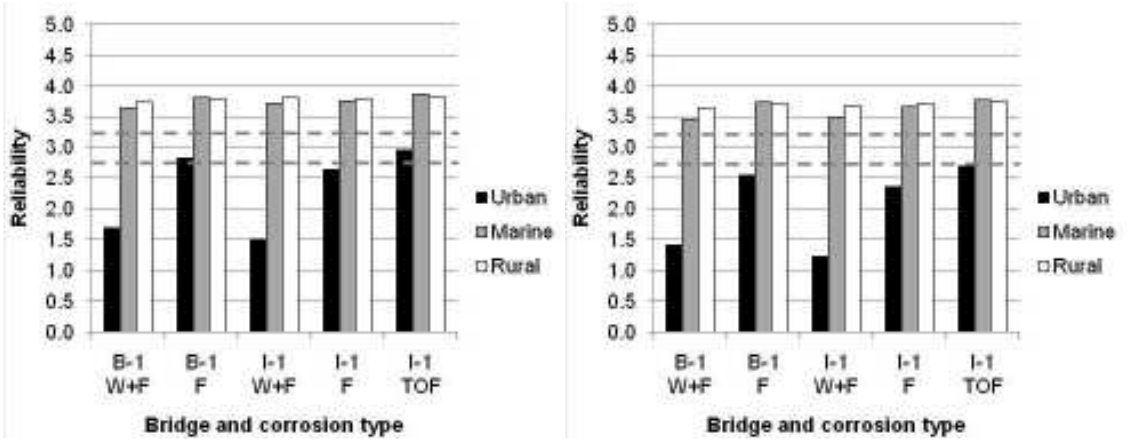

Figure 6.65: Reliability fractions for corrosion scenario bridges at 50 years (left) and 75 years (right)

Figure 6.64 and Figure 6.65 show that the greatest degradation of the reliability level occurs at the I-girder bridge that experiences corrosion to its web and both sides of its bottom flange. However, this is closely followed by the web + flange corrosion to the box girder; this is interesting because the I-girder is being attacked from both sides of its web and bottom flange, while the box girder is attacked on one side only. This result is mirrored by the flange-only corrosion to the B-1 and I-1 bridges. Not surprisingly, the I-1 bridge with corrosion occurring to its top flange-only fares the best.

Bridge Types

Figure 6.66 to Figure 6.69 are bar charts of the reliability indices for the twelve bridge types at 25, 50, and 75 year spans, respectively. They correspond with combined failure due to shear, moment, and shear + moment. All the bridges being considered here are assumed to experience web + flange corrosion and Class A highway traffic volumes. Again, the dashed grey lines are at the 2.75 and 3.25 levels.

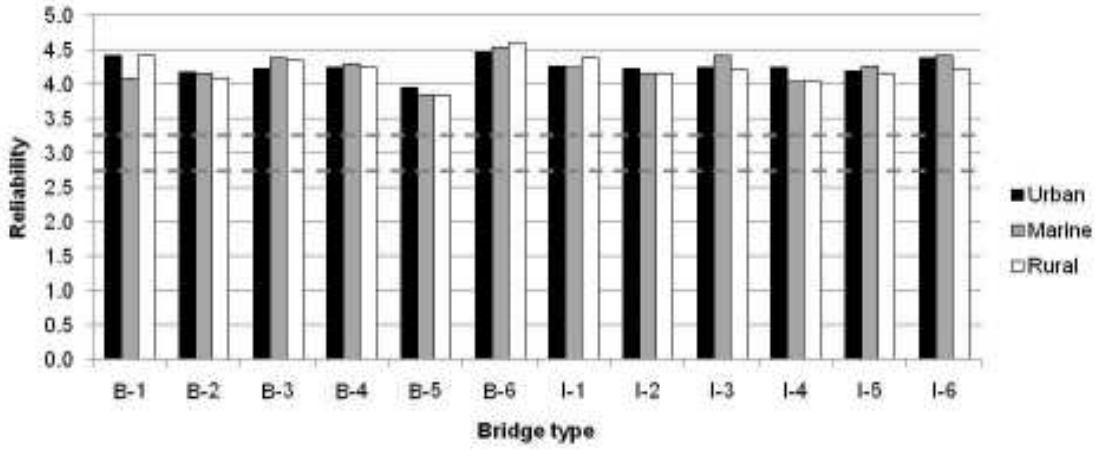

Figure 6.66: Reliability fraction of bridge types at 0 years

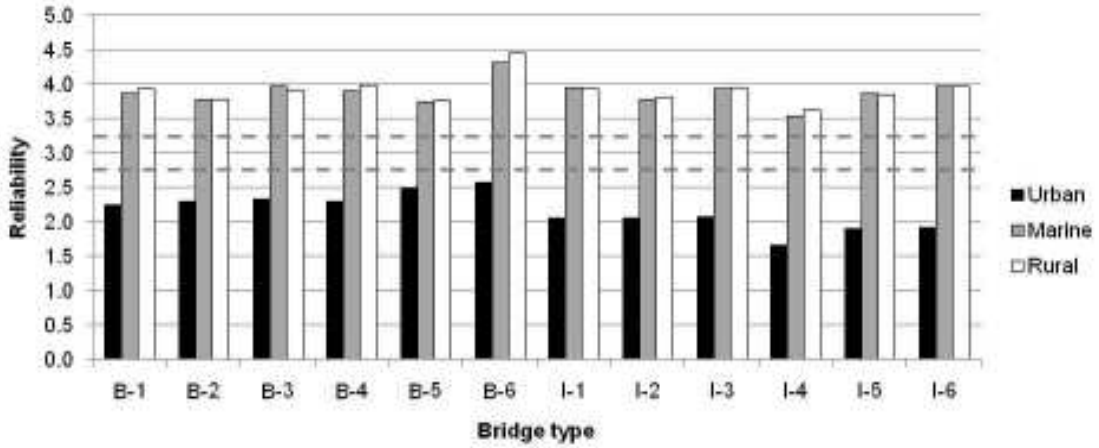

Figure 6.67: Reliability fraction of bridge types at 25 years

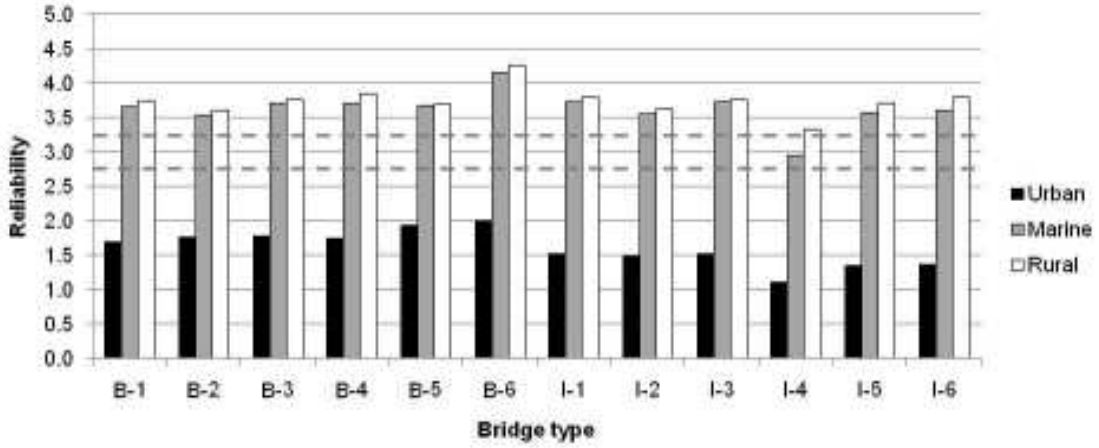

Figure 6.68: Reliability fraction of bridge types at 50 years

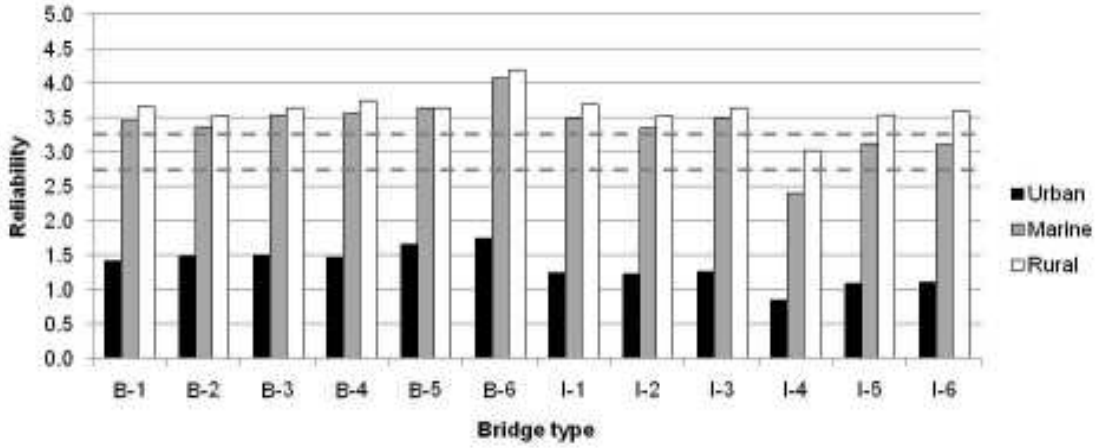

Figure 6.69: Reliability fraction for bridge types at 75 years

Of all the bridges, the one that fares the worst from corrosion is the 30 m long I-girder bridge (I-4), with the 35 m I-girder bridge (I-5) coming next. These bridges have a low

reliability because their shorter length enabled the use of thinner plate for their webs; since corrosion progresses at the same rate regardless of the thickness of the steel, these bridges experienced the fastest degradation.

Except for the I-4 and I-5 bridges, all the bridges maintain a reliability level above 3.25 up to the 75 year mark at the marine and rural corrosion rates. Thus, it can be assumed that if a bridge only shows a normal patina and does not give evidence of significant corrosion, it will perform adequately for the duration of its service life.

6.4 Case Study

Design and maintenance data has been made available for two box girder bridges along Highway 402, between London, Ontario and Sarnia, Ontario. Both bridges are four-lane, four-girder highway overpasses. Both are 83.0 m long, divided into two equal, simply-supported composite box girder spans. However, girder plate thicknesses, slab widths, sidewalk dimensions, etc, are different. Their truck traffic is estimated to be that of Class C structures. Figure 6.70 and Figure 6.71 show the resistance fractions of the two bridges, henceforth labelled A and B.

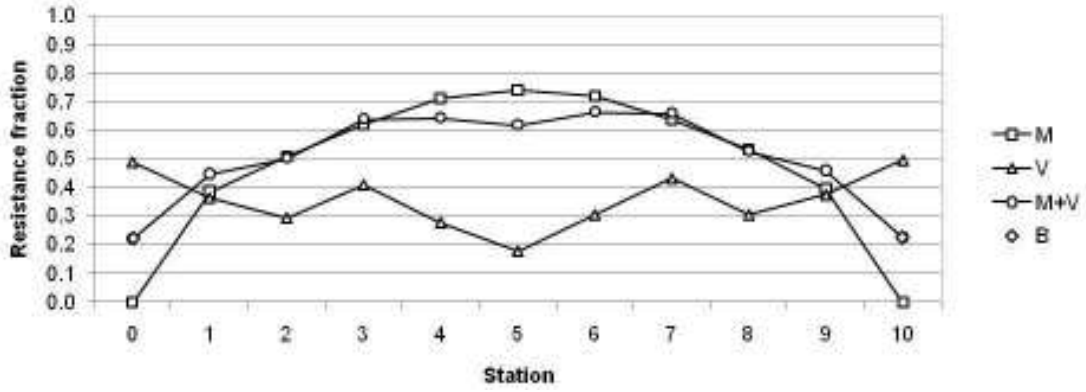

Figure 6.70: Bridge A resistance fractions

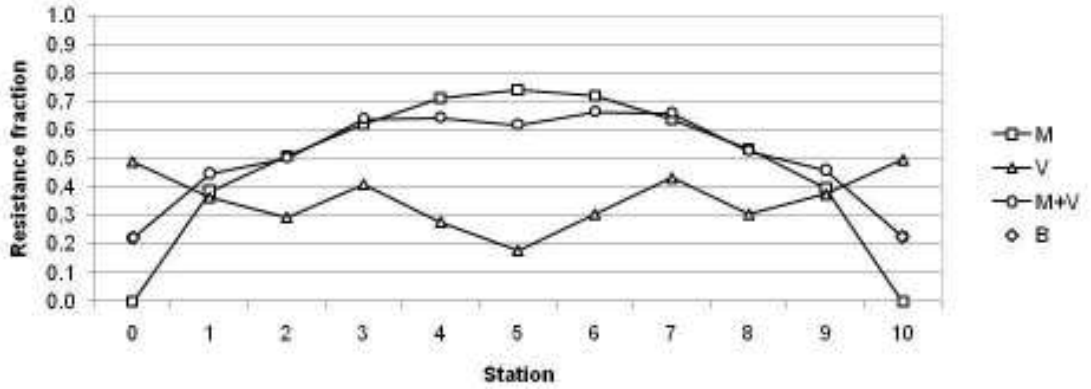

Figure 6.71: Bridge B resistance fractions

Figure 6.72 and Figure 6.73 are the reliability output for both bridges at the urban corrosion rate, with the bridge geometry taken from their respective structural drawings. For all analyses of these bridges, it was assumed that corrosion to the web and flange occur for 3.0 m from each abutment, and corrosion to the flange-only occurs over approximately 15.0 m centred at the midspan section. This is in accordance with what was noted during site visits to both bridges.

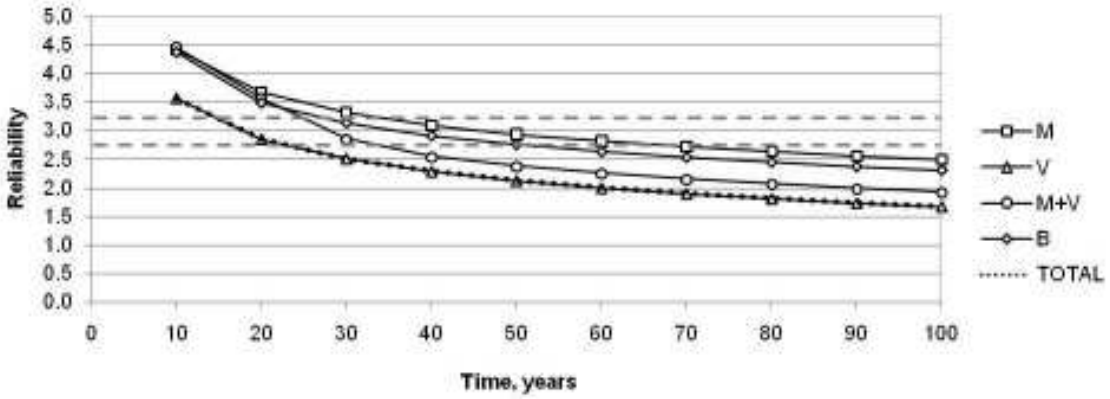

Figure 6.72: Bridge A, urban corrosion rate

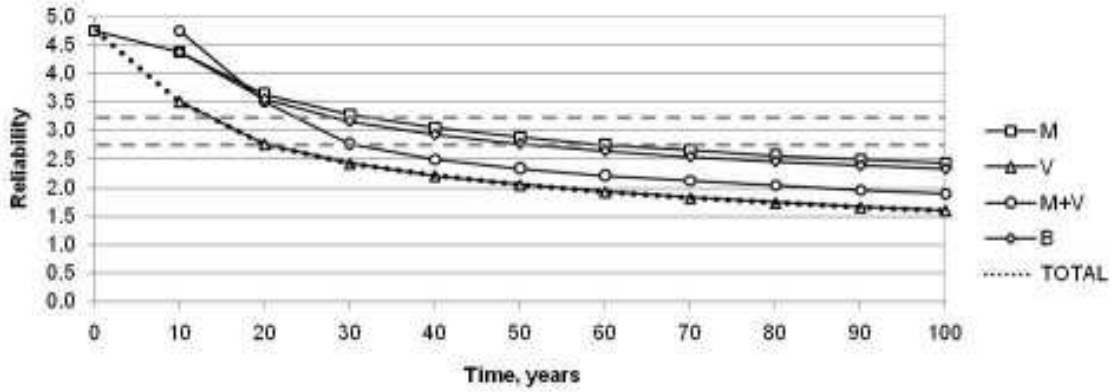

Figure 6.73: Bridge B, urban corrosion rate

An inspection performed 26 years after their construction; as part of this inspection, readings were taken of the material thicknesses at the web and flange of the girders. Inspections were performed at midspan and both abutments for every girder. A series of five readings were taken from side to side of each member. Figure 6.74 shows the points where thickness measurements were taken at all abutment and midspan locations.

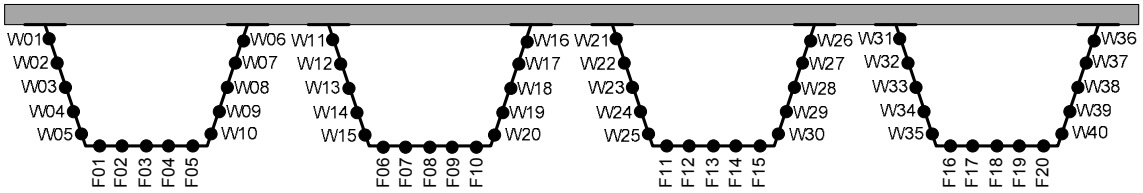

Figure 6.74: Inspection thickness measurement locations

This data can be used to recalculate the reliability, as is shown in the following figures. In Figure 6.75 and Figure 6.76, the time-dependent reliability of the bridges was recalculated using the average measured plate thicknesses for the web and flange at the abutments and midspan, but keeping the urban corrosion rate (which was in keeping with the high level of corrosion on the structures). The plate thicknesses recorded were almost all larger than expected, and even larger than designed; this is the reason for the increase in reliability in these figures.

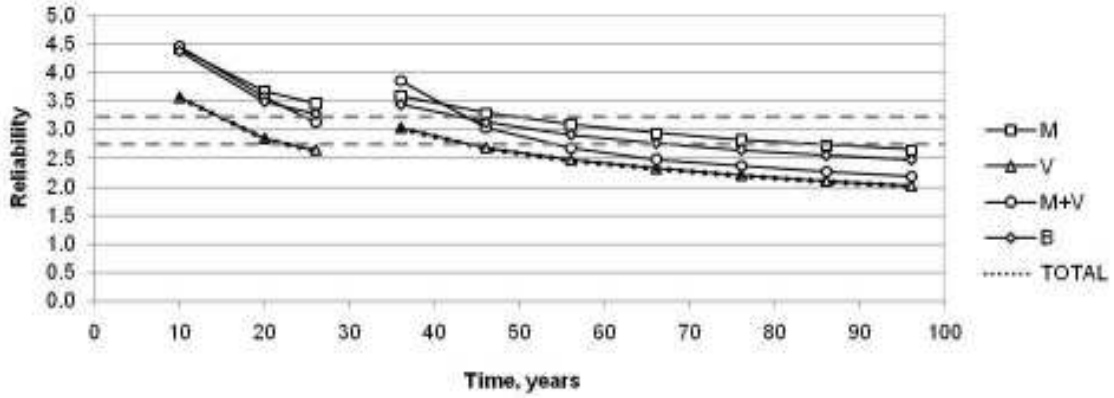

Figure 6.75: Bridge A with plate thicknesses measured at 26 years

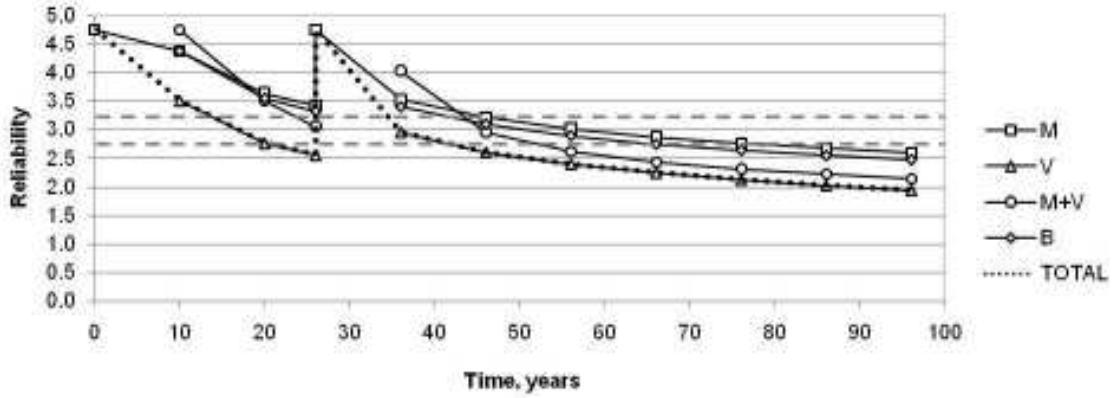

Figure 6.76: Bridge B with plate thicknesses measured at 26 years

Another method of analysis of the bridge data involved using the average plate thickness from the bridge inspection data, but with a normally-distributed variation to account not only for the variation in thickness of the plate itself (due to differences in manufacturing and corrosion), but also for issues with measuring plate thicknesses on corroded, in situ steel.

Assuming a standard deviation of 1.5 mm, the following results may be obtained (Figure 6.77 and Figure 6.78).

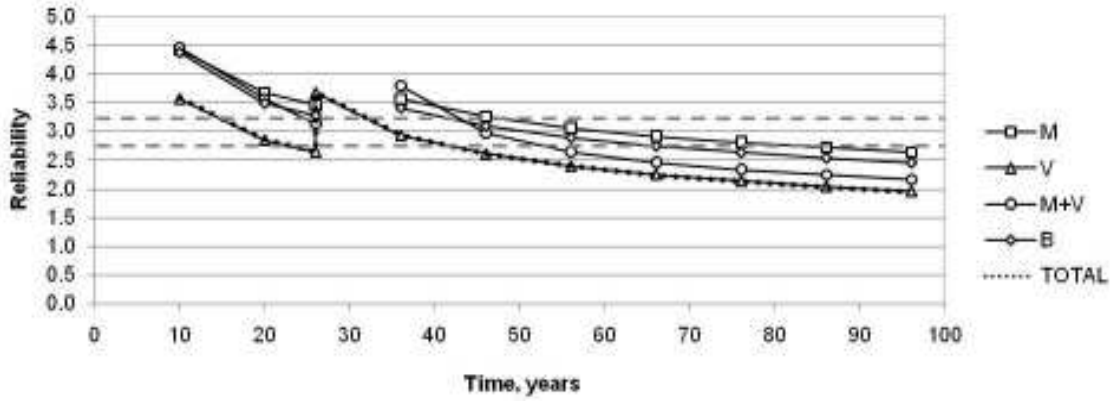

Figure 6.77: Bridge A w/plate thickness variation

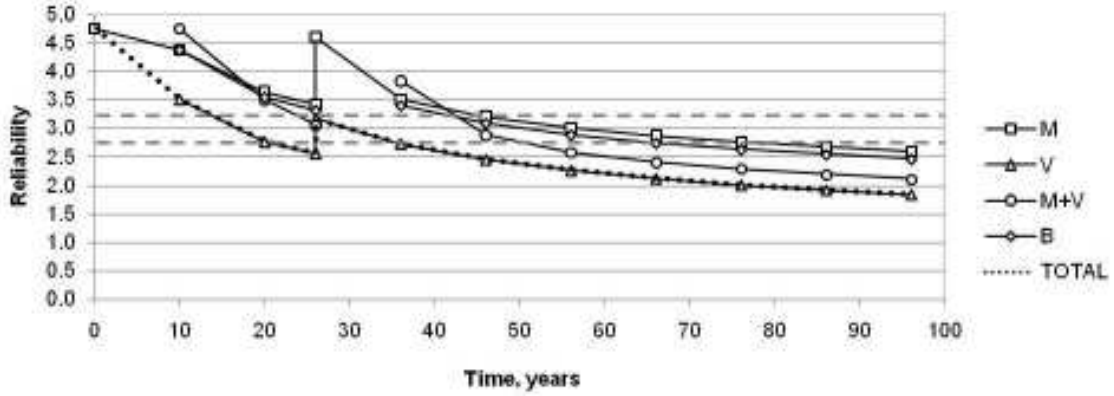

Figure 6.78: Bridge B w/plate thickness variation

It was also possible to determine the corrosion rate and variability from the data. The corrosion rate was found by calculating the difference between the average thickness of a member type and the average of the maximum thicknesses (for each set of five readings) of the member type. The standard deviation of the plate thicknesses was also calculated. Then, Equation 2.3 was used to calculate batches of values for corrosion penetration for the inspection interval (26 years). The mean and standard deviation of the *B* variable were manipulated so that mean and standard deviation of the corrosion values produced matched those of the inspection report. The new values for the mean and standard deviation of *B* were then input into the reliability program, along with the average plate sizes, and the bridge reliability was recalculated. Figure 6.79 and Figure 6.80 are the results of these calculations.

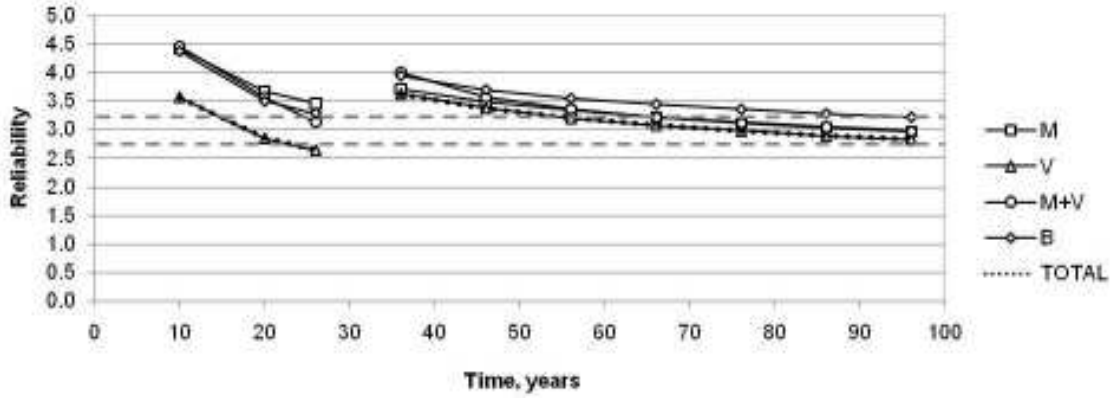

Figure 6.79: Bridge A with measured plate thicknesses and corrosion rates

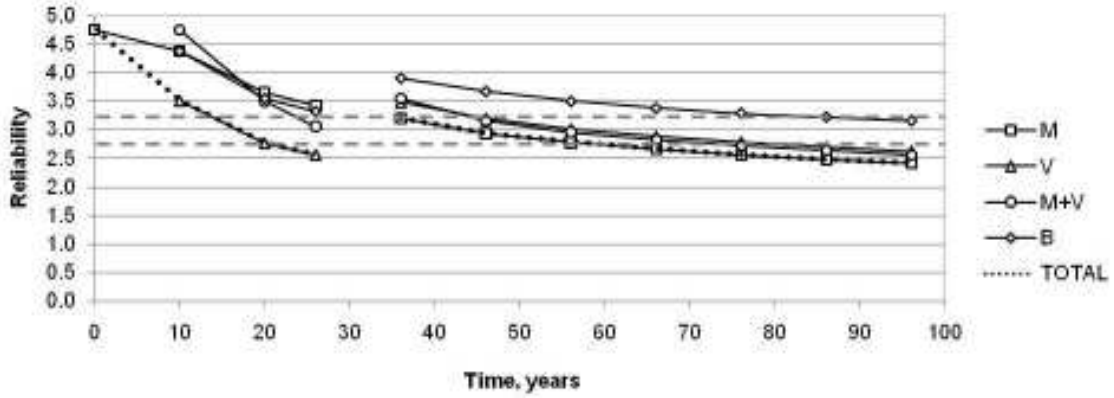

Figure 6.80: Bridge B with measured plate thicknesses and corrosion rates

Figure 6.81 and Figure 6.82 show a summary of the total failures due to ULS for both bridges. For these figures, Method 1 refers to the unmodified reliability analysis, Method 2 refers to the analysis with the updated plate thicknesses only, Method 3 refers to the updated plate thicknesses plus the statistical variation of the thicknesses, and Method 4 refers to the updated plate thicknesses plus the substitution of recalculated corrosion rates and variances.

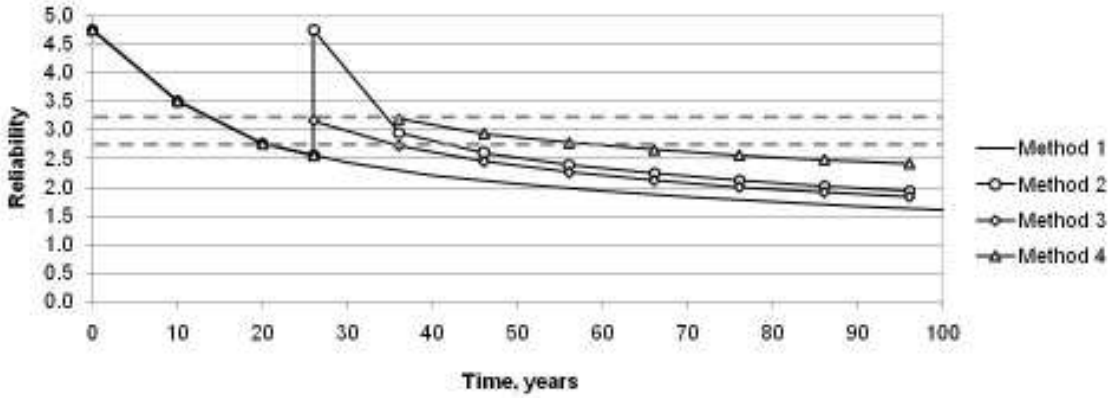

Figure 6.81: Bridge A, summary of reliability calculation modes

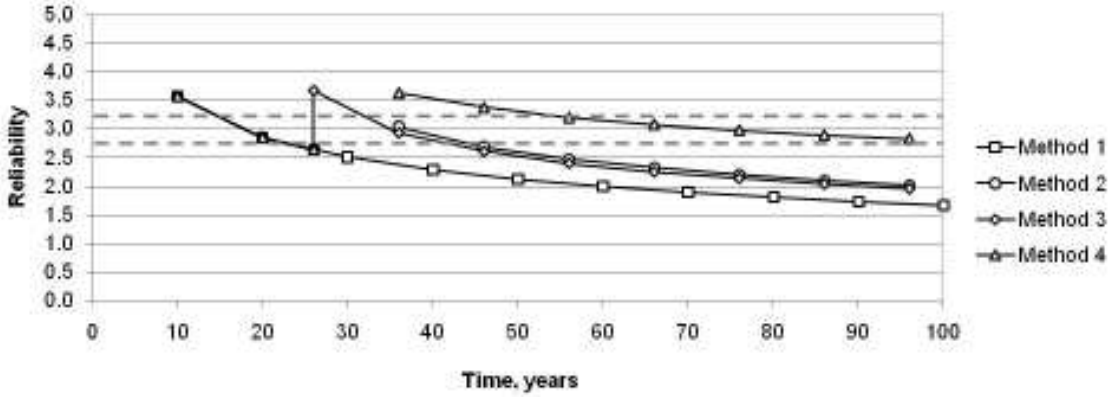

Figure 6.82: Bridge B, summary of reliability calculation modes

Table 6.10 shows the percentage benefit gained by collecting and analysing data from the plate girder bridges. The data below compares the original amount of time it took the bridge to reach a reliability of 2.75, against the recalculated amount of time to reach this level.

Table 6.10: Recalculated bridge service lives

	Bridge A	Bridge B
Method 2	91%	95%
Method 3	82%	66%
Method 4	No failure	166%

CHAPTER 7: CONCLUSIONS AND RECOMMENDATIONS

7.1 Conclusions

The conclusions presented in this chapter are divided into the three main areas of the research work: those resulting from (i) the ultrasonic thickness gauge (UTG) studies, (ii) the protective coating corrosion testing studies, and (iii) the development of the structural analysis models and the analytical studies performed with these models.

7.1.1 UTG Thickness Measurement Studies

Regarding the use of the UTG for the inspection of steel plate experiencing section loss due to corrosion, the following conclusions are drawn:

- The instrument is not capable of measuring from a heavily pitted surface, even if the rust layer has been removed (e.g. by sandblasting or chemical wash), because the surface is too uneven to provide a sufficiently uniform contact between the steel and the UTG probe head.
- When the measurements are made of a weathering steel plate with corrosion product on the opposite side, the UTG does not include the thickness of corrosion product in the measured plate thickness and, therefore, will provide values suitable for service life prediction.
- When measurements are made of a weathering steel plate with corrosion product on the same side then, if a measurement is possible at all, the measured thickness includes the corrosion layer, and this layer appears thicker than it actually is. Therefore the data cannot be used in service life predictions without further analysis to correct for the effect of the corrosion product.
- The UTG measures the shortest distance to an opposing surface; as such, it can be expected to measure the distance to a pit on the opposite side of the plate. In order to accurately determine the lowest plate thickness measurement, however, the UTG probe head must be directly over the pit.

7.1.2 Protective Coating Corrosion Testing Studies

The following conclusions are drawn from the corrosion test studies presented herein of uncoated, metallized, and zinc-tape coated weathering steel specimens, and the subsequent analyses of the corroded specimens:

- All the protective coatings tested, including pure zinc and aluminum-zinc-indium alloy metallizing and PVC-coated zinc tape, were successful in preventing corrosion of the weathering steel specimens in the period of the accelerated test which was estimated to be equivalent to 40 years of natural exposure.
- The surface roughness of the specimen did not have any detectable influence on the effectiveness of the metallizing or zinc tape protective coating.
- The effectiveness of the metallizing and zinc tape protective coatings was not reduced by the degree of sandblasting performed on the structure. More specifically, the results indicate that sandblasting the structure to a sub-white metal condition was not necessary for effective performance of these coatings.
- The metallizing and tape coatings had equal success at protecting the steel from structures constructed 40 years ago and the steel available for structures today.

7.1.3 Modelling of Corroding Weathering Steel Highway Structures

The following conclusions are drawn as a result of the development of the structural models for assessing the remaining service lives of corroding weathering steel highway structures and the analytical studies performed using these models:

- Corrosion occurring at the urban rate to weathering steel structures is capable of significantly reducing their service life. The reliability of the standard box girder bridge analysed herein drops below the acceptable level of 2.75 in approximately 15 years, rather than the 75 years required by [CAN/CSA-S6-06]. Likewise, the reliability of the I-girder bridge is below 2.75 after 13 years, and the two-span box girder bridge is below 2.75 after 22 years. Marine and rural corrosion rates do not pose a challenge to highway structures, except in the case of short-span, simply supported ($\leq$ 35 m) I-girder bridges. These bridges are threatened because, unlike the box girder bridges, their girder webs are both thinner than those of the longer

spans, and attacked from both sides by corrosion. In all other cases, the bridge reliability does not drop below 2.75 over a 75 year service life.

- The two-span box girder bridge has a reliability of 1.77 after 75 years at the urban corrosion rate, as compared with the simply-supported box girder and I-girder bridges which have reliabilities of 1.42 and 1.24 at this point,.
- The bearing failure mode is problematic for time-dependent reliability calculation according to the equations provided in [CAN/CSA-S6-06] because of the slenderness equation, which displays a non-rational bias against high-strength steel.
- Web + flange corrosion causes a more rapid degradation to the box and I-girder bridges than flange-only corrosion. For the web + flange corrosion scenario, shear is the predominant failure mode, while for the flange-only corrosion scenario it is moment. For the box girder bridge at the urban corrosion rate, corrosion to the flange-only results in a reliability of 2.55 after 75 years, compared with 1.42 if both the web and the flange are subject to corrosion; this difference is substantially less at the other corrosion rates. For the I-girder bridge at the urban corrosion rate, the reliability at 75 years is 2.37 for the scenario where both sides of the flange corrode and 2.70 where only the top of the flange corrodes, compared with 1.24 where web + flange corrosion is occurring. For the two-span box girder bridge at the urban corrosion rate, corrosion to the flange-only results in a reliability of 2.07 after 75 years; corrosion to the web and flange together results is a reliability of 1.76.
- The difference between the effects of web + flange corrosion for the box and I-girder bridges is relatively minor. The same is true for flange-only corrosion for these bridges. Nevertheless, the I-girder bridges are more sensitive to corrosion than box-girder bridges at both types of corrosion.
- Over the long term, shear failure mode is critical because of the relative slenderness of the plate. The amount of time required for this to occur depends on the corrosion rate.

- The use of high strength steel for the bridge girder does not have a significant impact on the service life of the highway structure. While it was expected that higher strength steel would result in thinner sections that are more susceptible to corrosion, this is not seen in the analysis results. After 75 years at the urban corrosion rate, a box girder bridge with 480 MPa yield strength has a reliability of 1.48, as opposed to 1.42 for a girder with 350 MPa yield strength. For the I-girder bridge, the 480 MPa bridge's reliability is 1.23, as opposed to 1.24 for the 350 MPa bridge. The use of low strength steel likewise does not have a significant impact. After 75 years at the urban corrosion rate, a 300 MPa yield strength box girder bridge has a reliability of 1.50, compared with 1.42 for the 350 MPa box girder structure. For the I-girder structure, the 300 MPa bridge has a reliability of 1.25 after 75 years, while the 350 MPa bridge has a reliability of 1.24.
- For the box girder structures, shorter spans do not result in a significantly different reliability after 75 years at the urban corrosion rate. The 30, 35, and 40 m long box girder bridges have reliabilities of 1.47, 1.65, and 1.42, respectively. The difference in these values is more a result of the initial reliability of the bridges. For the 30, 35, and 40 m long I-girder bridges, the reliability values are 0.84, 1.08, and 1.24, respectively. This shows the effect of thinner webs which undergo corrosion on both exposed faces.
- The number of lanes appears to have an impact on the time-dependent reliability of the structure, insofar as a structure with fewer lanes will have larger girders, which will in turn be more resistant to corrosion penetration. The box girder bridge at the urban corrosion rate has a reliability of 1.74 at the 75 year mark, while the four-lane bridge has a reliability of 1.42. However, for the I-girder bridge, this effect is not visible due to the relatively low initial reliability of the two-lane bridge design.
- The traffic amount does not have a significant impact on the time-dependent reliability of a bridge. At 75 years, the bridge supporting a Class A highway performs marginally worse than those supporting Class B, C, and D highways (at the urban corrosion rate, 1.42 to 1.51, 1.52, and 1.52, respectively). For the I-

girder bridge, after 75 years at the urban corrosion rate the Class A highway bridge reliability is 1.24, while the Class B, C, and D highway structures are 1.25, 1.27, and 1.29.

- The fatigue limit state of web breathing does not have a more decisive impact than the ultimate limit states. After 75 years at the urban corrosion rate, the reliability is 1.47 for this fatigue limit state for the box girder, and 1.33 for the I-girder bridge, as compared to 1.42 and 1.24 for the structures at the shear, moment, and shear + moment limit states.
- Very significant gains to the predicted service life (ranging from a 66% increase to no predicted failure whatsoever) can be made by integrating data from a particular bridge into a reliability analysis.

7.2 Recommendations for Future Work

7.2.1 Protective Coating Corrosion Testing Studies

The following recommendations are made based on the corrosion testing studies presented herein of uncoated, metallized, and zinc-tape coated weathering steel specimens, and the subsequent analysis of the corroded specimens:

- Additional test parameters, such as the effect of sulphur oxides and scoring on the metallized specimen performance, should be explored.
- The effect of a seam in the zinc tape, especially where the where the surface being covered is uneven, should be studied by further corrosion testing.
- A life-cycle cost comparison of painting versus metallizing or zinc taping would be beneficial. This comparison should take into account the maintenance costs of each coating method as well as the environmental impacts/costs.
- Field trials of the metallizing and zinc tape coatings are recommended.

7.2.2 Modelling of Corroding Weathering Steel Highway Structures

The following recommendations are made as a result of the development of the structural models for assessing the remaining service lives of corroding weathering steel highway structures and the analytical studies performed using these models:

- Further research on the effects of corrosion on bridge deflection and other service limit states, as well as the fatigue limit state, is recommended.
- More data are required about the corrosion rates of weathering steel. A good place to get this data would be from a detailed survey of weathering steel bridges, for example.
- Additional research should be done into two-span bridges, which appear to offer a considerable benefit over the simply-supported bridges with respect to time-dependent reliability.

REFERENCES

Albrecht, P. & Naeemi, A.H. *National Cooperative Highway Research Program Report 272: Performance of Weathering Steel in Bridges*. Transportation Research Board, National Research Council, Washington, D.C., 1984.

Albrecht, P. & Hall, T.T. *Atmospheric Corrosion Resistance of Structural Steels.* Journal of Materials in Civil Engineering, Vol. 15, No. 1, pp. 2-24, February 1, 2003.

Albrecht, P., Coburn, S.K., Wattar, F. M., Tinklenberg, G., & Gallagher, W. P. (). *National Cooperative Highway Research Program Report 314: Guidelines for the Use of Weathering Steel in Bridges*. Transportation Research Board, National Research Council, Washington, D.C., 1989.

Ang, A. & Tang, W. *Probability Concepts in Engineering Planning and Design*. John Wiley & Sons. New York. 1984.

Antaki, G. *Fitness-for-Service and Integrity of Piping, Vessels, and Tanks.* McGraw-Hill, New York. 2005.

ASTM International. *ASTM A 242/A 242M-04: Standard Specification for High-Strength Low-Alloy Structural Steel.* Annual Book of ASTM Standards 2007, Vol. 01.04. ASTM International. 2007.

ASTM International. *ASTM A 588/A 588M-05: Standard Specification for High-Strength Low-Alloy Structural Steel, up to 50 ksi [345 MPa] Minimum Yield Point, with Atmospheric Corrosion Resistance.* Annual Book of ASTM Standards 2007, Vol. 01.04. ASTM International. 2007.

ASTM International. *ASTM A 709/A 709M-06a: Specification for Structural Steel for Bridges.* Annual Book of ASTM Standards 2007, Vol. 01.04. ASTM International. 2007.

ASTM International. *ASTM D 1976-02: Standard Test Method for Elements in Water by Inductively-Coupled Argon Plasma Atomic Emission Spectroscopy.* Annual Book of ASTM Standards 2007, Vol.11.01. ASTM International. 2007.

ASTM International. *ASTM E 1019-03: Standard Test Methods for Determination of Carbon, Sulfur, Nitrogen, and Oxygen in Steel, Iron, Nickel, and Cobalt Alloys by*

Various Combustion and Fusion Techniques. Annual Book of ASTM Standards 2007, Vol. 03.05. ASTM International. 2007.

ASTM International. *ASTM G 1-03: Standard Practice for Preparing, Cleaning, and Evaluating Corrosion Test Specimens*. Annual Book of ASTM Standards 2007, Vol. 03.02. ASTM International. 2007.

ASTM International. *ASTM G 101-04: Standard Guide for Estimating the Atmospheric Corrosion Resistance of Low-Alloy Steels*. Annual Book of ASTM Standards 2007, Vol. 03.02. ASTM International. 2007.

Cheung, M.S. & Li, W.C. *Reliability assessment in highway bridge design*. Canadian Journal of Civil Engineering Vol. 29, pp. 799–805, 2002.

Cheung, M.S. & Li, W.C. *Serviceability reliability of corroded steel bridges*. Canadian Journal of Civil Engineering Vol. 28, pp. 419–424, 2001.

CISC. *Handbook of Steel Construction, 9th Edition*. Canadian Institute of Steel Construction. 2006.

Cook, D.C. *Spectroscopic Identification of Protective and Non-Protective Corrosion Coatings on Steel Structures in Marine Environments.* Corrosion Science Vol. 47, pp. 2550–2570, 2005.

CSA. *CAN/CSA-G40.20-04: General requirements for rolled or welded structural quality steel*. Canadian Standards Association. February 2004.

CSA. *CAN/CSA-G40.21-04: Structural quality steel*. Canadian Standards Association. February 2004.

CSA. *Calibration Report for CAN/CSA-S6-06 Canadian Highway Bridge Design Code*. Pdf. 2007.

CSA. *CAN/CSA-S6-06: Canadian Highway Bridge Design Code*. A National Standard of Canada. Canadian Standards Association. Pdf.

CSA. *CAN/CSA-S6.1-00: Commentary on CAN/CSA-S6-00*, *Canadian Highway Bridge Design Code*. Pdf.

Czarnecki, A.A. *System Reliability Models for the Evaluation of Corroded Steel Girder Bridges*. Thesis. University of Michigan, 2006.

Czarnecki, A.A. & Nowak, A.S. *Time-Variant Reliability Profiles for Steel Girder Bridges*. Structural Safety Vol. 30 No. 1, pp. 49-64, 2006.

Eamon, C.D., Nowak, A.S. *Effect of Secondary Elements on Bridge Structural System Reliability Considering Moment Capacity*. Structural Safety Vol. 26, pp. 29–47, 2004.

Hara, S., Kamimura, T., Miyuki, H., & Yamashita, M. *Taxonomy for Protective Ability of Rust Layer Using Its Composition Formed on Weathering Steel Bridge*. Corrosion Science Vol. 49, pp. 1131–1142, 2007.

Jones, Denny. *Principles and Prevention of Corrosion*. 2nd Ed. Prentice Hall, New Jersey, 1996.

Kamimura, T., Hara, S., Miyuki, H., Yamashita, M., Uchida, H., *Composition and Protective Ability of Rust Layer Formed on Weathering Steel Exposed to Various Environments*, Corrosion Science Vol. 48, pp. 2799–2812, 2006.

Kayser, J.R. *The Effects of Corrosion on Steel Girder Bridges*. Thesis. University of Michigan, 1988.

Kayser, J.R. & Nowak, A.S. *Reliability of Corroded Steel Girder Bridges*. Structural Safety, Vol. 6, pp. 53–63 , 1989.

Kennedy, D.J.L., & Baker, K.A. *Resistance Factors for Steel Highway Bridges*. Canadian Journal of Civil Engineering, Vol. 11, pp. 324–334, 1984.

Kulak, G.L. & Grondin, G.Y. *Limit States Design in Structural Steel, Eighth Edition*. Canadian Institute of Steel Construction Inc., 2006.

Kulicki, J.M., Prucz, Z., Sorgenfrei, D.F., & Mertz, D.R. *National Cooperative Highway Research Program Report 333: Guidelines for Evaluating Corrosion Effects in Existing Steel Bridges*. Transportation Research Board, National Research Council, Washington, D.C., 1990.

Kuroda, S., Kawakita, J., & Takemoto, M. *An 18-Year Exposure Test of Thermal-Sprayed Zn, Al, and Zn-Al Coatings in Marine Environment*. Corrosion, Vol. 62, No. 7, November 2005.

Laumet, P. *Reliability-Based Deterioration Model for Deflection Limit State in Steel Girder Bridges*. Thesis. University of Michigan. 2006.

Legault, R.A. & Leckie, H.P., "Effect of Alloy Composition on the Atmospheric Corrosion Behavior of Steels Based on a Statistical Analysis of the Larrabee-Coburn Data Set," *Corrosion in Natural Environments: ASTM STP 558*, American Society for Testing and Materials, pp. 334-347, 1974.

Matthes, S.A., Cramer, S.D., Bullard, S.J., Covino, Jr., B.S. & Holcomb, G.R. *Atmospheric Corrosion and Precipitation Runoff from Zinc and Zinc Alloy Surfaces*. Presented as Paper No. 03598 at Corrosion 2003, 2003.

McCuen, R.H., & Albrecht, P.M. "Composite Modeling of Atmospheric Corrosion Penetration Data," *Application of Accelerated Corrosion Tests to Service Life Prediciton of Materials: ASTM 1194*, Cragnolino, G. & Sridhar, N., Eds. American Society for Testing and Materials, Philadelphia, pp. 65-102, 1994.

McCuen, R.H. & Albrecht, P.M. *Effect of Alloy Composition on Atmospheric Corrosion of Weathering Steel*. Journal of Materials in Civil Engineering, Vol. 17, No. 2, pp. 117–125, 2005.

McCuen, R.H. & Albrecht, P.M. *Reanalysis of Thickness Loss Data for Weathering Steel*. Journal of Materials in Civil Engineering, Vol. 16, No. 3, pp. 237-246, 2004.

Melchers, R. *Structural Reliability Analysis and Prediction, 2nd Edition*. John Wiley & Sons. 2002.

Misawa, T., Asami, K., Hashimoto, K. & Shimodaira, S. *The Mechanism of Atmospheric Rusting and the Protective Amorphous Rust on Low Alloy Steel.* Corrosion Science, Vol. 14, pp. 279-289, 1974.

Park C.H. *Time Dependent Reliability Models for Steel Girder Bridges*. Thesis. University of Michigan, 1999.

Sagüés, A.A. & Powers, R.G. *Sprayed-Zinc Sacrificial Anodes for Reinforced Concrete in Marine Service*. Presented as paper no. 515 at Corrosion/95, 1995.

Sarveswaran J., Smith J.W. & Blockley, D.I. *Reliability of Corrosion-Damaged Steel Structures Using Internal Probability Theory*. Structural Safety Vol. 20, pp. 237-255, 1998.

Society of Automotive Engineers. *SAE J2334: Cosmetic Corrosion Lab Test – October 2002*. SAE Handbook. 2003.

Society for Protective Coatings. *Joint Surface Preparation Standard SSPC-SP 5/NACE No. 1: White Metal Blast Cleaning*. Pdf. 2000.

Tabsh, S. & Nowak, A. *Reliability of Highway Girder Bridges*. ASCE Journal of Structural Engineering, Vol. 117 (8), pp. 2372–2388, 1991.

Townsend, H.E. & Zoccola, J.C. "Eight-Year Atmospheric Corrosion Performance of Weathering Steel in Industrial, Rural, and Marine Environments," *Atmospheric Corrosion of Metals: ASTM STP 767*, S.W. Dean, Jr., & E.C. Rhea, Eds., American Society for Testing and Materials, 1982, pp. 45-59.

Walbridge, S. *A Probabilistic Study of Fatigue in Post-Weld Treated Tubular Bridge Structures*. EPFL Thesis No. 3330. École Polytechnique Fédérale de Lausanne, 2005.

Wang, J.H., Wei, F.I., Chang, Y.S. & Shih, H.C. *The Corrosion Mechanisms of Carbon Steel and Weathering Steel in SO_2 Polluted Atmospheres*. Materials Chemistry and Physics Vol. 47, pp. l-8, 1997.

APPENDICES

APPENDIX A: CANADIAN WEATHERING STEEL SPECIFICATIONS

For Canadian construction, the relevant codes are [CAN/CSA G40.20] and [CAN/CSA G40.21]. [CAN/CSA G40.21] lists three types of weathering steel:

1. Type R – Atmospheric corrosion-resistant steel
2. Type A – Atmospheric corrosion-resistant weldable steel
3. Type AT – Atmospheric corrosion-resistant weldable notch-tough steel.

Table 1.1 contains the chemical compositions for some of the weathering steels provided in [CAN/CSA G40.21-04].

Table A.1: Chemical composition of weathering steels, % [CAN/CSA G40-21]

Element	350R	350A	350AT
C	0.16 max	0.20 max	0.20 max
Mn	0.75 max	0.75-1.35	0.75-1.35
P	0.05-0.15	0.03 max	0.03 max
S	0.04 max	0.04 max	0.04 max
Si	0.75 max	0.15-0.50	0.15-0.50
Cr	0.30-1.25	0.70 max	0.70 max
Ni	0.90 max	0.90 max	0.90 max
Cu	0.20-0.60	0.20-0.60	0.20-0.60

The number 350 refers to the yield strength of the steel in MPa. 350R steel is atmospheric corrosion-resistant steel for light uses such as siding and light structural members. 350A steel is similar to 350R, except that is may be used for more critical structural elements such as the compression members in bridges. 350AT differs from the other two in that it is suitable for welded construction where notch toughness at low temperature is a design requirement [CISC 2006].

APPENDIX B: INDIVIDUAL SPECIMEN MASS LOSS DATA

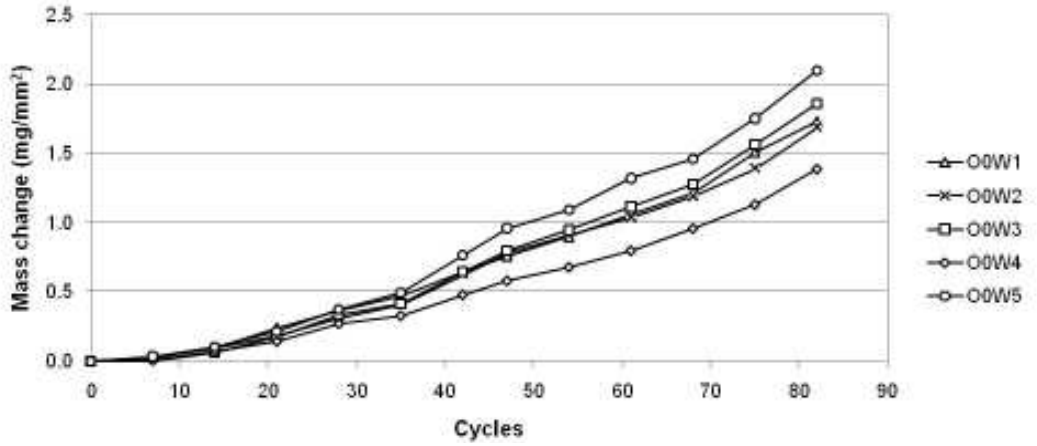

Figure B.1: Uncoated old steel specimens

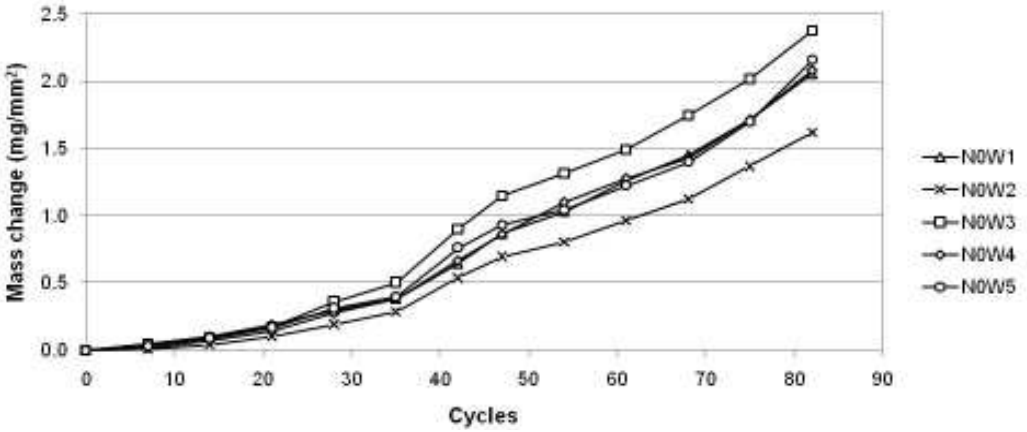

Figure B.2: Uncoated new steel specimens

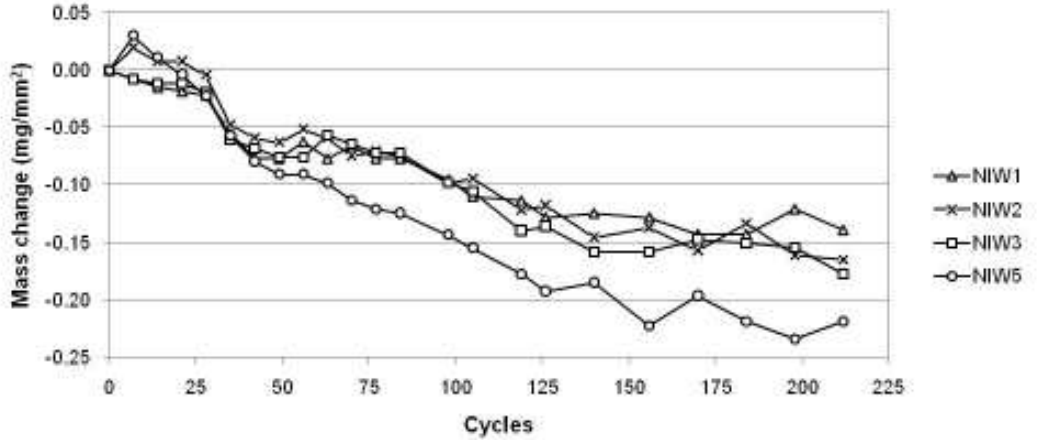

Figure B.3: Aluminum alloy metallized, fully-sandblasted, new steel specimens

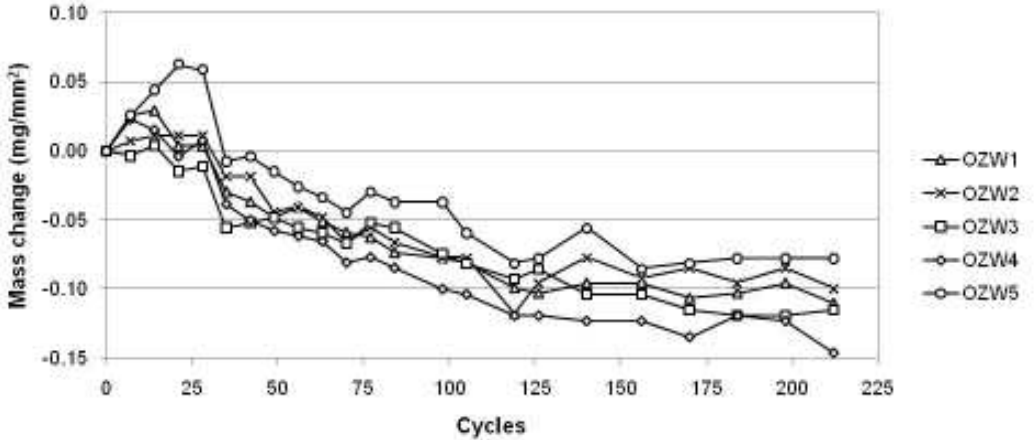

Figure B.4: Zinc metallized, fully-sandblasted, old steel specimens

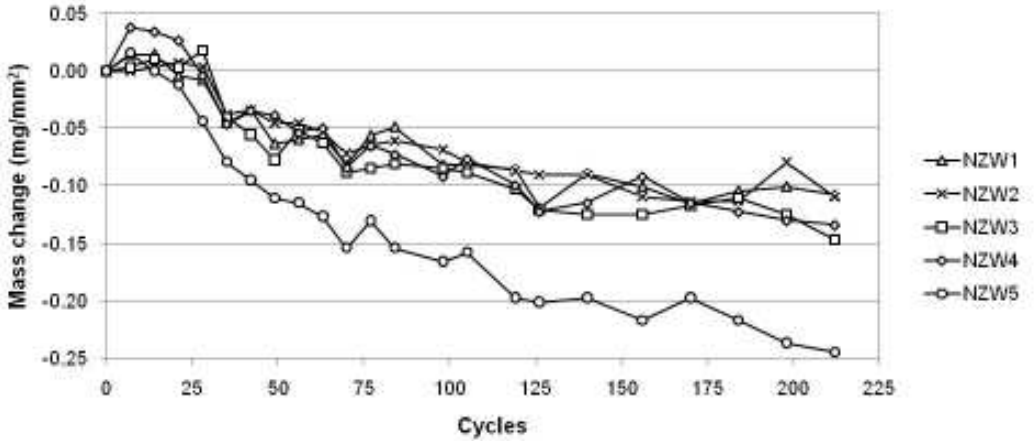

Figure B.5: Zinc metallized, fully-sandblasted, new steel specimens

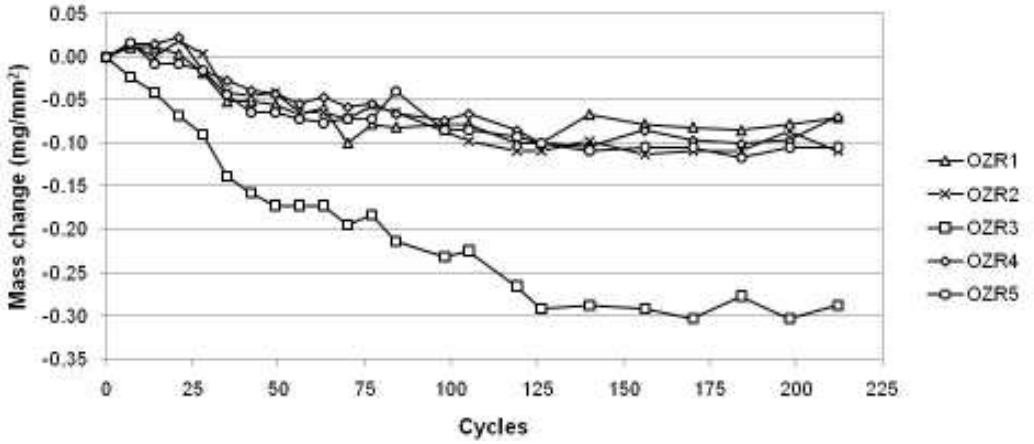

Figure B.6: Zinc metallized, partially-sandblasted, old steel specimens

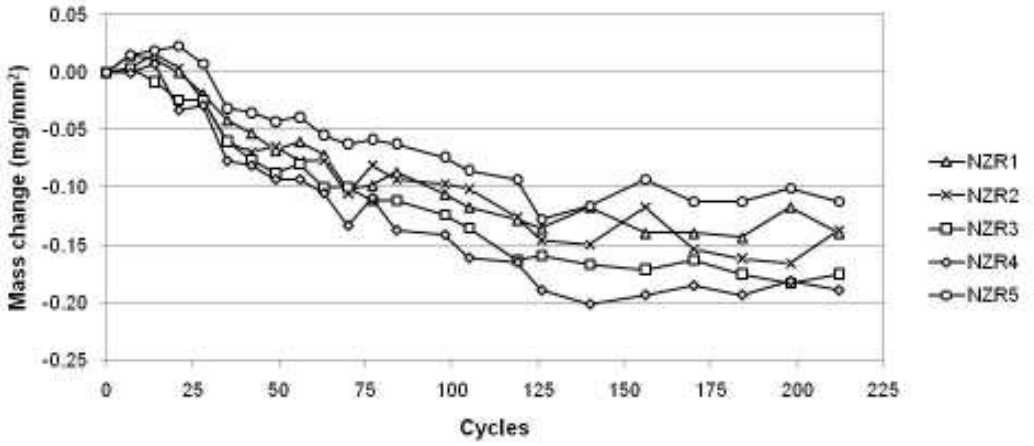

Figure B.7: Zinc metallized, partially-sandblasted, new steel specimens

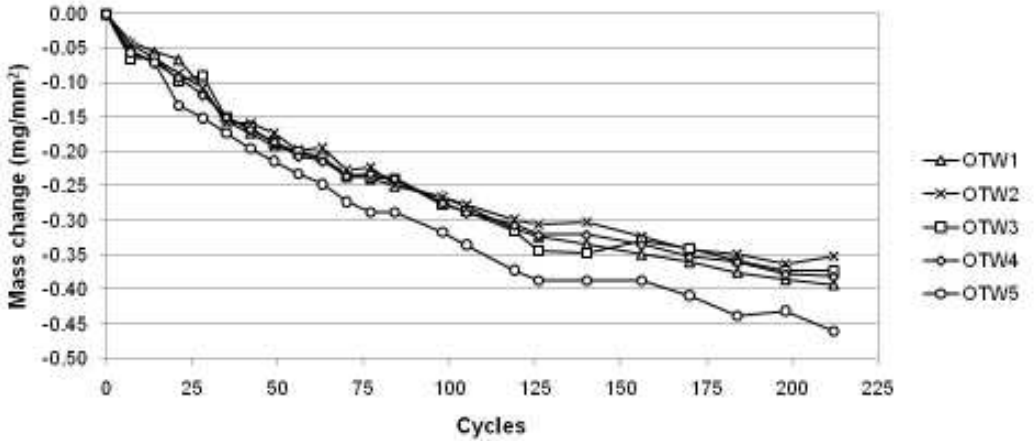

Figure B.8: Zinc taped, fully-sandblasted, old steel specimens

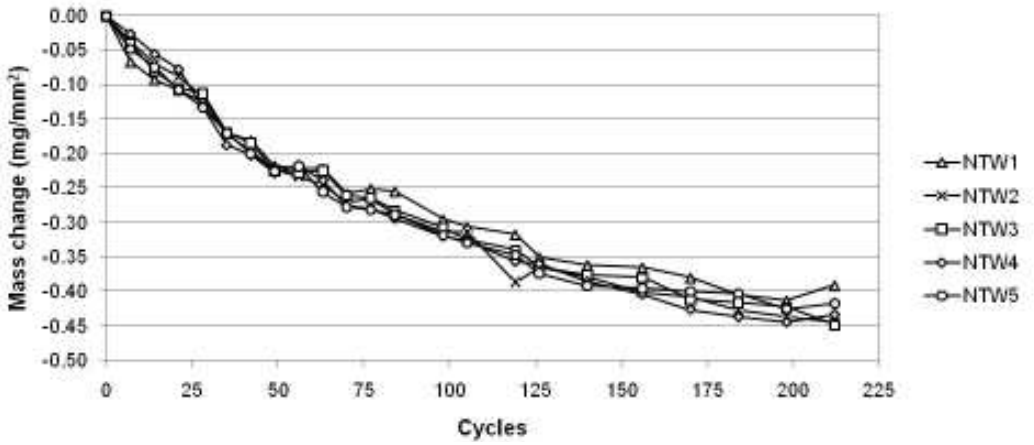

Figure B.9: Zinc taped, fully-sandblasted, new steel specimens

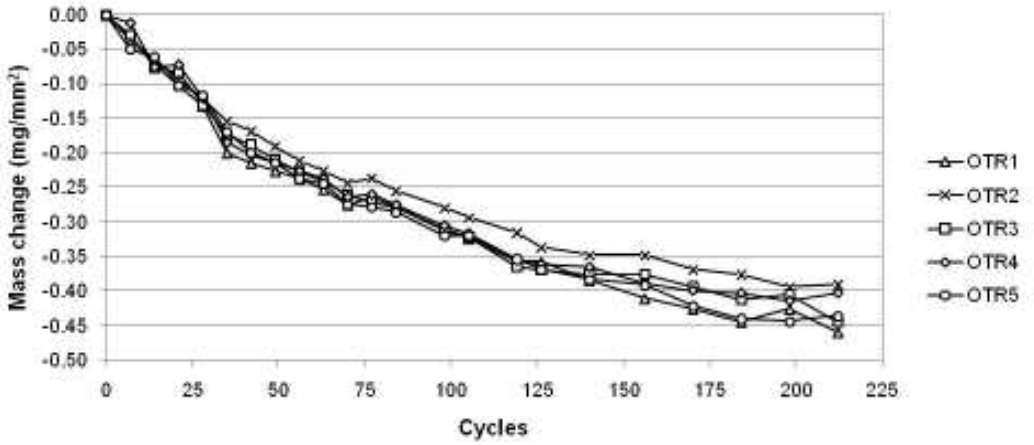

Figure B.10: Zinc taped, partially-sandblasted, old steel specimens

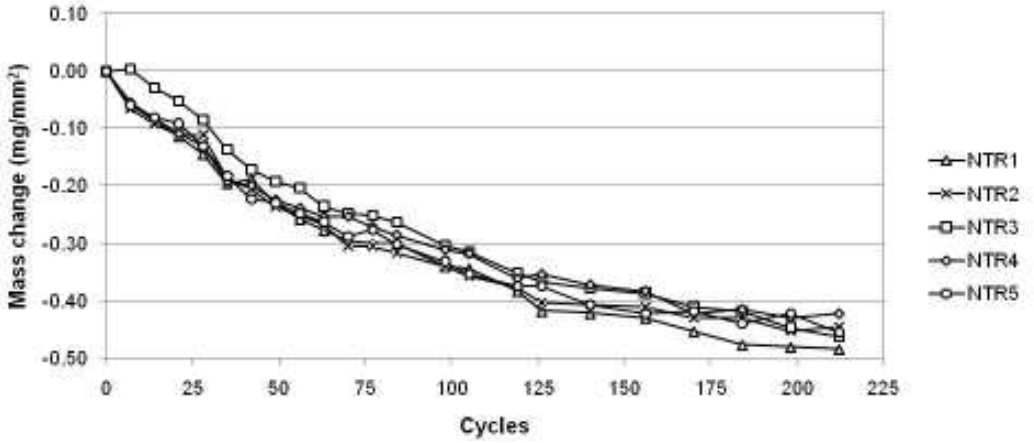

Figure B.11: Zinc taped, partially-sandblasted, old steel specimens